

The Formation of Stars: From Clouds to Cores

by

Erica Fogerty

Submitted in Partial Fulfillment of the  
Requirements for the Degree  
Doctor of Philosophy

Supervised by Professor Adam Frank

Department of Physics and Astronomy  
Arts, Sciences and Engineering  
School of Arts and Sciences

University of Rochester  
Rochester, New York

2017

This work is dedicated to my scientific ancestors; your curiosity, perseverance, and creativity inspires all those who follow in your footsteps.

# Table of Contents

<b>Biographical Sketch</b>	<b>vi</b>
<b>Acknowledgements</b>	<b>vii</b>
<b>Abstract</b>	<b>viii</b>
<b>Contributors and Funding Sources</b>	<b>ix</b>
<b>List of Tables</b>	<b>x</b>
<b>List of Figures</b>	<b>xi</b>
<b>List of Acronyms</b>	<b>xiv</b>
<b>1 Introduction</b>	<b>1</b>
1.1 Early, Quasi-static Models of Star Formation . . . . .	1
1.2 Dynamic Modes of Star Formation . . . . .	6
1.3 Modeling the Dynamical Evolution of Clouds, Cores, and Filaments with AstroBEAR . . . . .	10
<b>2 Numerical Methods</b>	<b>13</b>
2.1 Introduction . . . . .	13
2.2 Governing Equations . . . . .	14
2.3 Adaptive Mesh Refinement in AstroBEAR . . . . .	19
2.4 Source Terms: Self-gravity . . . . .	23
2.4.1 Testing Self-gravity in AstroBEAR: the Jeans Instability . . . . .	25
2.4.2 Modification: Bonnor-Ebert Sphere Module . . . . .	27
2.5 Source Terms: Heating & Cooling . . . . .	31
2.6 Source Terms: Sink Particles . . . . .	32

2.6.1	Modification: Radiation Feedback from Sink Particles . . . . .	33
2.6.2	Modification: Outflow Feedback from Sink Particles . . . . .	35
<b>3</b>	<b>The Effect of Environment on Single Star Collapse</b>	<b>39</b>
3.1	Introduction . . . . .	39
3.2	Methods . . . . .	42
3.2.1	Numerical Model . . . . .	42
3.2.2	Simulation Parameters . . . . .	45
3.3	Results . . . . .	46
3.3.1	A Test of Stability: The Sparse Ambient Medium Case . . . . .	46
3.3.2	Outside-in Collapse of BE Spheres: The “Classic” Case . . . . .	47
3.3.3	Varying the Ambient Density: New Collapse Modes . . . . .	49
3.4	Discussion . . . . .	61
3.5	Conclusions . . . . .	68
<b>4</b>	<b>Molecular Cloud Formation in High-shear, Magnetized Colliding Flows</b>	<b>72</b>
4.1	Introduction . . . . .	72
4.2	Methods . . . . .	75
4.2.1	Numerical Model . . . . .	75
4.2.2	Simulation Parameters . . . . .	77
4.3	Generating Shear via an Oblique Collision Interface . . . . .	79
4.4	Mass-to-flux Ratio . . . . .	81
4.5	Protocluster Formation and Evolution . . . . .	84
4.6	Morphology . . . . .	87
4.6.1	Main Features in Column Density . . . . .	93
4.7	Magnetic Fields and Dynamics: $\langle \beta^{-1} \rangle$ maps . . . . .	98
4.8	Thermodynamics: Probability Density Functions . . . . .	102
4.9	Energy Spectra . . . . .	107
4.10	Discussion . . . . .	110
4.11	Appendix . . . . .	113

4.11.1	Magnetized Ring Model . . . . .	113
<b>5</b>	<b>The Formation of Prestellar Filaments by MHD Shock Processes</b>	<b>117</b>
5.1	Introduction . . . . .	117
5.2	Methods . . . . .	121
5.2.1	Numerical Model and Simulation Parameters . . . . .	121
5.3	Infinite Adiabatic Oblique Shocks . . . . .	124
5.3.1	Hydro Case . . . . .	124
5.3.2	MHD Case . . . . .	125
5.4	Finite Oblique Shocks, with Cooling . . . . .	127
5.4.1	The Effects of Varying $\beta$ and $\theta$ on Reorientation . . . . .	127
5.4.2	Temporal Evolution of the Flows . . . . .	131
5.5	Discussion . . . . .	135
5.6	Appendix: Resolution Study . . . . .	138
<b>6</b>	<b>Summary and Future Directions</b>	<b>141</b>
6.1	Summary . . . . .	141
6.1.1	Molecular Cloud Formation and Dynamics in High-Shear, Magnetized Environments . . . . .	142
6.1.2	MHD Shock Dynamical Evolution of Prestellar Filaments . . . . .	144
6.1.3	Non-classical Collapse Dynamics of Bonnor-Ebert Spheres . . . . .	144
6.2	Future Directions . . . . .	145
6.2.1	Cloud-to-core Star Formation and ‘Closing the Feedback Loop’ . . .	145
6.2.2	Turbulent Fragmentation across Cosmic Time . . . . .	149
	<b>Bibliography</b>	<b>151</b>

# Biographical Sketch

Erica Fogerty (née Kaminski) was born in 1986 in Philadelphia, Pennsylvania. She attended Ursinus College from 2004 to 2006, and then transferred to the University of Rochester to complete her Bachelor of Science degree in Neuroscience. In 2008, Erica was awarded a ‘Take-Five Scholarship’ from the University, which granted her an extra year of college, tuition-free, to pursue her growing interests in physics. At the completion of this program, she decided to remain at the University to pursue doctoral research in Physics and Astronomy, under the direction of Professor Adam Frank. She began graduate coursework in 2010, and was awarded her Master of Arts degree in 2013. Her doctoral research has focused on the physics of molecular cloud and star formation. Alongside her research, she has been actively engaged in scientific outreach aimed at supporting underrepresented minorities in the sciences.

The following publications were a result of work conducted during the doctoral study:

Fogerty, E., Carroll-Nellenback, J., Frank, A., Heitsch, F., & Pon, A. 2017, in press, MNRAS

Fogerty, E., Frank, A., Heitsch, F., Carroll-Nellenback, J., Haig, C., & Adams, M. 2016, MNRAS, 460, 2110

Kaminski, E., Frank, A., Carroll, J., & Myers, P. 2014, ApJ, 790, 70

Kaminski, E., Frank, A., Carroll, J., & Myers, P. 2013, in Protostars and Planets VI Posters

# Acknowledgements

Adam, you have played a pivotal role in shaping my life to where it is today... it is truly remarkable. I remember the first conversation we had when I stopped you on campus to tell you how moved I was after hearing a public talk you recently gave. From there, you encouraged me to take your astronomy course and I remember being so intellectually stimulated during those classes that I would feverishly scribble down notes as I tried to keep up with everything you were saying (I think I still have some of those notebooks). After that, you encouraged me to pursue my highest aspiration – graduate school in Physics. Thank you for the unwavering support and guidance you have shown me over these many years. I will never forget you, nor this profound scientific pilgrimage as your apprentice. I hope we remain colleagues and friends for the rest of our lives.

Jonathan, you have a rare ability to hold deep and thoughtful conversations on nearly any subject, and I have enjoyed sharing in them with you over the years. I am very grateful Adam assigned me to the star formation ‘team’ in our group. Following in your footsteps has been one of the great joys (and exciting challenges) of graduate school. You are my respected colleague, mentor, and friend.

To the University of Rochester Astronomy group: thank you for welcoming me into the ‘family.’ I will always have fond memories of the intellectually stimulating environment you helped to create in the Department.

Lastly, to the one I love, Shane. You have shown me the stars and everything in-between. This thesis and my life’s work is dedicated to you in the utmost. Cheers to the many years ahead of us as we continue to learn and grow in each other’s company.

# Abstract

High resolution simulations were conducted to investigate different stages of the star formation process, from molecular cloud formation to single protostellar collapse. The simulations were performed using AstroBEAR, a state-of-the-art, multiphysics, adaptive mesh refinement code for astrophysical fluid dynamics. In each of the cases, the fluid dynamical properties of the potentially star forming gas were investigated to reveal the relative roles of gravity, magnetic fields, turbulence, and shocks. The models successfully produce many of the structural characteristics of star forming regions. While the simulations modeled isolated, or semi-isolated, phases of the star formation process, cumulatively they represent over 5 orders of magnitude change in spatial scale. Insights provided from this work will aid the development and interpretation of the next generation of simulations – those which will model star formation *through* the phases using self-consistent, hierarchical frameworks.

# Contributors and Funding Sources

This work was supported by a dissertation committee consisting of Professors Adam Frank (advisor), Dan Watson, and Segev Benzvi from the Department of Physics and Astronomy, Professor Doug Kelley from the Department of Mechanical Engineering, and Professor Doug Haessig from the Department of Mathematics. The thesis research was financially supported through the National Science Foundation by grant number AST-0807363, Space Telescope Science Institute by the grants HST-AR-11251.01-A and HST-AR-12128.01-A, the Department of Energy by grant number DE-SC0001063, and the Laboratory for Laser Energetics at the University of Rochester by the Horton Fellowship. Computational resources were provided by the Center for Integrated Research Computing at the University of Rochester and the Extreme Science and Engineering Discovery Environment (XSEDE), which is supported by the National Science Foundation through grant number OCI-1053575.

# List of Tables

3.1	Suite of simulations. . . . .	46
3.2	Thermal and gravitational timescales for the ambient medium, along with the simulation times for the different runs. . . . .	52
4.1	The suite of simulations. . . . .	77
4.2	Analysis region for the different runs. . . . .	108
5.1	Suite of simulations. . . . .	123

# List of Figures

1.1	Hierarchical Star Formation in the Orion Nebula. . . . .	7
2.1	AMR mesh and corresponding tree. . . . .	21
2.2	Growth rate of the Jeans instability for 1D flow. . . . .	28
2.3	The density profile of a marginally-stable Bonnor-Ebert sphere as a function of $\xi$ in log-log space. . . . .	29
2.4	Density and velocity map of the newly incorporated outflow-feedback module in AstroBEAR. . . . .	38
3.1	Schematic of the mesh with an octant of the Bonnor-Ebert sphere located at (0,0,0). . . . .	44
3.2	Radial density profiles for the Sparse case. The different profiles are calculated at different sound crossing times of the sphere, $t_{sc}$ . . . . .	47
3.3	Radial velocity profiles for the Sparse case. . . . .	48
3.4	Radial density profiles for the Classic case, over time. . . . .	50
3.5	Radial velocity profiles for the Classic case, over time. . . . .	51
3.6	Density profiles for the Matched run, $\rho(R_{BE}) = \rho_{amb}$ , over time. . . . .	53
3.7	Radial velocity profiles for the Matched run, $\rho(R_{BE}) = \rho_{amb}$ , over time. . . . .	54
3.8	Density profiles for Run 1/3, over time. The legend is time in units of the sphere's sound-crossing time, $t/t_{sc}$ . . . . .	57
3.9	Radial velocity profiles for Run 1/3, over time. . . . .	58

3.10	Density profiles for Run 1/10, $\rho_{amb} = \rho(R_{BE})/10$ , over time. . . . .	60
3.11	Radial velocity profiles for Run 1/10, $\rho_{amb} = \rho(R_{BE})/10$ , over time. . . . .	61
3.12	Radial velocity profiles for Run 1/30, $\rho_{amb} = \rho(R_{BE})/30$ , over time. . . . .	62
3.13	Density profiles for Run 1/30, $\rho_{amb} = \rho(R_{BE})/30$ , over time. . . . .	63
3.14	Variation of the non-dimensional radius ( $\xi$ , Eqn. 2.31) with time for Run 1/30. . . . .	64
3.15	Pressure perturbation induced at the surface of the sphere as a function of time, as derived from the atmospheric settling model. . . . .	69
4.1	Physical model . . . . .	76
4.2	Mass-weighted vorticity histograms at $t = 1 \text{ Myr}$ . . . . .	80
4.3	Final mass distribution of protoclusters as a function of formation time, $t_{sink}$ . . . . .	86
4.4	Masses of the various sink particles at 1 $\text{Myr}$ after their formation with corresponding final masses. . . . .	88
4.5	Mass-weighted vorticity histograms for the $\theta = 60^\circ$ case at early and late times. . . . .	89
4.6	Column density map for the $\theta = 0^\circ$ case. . . . .	91
4.7	Streamline plot of $B_x$ and $B_z$ components of the magnetic field averaged along $y$ as shown in the $x - z$ plane for the $\theta = 0^\circ$ case. . . . .	92
4.8	Column density map for the $\theta = 15^\circ$ case. . . . .	95
4.9	Column density map for the $\theta = 60^\circ$ case. . . . .	97
4.10	Average $\beta^{-1}$ map for the $\theta = 0^\circ$ case (see Eqn. 4.9 for definition). . . . .	99
4.11	Column $\beta^{-1}$ map for the $\theta = 15^\circ$ case. . . . .	101
4.12	Column $\beta^{-1}$ map for the $\theta = 60^\circ$ case. . . . .	103
4.13	Pressure vs. density histograms for the $\theta = 0^\circ$ case. . . . .	104
4.14	Pressure vs. density histograms for the $\theta = 15^\circ$ case. . . . .	106
4.15	Pressure vs. density histograms for the $\theta = 60^\circ$ case. . . . .	107
4.16	Energy spectra for the various runs. Shown are the kinetic ( <i>smooth lines</i> ), magnetic ( <i>dashed</i> ), and gravitational energies ( <i>fine-dashed</i> ) over time (in- creasing in time from dark to light). . . . .	109
4.17	Diagram of the magnetic ring model. . . . .	114

5.1	Mechanisms for generating filaments normal to magnetic field lines. . . . .	119
5.2	Model diagrams. . . . .	122
5.3	The fluid variables across hydrodynamic, oblique shocks. . . . .	126
5.4	The fluid variables across MHD, oblique shocks. . . . .	128
5.5	Density plots of the six finite colliding flows runs, with overlaid velocity vectors and magnetic field lines. . . . .	130
5.6	Temporal evolution of the $\beta = 1$ , $\theta = 30^\circ$ case. . . . .	132
5.7	Temporal evolution of the $\beta = 1$ , $\theta = 60^\circ$ case. . . . .	132
5.8	Temporal evolution of the $\beta = 10$ , $\theta = 30^\circ$ case. . . . .	134
5.9	Temporal evolution of the $\beta = 10$ , $\theta = 60^\circ$ case. . . . .	134
5.10	Evolution of the 3D $\beta = 10$ , $\theta = 60^\circ$ case, with self-gravity. . . . .	135
5.11	Potential reorientation mechanisms for finite, oblique, MHD colliding flows. . . . .	137
5.12	Resolution study of the $\beta = 10$ , $\theta = 60^\circ$ case. . . . .	139
5.13	Total scaled magnetic energy over time for three different resolutions. . . . .	139
6.1	Column density map of a molecular cloud formed via magnetized, sheared colliding flows. . . . .	143
6.2	Density isocontours of generated molecular cloud complex. . . . .	143
6.3	Reorientation of a shock confined filament. . . . .	145
6.4	A comparison of radial density profiles of collapsing Bonnor-Ebert spheres for compression-wave induced collapse vs. forced perturbation. . . . .	146
6.5	Cloud-to-core star formation simulation feedback loops. . . . .	147

# List of Acronyms

<b>AMR</b>	adaptive mesh refinement
<b>CTU</b>	corner transport upwind
<b>ISM</b>	interstellar medium
<b>KH</b>	Kelvin-Helmholtz
<b>MHD</b>	magnetohydrodynamics
<b>NTSI</b>	non-linear thin shell instability
<b>TI</b>	thermal instability
<b>RT</b>	Rayleigh-Taylor
<b>YSO</b>	young stellar object
<b>BE</b>	Bonnor-Ebert
<b>SIS</b>	singular isothermal sphere
<b>HSE</b>	hydrostatic equilibrium
<b>PDF</b>	probability density function
<b>CDM</b>	column density map
<b>UV</b>	ultraviolet
<b>CNM</b>	cold nuclear medium
<b>WNM</b>	warm nuclear medium
<b>IMF</b>	initial mass function
<b>RHS</b>	right hand side
<b>LHS</b>	left hand side

<b>FS</b>	fast shock
<b>SS</b>	slow shock
<b>CD</b>	contact discontinuity

# Chapter 1

## Introduction

Star formation has been ongoing throughout cosmic history. It is occurring both locally in the universe today (within the Milky Way and its nearest neighbors), and signatures of early star formation epochs are traceable to the distant past. With each successive generation of stars, the environments from which they form change (e.g. through supernovae enrichment), and thus, potentially the dominant mechanisms involved in their formation. In the local universe at least, a paradigm has emerged that identifies the following key physical components of star formation: gravitational fragmentation, magnetic field amplification and dissipation, turbulence, fluid instabilities, and feedback. The relative dominance and contributions of these processes, however, are not yet fully determined (both across spatial scales, as well as time at a fixed scale).

### 1.1 Early, Quasi-static Models of Star Formation

At the simplest level, star formation begins when the self-gravity of a single protostellar *core* (i.e. the precursor of a protostar – a quasi-spherical ball of gas, roughly  $.1\text{ pc}$  across) overwhelms the local supportive forces within the gas, which include thermal and turbulent pressure, magnetic fields, and rotation. This widely accepted view that star formation

results from the gravitational contraction of interstellar gas is not new. Indeed, this concept dates back many centuries, having been proposed by Newton in 1692 following publication of his Universal Law of Gravitation (Larson, R. B., 2003). Observational evidence that supports this claim, however, did not surface until only about 50 years ago.

The first series of observations that connected star formation to gravitational contraction of gas in the interstellar medium (ISM) seemed to indicate that star formation was occurring through a quasi-static process. Dark ‘voids’ were detected, so dense that they obscured visible light, and thus appeared as holes in the night sky (Bok, 1948). These ‘Bok globules’ were later identified as the earliest evolutionary state of newly forming stars (i.e. *protostars*). Far-infrared continuum observations (Ward-Thompson et al., 2002) and millimeter-wave spectroscopic studies (Jessop & Ward-Thompson, 2001) indicated that many of the Bok globules were heated externally by the interstellar radiation field, rather than internally as would be expected by an embedded, gravitationally contracting protostar. Indeed, their inferred central temperatures were very cold, only  $\sim 10\text{ K}$  (Ward-Thompson et al., 2002). Some of the Bok globules appeared massive enough to be gravitationally bound (Myers & Benson, 1983), as well as in an early state of condensation or collapse (Tafalla et al., 1998; Lee et al., 1999). That the measured density profiles of some these objects seemed to also closely match those predicted by hydrostatic equilibrium models (Bacmann et al., 2000; Alves et al., 2001), provided further evidence that these “*pre-protostellar cores*” were evolving quasi-statically toward a state of gravitational instability, and thus, star formation.

Beyond the scale of individual pre-stellar cores, observations of molecular clouds seemed to indicate that they too were in a state of approximate quasi-static equilibrium. While clouds contain both starless *and* star-forming pockets of dense gas, they do not contain nearly enough of the later, as would be theoretically predicted based on their masses and temperatures. That is to say, the *star formation efficiency* of molecular clouds, i.e. the fraction of the cloud that is actively forming stars within a given dynamical time, is very small (typically  $\sim 1 - 3\%$ , Lada et al., 2010). Thus, various mechanisms have been invoked

that could provide support to molecular clouds against their own self-gravity, and hence, result in their apparent quasi-static equilibrium configuration.

One of these mechanisms is turbulence, which appears to be in rough equipartition with gravity on the scales of molecular clouds (Larson, R. B, 1981; Myers & Benson, 1983). The first line of evidence that molecular clouds are turbulent is that molecular line emission *broadens* within molecular clouds. This is widely attributed to turbulent motions within the gas, which appear to be supersonic in all but the smallest globules (Larson, R. B, 1981; Myers & Benson, 1983). Second, there appears to be a scale-dependence of the measured linewidths, similar to classical Kolmogoroff scaling relations (i.e.  $\sigma \propto L^{0.38}$ , where  $\sigma$  is the inferred velocity dispersion from molecular linewidths and  $L$  is the length of a given region under consideration; Larson, 1981). However, it is unclear how closely the turbulent motions within molecular clouds actually resemble classical eddy turbulence. For instance, the Kolmogoroff spectrum describes the energy cascade for turbulent, *incompressible* fluids. When supersonic motions are present (as in the ISM), energy can be dissipated by shocks in addition to viscosity. Thus, this empirical scaling relation (known as the first of “Larson’s laws”) may be coincidental, although similar linewidth-size relations have been confirmed by many groups, as well as in many molecular clouds (Larson, R. B, 1981; Myers, 1983; Falgarone et al., 1992; Goodman et al., 1998; Myers & Gammie, 1999). Third, the sub-structure of molecular clouds is often self-similar and hierarchical (Falgarone et al., 1992), as would be expected from a scale-free, turbulent cascade. Indeed, the fractal nature of molecular clouds has been explored, with results indicating that at least some molecular clouds do exhibit this type of scale-free structure (Falgarone et al., 1991; Simon, 1997).

Another mechanism is magnetic support. Magnetic fields have long been invoked in the quasi-static paradigm of star formation, whereby clouds and their embedded cores evolve quasi-statically via ambipolar diffusion, a process by which the gas slowly decouples from the magnetic field (Mouschovias, 1979). However, evidence to support this scenario is inconclusive, as measuring the magnetic field strength within molecular clouds and cores is extremely challenging. Such measurements are largely provided by the Zeeman effect, but

this method yields only upper limits to the field strength (Heiles et al., 1993; Bourke et al., 2001). On the molecular cloud scale, magnetic field estimates seem to indicate that the field alone is unlikely to be strong enough to counterbalance gravity (Crutcher, 1999; Heiles & Troland, 2005). On the pre-stellar core scale, the evidence that cores are magnetically supported is mixed (c.f. Ward-Thompson, 2002b).

Now that we have established some of the observational motivations for the quasi-static nature of pre-stellar cores and their encompassing molecular clouds, let us turn to early theoretical models of star formation that embody these concepts. To explore the evolution of initially quasi-static protostellar cores, two theoretical methods arose around the late 1960s and 70s: analytical similarity solutions that described simplified initial conditions, and early numerical simulations that solved the full nonlinear system of fluid equations. In both cases, the starting conditions were spherical, isothermal mass distributions. That the core be treated isothermally was supported by earlier work by Hayashi (1966), which showed that the collapse should proceed isothermally until the opacity limit of the gas was reached ( $\rho \sim 10^{-13} \text{ g cm}^{-3}$ ), at which point the temperature should increase due to radiative trapping.

The similarity solutions yielded the collapse profiles of the simplest spherical structures – those of uniform density or simple polytropic density laws (i.e.  $\rho \propto P^\Gamma$ , where  $P$  is the thermal pressure and  $\Gamma$  is the adiabatic index; Penston, 1969, Shu, 1977). Early numerical simulations of these same initial conditions revealed that the collapse was actually highly non-homologous, regardless of choice of boundary conditions (Bodenheimer & Sweigart, 1968; Penston, 1969b; Larson, 1979). Additionally, early simulations revealed that the collapse proceeded through a “first hydrostatic core” phase, which formed once the inner regions of the collapsing sphere became optically thick (i.e. once  $\rho > 10^{-13} \text{ g cm}^{-3}$ ). At that point, radiative heating halted the collapse of the core, resulting in bounding, spherical “accretion” shocks that continued to deliver material onto the central, hydrostatic region until it became dense enough that a second collapse was triggered (Larson, 1979).

As computing power increased, so did the flexibility of adding increasingly complex

physics solvers to these early-type simulations of single star formation. Over the years, many groups have continued in this direction, exploring the collapse dynamics of polytropic spheres under various physical conditions: rotation (Banerjee et al., 2004), magnetic fields Banerjee & Pudritz (2006), imposed turbulent velocity perturbations (Offner et al., 2008). Indeed, these simulations have taught the astronomical community a great deal about the dynamics of collapsing protostellar cores, although these models now appear to have a few glaring inconsistencies. The first is that the star formation community is largely moving away from the quasi-steady state viewpoint of molecular clouds (Ward-Thompson, 2002; Larson, R. B., 2003). Instead, the community is embracing the apparent *dynamic* nature of molecular clouds, which do not physically appear to be in any type of equilibrium state – they are wind-blown in appearance, much like terrestrial clouds, and contain a rich tapestry of turbulent substructure. So, the first inconsistency can be stated as: how do you get quasi-static initial conditions of star formation from a dynamic molecular cloud environment?

Second, the hierarchical structure present in molecular clouds strongly suggests that the formation and evolution of these self-similar structures may play an important role in star formation. Indeed, it is now widely accepted that protostellar cores reside within larger spherical *protocluster* “clumps” ( $r \approx 1 - 10 \text{ pc}$ ), which reside within elongated, cylindrical structures of molecular material, known as *filaments*. At the largest scale of star formation, we have the molecular cloud itself (typically  $10 - 100 \text{ pc}$  across), representing the accumulated aggregate of filaments, clumps, and cores. Understanding how these various structures form, and how they relate to the star formation process is of current interest to the star formation community. Yet, these questions can fundamentally not be pursued using such simplified initial conditions as isolated, collapsing spheres.

Third, and highly related to the previous point, is that simulations of isolated spherical collapse largely decouple the sphere from its encompassing environment via some sort of discontinuity in the fluid variables (such as a large jump in density so that the ambient medium is extremely sparse, and thus, dynamically quiescent). Indeed, observations indicate the necessity of considering the ambient environment: the overwhelming majority of

stars form in complex, crowded environments (Fig. 1). In the cluster environment, star formation becomes highly dynamic, as protostellar cores and young-stellar objects interact through *feedback*, which can take the form of ionizing radiation, winds and outflows. While the detailed role of feedback in the star formation process is not yet fully determined, it is widely regarded as one of the mechanisms by which star formation is *regulated* in stellar nurseries.

## 1.2 Dynamic Modes of Star Formation

Star formation models that begin with quasi-static initial conditions may more or less approximate quiescent regions where star formation proceeds in an isolated fashion (the canonical example being the Taurus molecular cloud complex, although there is evidence to support the dynamical nature of star formation even there, see Hartmann, 2003). However, for many years, the star formation community has been moving away from this paradigm toward one that embraces the *dynamic* nature of the larger molecular cloud environment. Such studies are not only motivated by the limitations of isolated, star formation models (discussed previously), but also by the realization that the ‘problem’ of the low star formation efficiency of molecular clouds can be circumvented if molecular clouds are in fact transient structures (Larson, R. B., 1981; Larson, R. B., 2003). Indeed, a new school of thought has emerged within the star formation community, in sharp contrast to the ‘long-lived, quasi-static’ molecular cloud camp of old (Mouschovias, 1979; Shu et al., 1987a): the ‘short-lived, *dynamic*’ molecular cloud paradigm (Ballesteros-Paredes, 2000; Hartmann et al., 2001b). In this framework, molecular clouds are believed to form out of the background ISM via turbulent fluid dynamical instabilities, form stars *immediately* in the densest regions contained within them, and then disperse within 1-2 dynamical times. Evidence for this transient molecular cloud scenario comes from the observation that nearly *all* molecular clouds are actively forming stars, and that the age span of these forming stars is *very small* (on the order of the cloud’s sound crossing time, defined by its length divided by its sound



**Figure 1.1:** The Orion Nebula provides a good example of the hierarchical structure typical of active star forming regions. Young stars, still heavily embedded within the surrounding complex of gas and dust, are shown in this map as purple points. NASA/HUBBLE.

speed; Elmegreen, 2000; Hartmann et al. 2001b; Hartmann, 2003).

To model the formation of molecular clouds and their embedded pre-stellar structures in this dynamical framework, some of the first simulations focused on the evolution of the turbulent ISM. For instance, Vazquez-Semadeni et al. (1995) modeled the ISM on *kpc* scales. These simulations used periodic boundary conditions, seeded turbulence via perturbations in the velocity field, and included self-gravity, stellar heat sources, and radiative cooling. Once a given density threshold was reached in localized regions of the flow, a heat source was turned on in that region, mimicking the formation of an O star. This heat source produced expanding numerical H II regions, which acted as additional sources of turbulence in the simulations. One of the main results from this study was that cold, high-density structures, similar to molecular clouds, naturally formed in the flow. Closer inspection of these high-density regions revealed that they were in rough pressure equilibrium with the lower density and warmer surrounding environment, and that they were forming at the intersection of converging flows.

While models of the turbulent ISM have in many ways advanced understanding of star formation within dynamical environments (see Mac Low & Klessen, 2004 for a detailed review), the seemingly artificial imposed turbulence in the initial conditions, without a clear understanding of the origin of said turbulence, is undesirable. One model that has since gained wide-spread support for *self-consistently* generating turbulent molecular clouds is the ‘colliding flows’ model (Audit & Hennebelle, 2005; Vazquez-Semadeni et al., 2011; Heitsch et al. 2009, Carroll-Nellenback et al., 2014; Fogerty et al. 2016). Instead of forcing turbulence, the colliding flows model naturally generates turbulent molecular clouds through the excitation of various fluid instabilities in the post-shock region between two converging, supersonic streams of gas. While most colliding flows simulations represent an idealized version of what would likely constitute actual colliding flows in nature, the colliding flows paradigm does have a fair degree of observational and theoretical motivation. The boundaries of molecular clouds are highly irregular, resembling swept up gas from turbulent flows (Falgarone et al., 1991). Atomic inflows have been observed converging onto molecular clouds (Ballesteros-

Paredes et al., 1999; Brunt, 2003), and as stated previously, simulations of the turbulent ISM show dense, molecular gas often forming at the intersection of colliding gas streams (Vazquez-Semadeni et al., 1995; Passot et al., 1995).

Many observationally consistent features are born out of colliding flows simulations. First, they naturally produce clouds that are short-lived. The turbulent origin of molecular clouds in this framework means that once enough gas has been swept up and cooled to high-enough densities to be effectively molecular, star formation can proceed immediately. That is, star formation is intimately tied to cloud formation in this paradigm. Second, turbulence is self-consistently generated as gas is shocked, heated, and cooled within the collision region between flows. Fluid instabilities associated with this process include the Rayleigh-Taylor, Kelvin-Helmholtz, thermal, and nonlinear thin shell instabilities. Third, the post-shock fluid instabilities seeded by colliding flows produce hierarchical structure similar to those found in physically-realized molecular clouds. Filaments and embedded clumps naturally arise in molecular clouds formed by this mechanism. However, detailed statistics on the formation of individual stars forming in these clumps are still difficult to derive, given current resolution limitations (i.e. to simultaneously model the entire molecular cloud complex, as well as individual forming protostars, remains computationally challenging). Indeed, this is one of the future directions star formation research will follow – accurately capturing the dynamics of forming protostellar clusters that form within self-consistently generated molecular clouds using high resolution, multiphysics simulations.

In summary, modern day theories view star formation as the combined result of gravitational and turbulent fragmentation, subjected to a wide range of physical processes, such as magnetic fields, fluid dynamical instabilities, and feedback. One of the main goals in the field is to understand the interconnections between the various structures associated with this fragmentation, as well as the physical processes operating within (and between) each of these phases of the gas. In a phrase, the star formation paradigm has evolved from a quasi-static theory into a dynamic, *multiscale*, *multiphysics* framework.

## 1.3 Modeling the Dynamical Evolution of Clouds, Cores, and Filaments with AstroBEAR

The main body of work presented in this thesis focuses on early evolutionary epochs of star formation. The simulations were conducted with the numerical code, AstroBEAR (Cunningham et al., 2009; Carroll-Nellenback et al., 2013), and included magnetic fields, self-gravity, heating and cooling processes relevant to the ISM, and sink particles (see Ch. 2). Feedback was not included in the main body of work, but is currently being developed in AstroBEAR for future directions (c.f. Ch. 2, Sec. 2.6.1-2.6.2, and Ch. 6, Sec. 6.2). Instead of modeling all scales simultaneously (which is computationally prohibitive), this work focuses on three different phases of evolution: isolated protostellar collapse under realistic environmental conditions (Ch. 3), molecular cloud formation and evolution by magnetized, sheared colliding flows (Ch. 4), and the dynamics of prestellar filaments formed by MHD shock processes (Ch. 5).

In the protostellar collapse chapter, simulations are presented that explore the evolution of single protostellar cores due to purely gravito-hydrodynamical interactions with their ambient environments. The emphasis of this work therefore was on investigating the relationship between embedded protostellar cores and their encompassing environments, in contrast to previous studies that have largely focused on forced collapse dynamics of protostellar cores through applied perturbations that initiated collapse (such as the reduction of thermal energy within the core). To study this relationship, protostellar cores were embedded within ambient media of different masses and the simulations were allowed to evolve dynamically. The results of this work indicate that gravitational instability of embedded protostars can be driven by the dynamics of the ambient medium alone. These findings underscore the importance of considering the boundary between protostars and their environments in numerical experiments of isolated star formation.

The work on molecular cloud formation investigates the dynamics of molecular clouds formed in magnetized environments of varying degrees of shear, using a colliding flows setup. Previous

colliding-flows models of molecular cloud formation largely focused on the formation of clouds between head-on colliding flows. Thus, exploring the effect of shear in colliding flows (induced by oblique shocks at the collision interface) was an important next step in the investigation of cloud generation by the colliding flows mechanism. Moreover, regions of high shear can be found within the Galaxy (for instance, at spiral arm/inter-arm boundaries, induced by galactic rotation), and thus, it is of interest to understand whether molecular clouds can form and produce stars in such environments. The results of this study indicate that magnetic field amplification within turbulent molecular clouds greatly impedes star formation, and this amplification increases as shear increases in the cloud environment. These findings support the presence of dissipation mechanisms in high-shear environments, capable of removing amplified magnetic fields so that star formation can proceed.

Lastly, filament formation by MHD shock dynamical processes was explored using a similar colliding flows model as described previously. In this work, an MHD shock process was identified capable of *reorienting* filaments (formed in the post-shock regions between the flows) such that they lie normal to the environmental magnetic field. The dynamics of this process is explored and potential mechanisms that explain the reorientation mechanism are presented in this thesis. Indeed, that an MHD shock process may produce such an orientation is curious. Not only are supersonic flows ubiquitous in the interstellar medium (Brunt, 2003; Kirk et al., 2013; Fernández-López et al., 2014), but such an orientation between filaments and magnetic fields is widely observed in young star forming regions (André et al., 2010; Arzoumanian et al., 2011; Polychroni, 2012; Lee et al., 2014). The origin of this orientation, as well as its significance to the star forming process, is currently unknown. The results of this work indicate that MHD shock processes may play a role in the formation of this unique star forming structure.

The overarching goal of this thesis was to investigate the dominant physical processes operating within protostellar cores, filaments, and molecular clouds, under dynamic environmental conditions. It is hoped this work will support future, fully multiscale models of star formation through its analysis of these phases on their respective scales. Indeed, new methodologies are being

developed that will make the next generation of star formation simulations computationally feasible (those that will self-consistently model star formation, from molecular cloud formation through cluster formation and evolution). This thesis is organized as follows. The key numerical methods used throughout the doctoral research will be described in Ch. 2, the main numerical experiments will be presented in Ch.3-5, and the thesis will conclude with a summary of key results and future directions in Ch. 6.

## Chapter 2

# Numerical Methods

### 2.1 Introduction

The advent of high-performance numerical methods has ushered in a new era of astrophysics research. These methods allow the exploration of physical systems when theory or observations alone would fall short. Simulations are not fully isolated, however: observations and theory directly inform numerical models, as well as motivate the development of new methodologies. Thus, computational astrophysics lies at the crossroads between the observational and theoretical branches of research.

In the case of star formation, adaptive mesh refinement and modern shock capturing techniques have provided the means for modeling the *dynamical evolution* of star-forming gas. With these methods, modern codes are able to accurately model compressible gas dynamics over many orders of magnitude change in spatial scale. Moreover, the addition of increasingly complex physics solvers to astrophysical fluid codes (e.g. self-gravity, radiation transfer, chemistry) provides a test-bed for detailed theoretical models and predictions, as well as observations. This *multiscale, multiphysics* nature of modern numerical methods makes them especially conducive to the study of star formation, which occurs over many decades of spatial scales and under the influence of a wide variety of physical processes.

The numerical research in this dissertation was conducted using AstroBEAR (Cunningham et al., 2009; Carroll-Nellenback et al., 2013), a massively parallelized, multiphysics, adaptive mesh refinement code for astrophysical fluid dynamics. AstroBEAR is a ‘living code’, in that it is actively developed, tested (c.f. Poludnenko et al., 2002; Cunningham et al., 2009; Kaminski et al., 2014), and documented<sup>1</sup> by the computational astrophysics research group at the University of Rochester, led by Dr. Adam Frank.

The focus of the present chapter is on the numerical methods by which AstroBEAR solves the equations of hydrodynamics and magnetohydrodynamics including source terms, modules and tests that have been developed for AstroBEAR throughout the course of this thesis research. The discussion will be limited to those methods directly related to the work presented in this dissertation.

## 2.2 Governing Equations

AstroBEAR solves the equations of ideal magnetohydrodynamics (MHD) in multiple dimensions on a Cartesian, adaptive mesh refinement mesh. In conservative form, the full (3D) system of equations is given by:

$$\frac{\partial}{\partial t}\mathbf{Q} + \frac{\partial}{\partial x}\mathbf{F}(\mathbf{Q}) + \frac{\partial}{\partial y}\mathbf{G}(\mathbf{Q}) + \frac{\partial}{\partial z}\mathbf{H}(\mathbf{Q}) = \mathbf{S}(\mathbf{Q}) \quad (2.1)$$

where  $\mathbf{Q}$  is the vector of conserved variables,

---

<sup>1</sup>See AstroBEAR’s documentation here: <https://astrobear.pas.rochester.edu>

$$\mathbf{Q} = \begin{bmatrix} \rho \\ \rho v_x \\ \rho v_y \\ \rho v_z \\ \mathcal{E} \\ B_x \\ B_y \\ B_z \end{bmatrix} \quad (2.2)$$

$\mathbf{F}$ ,  $\mathbf{G}$ , and  $\mathbf{H}$  are the corresponding fluxes of fluid variables along  $\hat{x}$ ,  $\hat{y}$ , and  $\hat{z}$ ,

$$\mathbf{F}(\mathbf{Q}) = \begin{bmatrix} \rho v_x \\ \rho v_x^2 + P + \mathbf{B}^2/2 - B_x^2 \\ \rho v_y v_x - B_x B_y \\ \rho v_z v_x - B_x B_z \\ (\mathcal{E} + P + \mathbf{B}^2/2)v_x - B_x(\mathbf{B} \cdot \mathbf{v}) \\ 0 \\ -E_z \\ E_y \end{bmatrix} \quad (2.3)$$

$$\mathbf{G}(\mathbf{Q}) = \begin{bmatrix} \rho v_y \\ \rho v_x v_y - B_y/B_x \\ \rho v_y^2 + P + \mathbf{B}^2/2 - B_y^2 \\ \rho v_z v_y - B_y B_z \\ (\mathcal{E} + P + \mathbf{B}^2/2)v_y - B_y(\mathbf{B} \cdot \mathbf{v}) \\ E_z \\ 0 \\ -E_x \end{bmatrix} \quad (2.4)$$

$$\mathbf{H}(\mathbf{Q}) = \begin{bmatrix} \rho v_z \\ \rho v_x v_z - B_z B_x \\ \rho v_y v_z - B_z B_y \\ \rho v_z^2 + P + \mathbf{B}^2/2 - B_z^2 \\ (\mathcal{E} + P + \mathbf{B}^2/2)v_z - B_z(\mathbf{B} \cdot \mathbf{v}) \\ -E_y \\ E_x \\ 0 \end{bmatrix} \quad (2.5)$$

and  $\mathbf{S}$  is the vector of source terms,

$$\mathbf{S} = \begin{bmatrix} S_\rho \\ S_{\rho v_x} \\ S_{\rho v_y} \\ S_{\rho v_z} \\ S_{\mathcal{E}} \\ S_{B_x} \\ S_{B_y} \\ S_{B_z} \end{bmatrix} \quad (2.6)$$

Note, source terms can also take the form of geometric corrections, when the system is transformed into a non-Cartesian coordinate system. In the above equations, the variables have their usual meanings, namely,  $\rho$  is the mass density,  $\mathbf{v}$  is the velocity vector,  $\mathcal{E}$  is the total energy per unit volume,  $\mathbf{B}$  is the magnetic field,  $P$  is the thermal pressure, and  $\mathbf{E}$  is the electric field. As the last three equations in this system result from Faraday's law,

$$\frac{\partial}{\partial t} \mathbf{B} + \nabla \times \mathbf{E} = \mathbf{0} \quad (2.7)$$

the system has the additional constraint that initially solenoidal magnetic fields remain divergence-free:

$$\nabla \cdot \mathbf{B} = 0 \quad (2.8)$$

Finally, the equations of ideal MHD are brought to closure by Ohm's law for a perfectly conducting fluid,

$$\mathbf{E} = -\mathbf{v} \times \mathbf{B} \quad (2.9)$$

and a suitable equation of state, such as the polytropic equation of state for an ideal gas,

$$P = (\gamma - 1)\left(\mathcal{E} - \frac{\rho \mathbf{v} \cdot \mathbf{v}}{2} - \frac{\mathbf{B} \cdot \mathbf{B}}{2}\right) \quad (2.10)$$

where  $\gamma$  is the ratio of specific heats.

AstroBEAR solves the above fluid equations using an operator-split approach (viz. later sections on source terms, as well as Cunningham et al., 2005 for details) combined with an upwind, Godunov-type finite-volume scheme that is directionally-split and second order accurate in space and time. To illustrate the basic finite-volume approach, let us consider a directionally-*unsplit* version of the method. Further, as the *homogeneous* version of the fluid equations are solved in operator-split schemes, let us consider the following prescription for advancing the conserved fluid variables forward in time, which results from discretizing Eqn. 2.1 with  $\mathbf{S} \equiv \mathbf{0}$ :

$$\begin{aligned} \mathbf{Q}_{i,j,k}^{t+\Delta t} = \mathbf{Q}_{i,j,k}^t &+ \frac{\Delta t}{\Delta x} (\tilde{\mathbf{F}}_{i-1/2,j,k} - \tilde{\mathbf{F}}_{i+1/2,j,k}) + \frac{\Delta t}{\Delta y} (\tilde{\mathbf{G}}_{i,j-1/2,k} - \tilde{\mathbf{G}}_{i,j+1/2,k}) \\ &+ \frac{\Delta t}{\Delta z} (\tilde{\mathbf{H}}_{i,j,k-1/2} - \tilde{\mathbf{H}}_{i,j,k+1/2}) \end{aligned} \quad (2.11)$$

The main numerical procedure for updating  $\mathbf{Q}$  in this equation consists of calculating the fluxes across cell boundaries, taking a volume-weighted average of these fluxes ( $\tilde{\mathbf{F}}$ ,  $\tilde{\mathbf{G}}$ ,  $\tilde{\mathbf{H}}$ ), and advancing the  $\mathbf{Q}$  array to the next time step ( $t + \Delta t$ ). Note, the  $\mathbf{Q}$  array is collated at cell centers, which are indexed in this equation by  $i, j, k$  for the  $x, y$ , and  $z$  directions. In split form, the code updates  $\mathbf{Q}$  along each dimension independently.

To compute the flux at each cell interface, the data are spatially reconstructed along the inter-cell boundary to second-order accuracy using one of AstroBEAR's pre-compiled reconstruction methods. These include the MUSCL (Van Leer, 1979), piece-wise parabolic (Colella & Woodward, 1984), and piece-wise hyperbolic methods (Marquina, 1994). The user can choose which reconstruction method to use at run-time, along with their choice of any number of flux-limiters. Once the

data are reconstructed along cell boundaries, the upwinded flux is computed via solution of the local Riemann problem (i.e. defined by the reconstructed left and right states along the discontinuity at the inter-cell boundary). This is achieved using one of AstroBEAR’s many Riemann solvers, which include the Exact, HLLC (Einfeldt et al., 1991), and HLLD (Miyoshi & Kusano, 2005) methods. These solvers are also pre-compiled, and thus, can be easily selected by the user at run time. The solution is then updated temporally using a second-order accurate integration scheme, such as a MUSCL-Hancock predictor-corrector scheme or a two-step Runge-Kutta approach, both of which are implemented in AstroBEAR (Cunningham et al., 2009).

Finally, to maintain the divergence-free constraint of the magnetic field (Eqn. 2.8), the normal component of the magnetic field is updated at cell faces according to a corner transport upwind scheme (Cunningham et al., 2009). In this method, the magnetic field components normal to cell faces are computed using interpolated electric field components along cell edges. Once calculated, these values replace those computed by the Godunov-scheme at cell centers, and are used to update the total volume averaged energy  $\mathcal{E}$ .

## 2.3 Adaptive Mesh Refinement in AstroBEAR

This section provides a brief overview of the AMR algorithm in AstroBEAR. For a more complete description of the procedure, the reader is referred to Carroll-Nellenback et al. (2013). It is instructive to begin this section with a quick tutorial of fixed-grid parallelization in AstroBEAR, as a means to introduce terminology. In fixed grid, the (uniform) mesh is divided up into rectangular collections of cells (i.e. patches), which then are divided among processors (one processor per patch, but not necessarily one patch per processor). Each processor is tasked with computing the hyperbolic advance of its own patch(es). The ghost zones (boundary values) for internal patches of the domain are provided by patches that lie adjacent in physical space. Each patch’s physical location within the domain is stored within a computational entity in AstroBEAR called a node. There is a one-to-one

correspondence between nodes and patches. That is, each node contains information about exactly one patch. In addition to a given patch’s location within the domain, a node also contains information about the patch’s dimensions (in index space), and the location of all neighboring (adjacent) nodes. Each processor stores its own node in memory, rather than the whole tree. In contrast to nodes, patches store the actual fluid variables, which are updated both spatially and temporally as the calculation proceeds.

In AMR calculations, the resolution of each patch can now vary (Fig. 2.1). The resolution of a given patch (i.e. its inter-cell spacing,  $dx$ ) is related to the resolution of the coarse grid through the equation  $dx = (L_x/m_x)2^{-l}$ , where  $l$  is the AMR level (c.f. Fig. 2.1),  $L_x$  is the length of the computational domain, and  $m_x$  is the number of coarse grid cells. That is, each successive level of refinement increases the resolution of a given patch by a factor of two. Finer patches are nested within coarser, parent patches, all the way up to the root grid (which is at the coarsest resolution). In addition to carrying out their own computations, each processor needs to exchange data with processors of neighboring patches. As we will see, this includes communication between nested grids (‘parents’ and ‘children’), adjacent patches of the same level (‘siblings’ and otherwise), and successive patches in time that are spatially coincident. As in fixed-grid, the metadata for each patch, such as its location within the computational domain, its dimensions, and its connections to neighboring patches, are stored within a node. The collection of all nodes comprises the AMR tree (c.f. right-side of Fig. 2.1), which is distributed among processors. AstroBEAR was one of the first patch-based AMR codes to have a distributed AMR tree, thus minimizing the memory required per processor to store the global nodal distribution.

The evolution of the AMR tree occurs both spatially and temporally, as grids are continually generated and destroyed over the course of a simulation. This process follows five steps, which are recursive across AMR levels: Overlaps, Prolongation, Advances, Synchronization, Restriction. In the Overlaps subroutine, the next iteration of level  $l$  grids is calculated. These can be entirely new grids that are born in the domain (i.e. new child grids), or just the next iteration of preexisting child

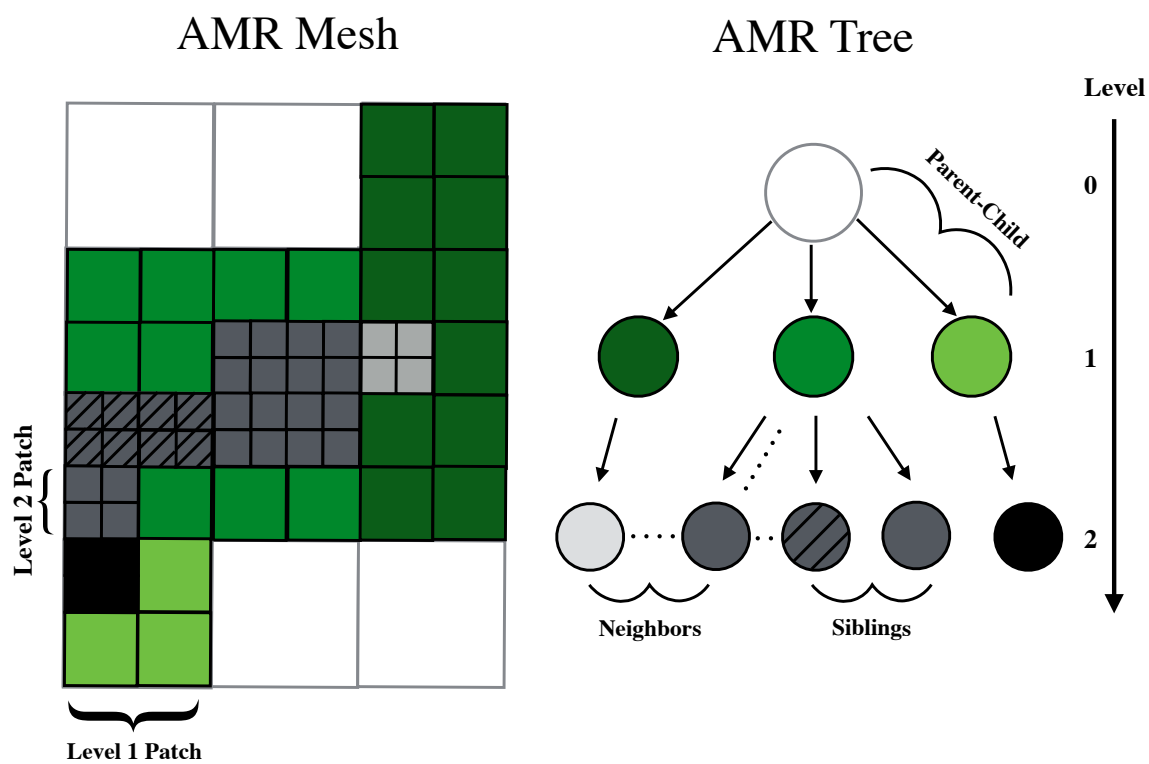


**Figure 2.1:** AMR mesh and corresponding tree. Example communication connections between nodes in the AMR tree (at a fixed time) are shown with dashed lines.

grids, or a blend of the two (i.e. a preexisting child grid that is reshaped). These grids are initialized with a combination of data from their parent grids (through the Prolongation subroutine), as well as their previous iterations. In this way, data is passed between parent and child grids, as well as successive patches that share the same physical location. Through the distributed AMR tree, each processor has access to its own node as well as the spatial and temporal neighbors with which it needs to communicate to perform its calculations. While there are many successive iterations of grids over the course of a typical simulation, only the two most current iterations are stored in the AMR tree at any one time.

After the Overlap and Prolongation steps, new level  $l + 1$  grids can be generated and the grids ( $l, l + 1$ ) advance. Each grid advances at a level-dependant time-step, given by  $\Delta t_{l+1} = \Delta t_l 2^{-l}$ . Thus, after  $2^l$  time-steps, parent and child grids have reached the same time. At this point, data from finer grids are *Restricted* to coarser grids and fluxes are *Synchronized* across grid boundaries. After these steps, the AMR algorithm begins again, starting with the grid-generation subroutines.

The above described AMR grid cycle supports the *simultaneous* advancing of grids across AMR levels. This advancing technique is a key feature of AstroBEAR, and is achieved by inter-level threading of the AMR algorithm. In order to decouple the hyperbolic advance of grids across AMR levels, a mechanism needs to be in place that specifies the values of ghost zones around nested AMR patches. For the initialization of new level  $l + 1$  grids, ghost zones are supplied by the parent level  $l$  grid through prolongation. However, as the child grid advances through smaller time-steps than its parent grid, these zones cannot simply be updated with prolonged data from the parent.

For spatially adjacent patches of a given level, ghost zones can be updated following the hyperbolic advance of the neighboring patch, using the neighbor's updated fluid variables. However, for isolated patches, the choice in ghost zone values is not as obvious. One method is to use the time-derivative of fluid variables on the coarser level grid for the ghost-zone update. However, this can introduce large discretization errors, particularly in the presence of shocks. Another method is to use an *extended* region of ghost zones around level  $l$  patches, essentially mimicking adjacent

level  $l$  patches. In such a case, the number of ghost zones required in each dimension surrounding the patch would be equal to  $n_{ghost}2^l$ , where  $n_{ghost}$  is the number of ghost zones required to take a time-step on level  $l$ . This latter method is implemented in AstroBEAR.

## 2.4 Source Terms: Self-gravity

With self-gravity, the Euler equations become,

$$\frac{\partial \rho}{\partial t} + \nabla \cdot (\rho \mathbf{v}) = 0 \quad (2.12)$$

$$\frac{\partial \rho \mathbf{v}}{\partial t} + \nabla \cdot (\rho \mathbf{v} \mathbf{v} + P) = -\rho \nabla \phi_g \quad (2.13)$$

$$\frac{\partial \mathcal{E}}{\partial t} + \nabla \cdot [\mathbf{v}(\mathcal{E} + P)] = -\rho \mathbf{v} \cdot \nabla \phi_g \quad (2.14)$$

where  $\phi_g$  is the gravitational potential satisfied by Poisson's equation,

$$\nabla^2 \phi_g = 4\pi G(\rho - \bar{\rho}) \quad (2.15)$$

and the total energy density  $\mathcal{E}$  is,

$$\mathcal{E} = \frac{1}{2}\rho v^2 + \epsilon \rho \quad (2.16)$$

(where  $\epsilon$  is the specific internal energy). For ideal gas, the caloric equation of state gives  $\epsilon = P/[(\gamma - 1)\rho]$ , where  $\gamma$  is the ratio of specific heats. Subtracting off the mean density ( $\bar{\rho}$ ) in Equation 2.15 is necessary when solving for the potential on a periodic grid, as it provides an additional condition to close the system of equations. For non-periodic grids, the code sets  $\bar{\rho} = 0$  for this condition.

AstroBEAR can solve the self-gravitating fluid equations (2.12-2.14) using a Strang splitting method + a corner transport upwind (CTU) scheme, or can solve the equations with momentum conservation. Using Strang splitting, the homogeneous versions of the Euler equations are solved during the hydrodynamic steps and the source term equations,  $d\mathbf{q}/dt = \mathbf{s}(\mathbf{q})$ , are solved during the source steps, where  $\mathbf{q}$  is the vector of fluid variables and  $\mathbf{s}$  is the source term vector given by the components on the right-hand side (RHS) of equations (2.12-2.14). Here, a source step of half a time-step is taken on both sides of the hydrodynamic advance step to make the scheme 2nd-order accurate in time. The hydrodynamic advance steps can use any one of many available hyperbolic solvers.

Using just Strang splitting, sink particles (numerical sub-grid algorithms that approximate gravitationally bound and collapsing objects in the grid, see Sec. 2.6) that formed under spherically symmetric conditions would occasionally wander across the grid, even though the net forces on the sink should have been zero. To correct this, strict momentum conservation was enforced across grids. This eliminated the erroneous kicks to the sink particles. To implement a momentum conserving scheme, the fluid equations must be expressed in conservative form. That is, in terms of a flux function  $F$  for which the following relationship holds,

$$\frac{\partial \mathbf{q}}{\partial t} = -\nabla \cdot \mathbf{F} \quad (2.17)$$

For momentum conservation, this flux function follows from forcing the RHS of the momentum equation (2.13) to be equal to the negative divergence of the flux,

$$-\rho \nabla \phi = -\nabla \cdot F \quad (2.18)$$

Using Poisson's equation (2.15) to substitute for  $\rho$  gives,

$$\nabla \cdot F = \left( \frac{\nabla^2 \phi}{4\pi G} + \bar{\rho} \right) \nabla \phi \quad (2.19)$$

which in 1D is equivalent to,

$$\nabla \cdot F = \nabla \cdot \left[ \frac{1}{2} \frac{(\nabla \phi)^2}{4\pi G} + \bar{\rho} \phi \right] \quad (2.20)$$

A similar analysis gives the form of the flux function tensor  $F_{ij}$  for general dimension,

$$F_{ij} = \frac{(\partial_j \phi \partial_i \phi)}{4\pi G} - \delta_j^i \left( \frac{\partial_k \phi \partial_k \phi}{8\pi G} + \bar{\rho} \phi \right) \quad (2.21)$$

The *total* flux (including the Riemann flux calculated across cell boundaries, Eqn. 2.11), is used to update the momenta array during the CTU scheme.

For both the non-momentum conserving and momentum-conserving schemes, the gravitational potential is computed using the HYPRE library, a generalized software package that solves linear systems on massively parallelized computing systems. The stencil for the potential varies depending on the grid dimension and whether it has fixed cell spacing or not. In its simplest form, the 2nd-order accurate discrete version of Equation 2.15 in 1D is

$$\frac{(\phi_{i+1} + \phi_{i-1} - 2\phi_i)}{(\Delta x)^2} = 4\pi G(\rho_i - \bar{\rho}) \quad (2.22)$$

where  $\Delta x$  is the inter-cell spacing. Using a stencil such as this, Hype implicitly solves for the potential on each level. To update the ghost cells of finer-level grids, the time-derivative of the potential ( $\dot{\phi}$ ) from coarser grids is used. Once the new potential is calculated, the source terms are updated.

#### 2.4.1 Testing Self-gravity in AstroBEAR: the Jeans Instability

As a test of AstroBEAR's self-gravity implementation, the growth rate of a 1D Jeans unstable mode was computed with AstroBEAR and compared to its analytical value. Before presenting the results of this test, let us briefly review the derivation of this growth rate. The 1D linearized, self-gravitating

fluid equations are given by,

$$\frac{\partial \rho'}{\partial t} + \rho_0 \nabla \cdot v' = 0 \quad (2.23)$$

$$\rho_0 \frac{\partial v'}{\partial t} = -C_s^2 \nabla \rho' - \nabla \phi' \quad (2.24)$$

$$\frac{\partial^2}{\partial x^2} \phi' = 4\pi G \rho' \quad (2.25)$$

where the background density ( $\rho_0$ ) and gravitational potential are assumed constant, and the velocity is initially zero ( $v_0 = 0$ ). The primed terms in the equations indicate the perturbation in the corresponding variable. By combining these equations, one arrives at the following wave equation in the density perturbation,

$$\frac{\partial^2 \rho'}{\partial t^2} - C_s^2 \nabla^2 \rho' = -4\pi G \rho_0 \rho' \quad (2.26)$$

Looking for plane-wave solutions to this equation,

$$\rho' \propto e^{ikx - \omega t} \quad (2.27)$$

(where  $k$  is the wave number and  $\omega$  is the frequency) gives the dispersion relation,

$$\omega^2 = C_s^2 k^2 - 4\pi G \rho_0 \quad (2.28)$$

and hence the growth rate of the density perturbation ( $\omega^{-1}$ ). Note that only for,  $C_s^2 k^2 - 4\pi G \rho_0 < 0$ , are the waves exponentially growing. This length scale defines the Jeans length, and underlines the classical Jeans instability.

To find the corresponding velocity perturbation, one inserts the density function into the

continuity equation (Eqn. 2.23). This gives

$$v' \propto -\frac{\omega}{\rho_0 k} \sin(kx) \quad (2.29)$$

The pressure perturbation is then specified using the ideal gas equation,

$$P \propto \frac{K_B T}{m_H} (\rho_0 + \rho') \quad (2.30)$$

To test the code, a 1D grid was seeded with these perturbations with an amplitude of  $\delta = 0.001$ , and evolved for 5 e-folding times (the time it takes the perturbation to increase by a factor of ‘e’) using periodic boundary conditions for both the box and the elliptic solver. The code was able to match the growth rate of the perturbation over the first couple of e-folding times ( $\tau_e$ ), to good accuracy (Fig. 2.2); by about  $t = 3\tau_e$ , the growth rate began to increase beyond the analytical curve, remaining within 10%, however, by the end of the simulation. These results confirm AstroBEAR’s ability to model self-gravity in astrophysical flows.

### 2.4.2 Modification: Bonnor-Ebert Sphere Module

Bonnor-Ebert (BE) spheres (Bonnor, 1956; Ebert, 1955) are finite, isothermal, self-gravitating spheres in hydrostatic equilibrium (i.e. solutions to the *Lane-Emden equation*). They are commonly used as initial conditions in simulations of single star formation, as will be demonstrated in Chapter 3. A module was added to AstroBEAR that initializes a BE sphere on the grid and perturbs it into collapse. Before describing the details of this module, let us first recall some of the basic properties of BE spheres.

All BE spheres have a flat-topped density profile near their centers, with outer densities that decline monotonically with radius (Fig. 2.3). The BE sphere, defined by its truncation radius  $R_{BE}$  and confining pressure  $P_{ext}(R_{BE})$ , is thermally or gravitationally dominated depending upon the value of its non-dimensional radius,  $\xi$ .  $\xi$  is related to the BE sphere’s initial central density  $\rho_0$ ,

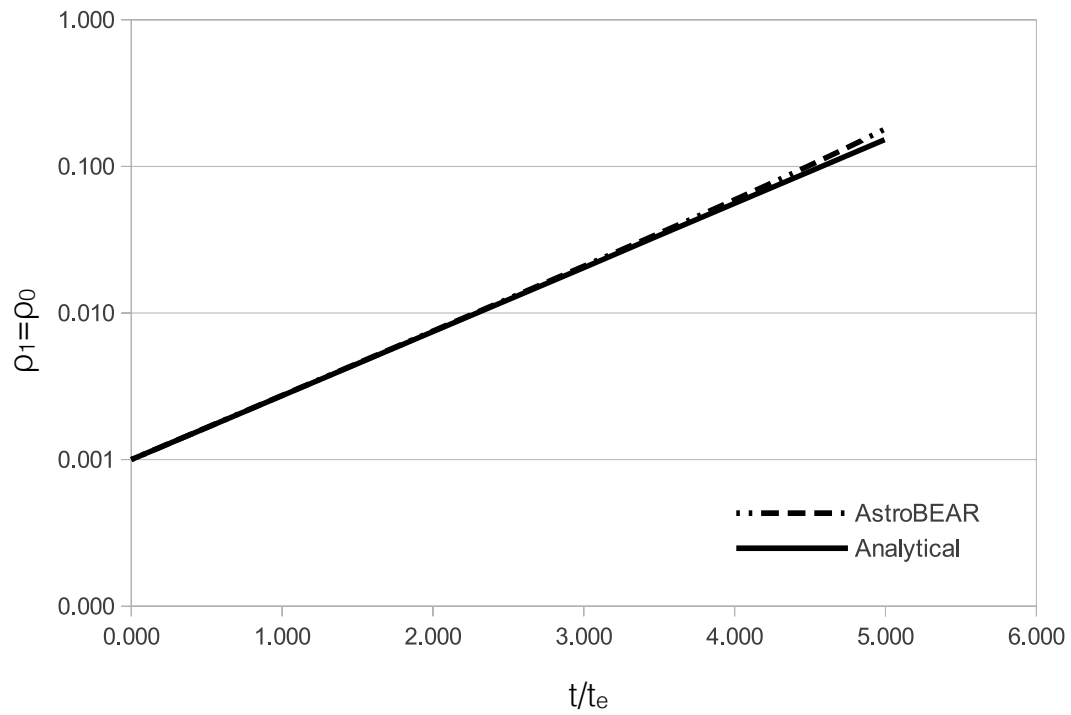


**Figure 2.2:** Growth rate of the Jeans instability for 1D flow. Comparison of AstroBEAR and the analytical prediction of the Jeans instability growth rate. Numerical data was taken from a peak in the growing instability, over time. AstroBEAR correctly produces the growth rate for the first few e-folding times  $t_e$ , diverging by about 10% by  $t=5t_e$ .

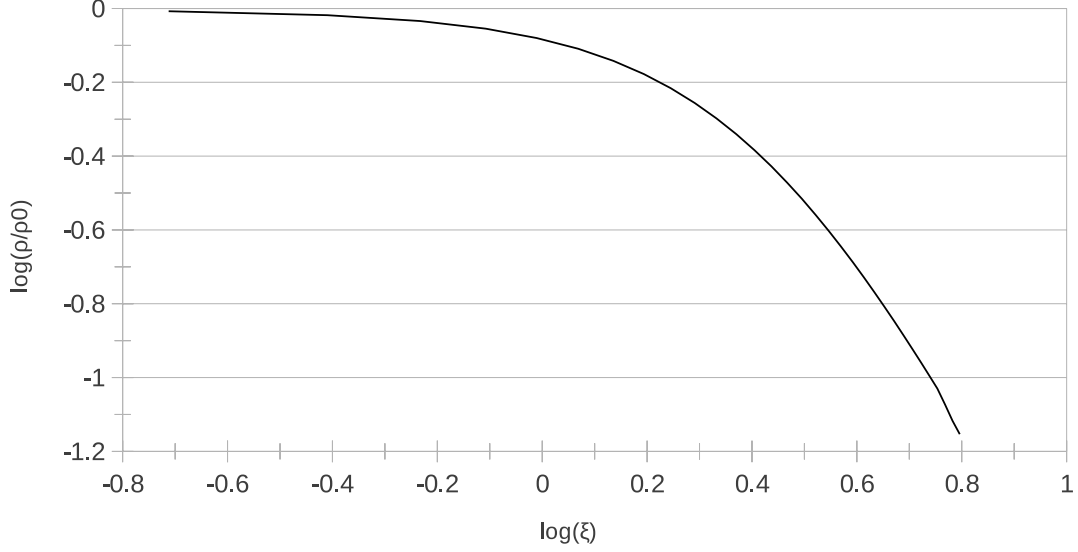


**Figure 2.3:** The density profile of a marginally-stable Bonnor-Ebert sphere as a function of  $\xi$  in log-log space. The y-axis is in scaled units, normalized to the initial central density  $\rho_0$  of the BE sphere. Given the scaled nature of this curve, it represents a family of solutions, each BE sphere given by a different  $\rho_0$  and truncation radius.

isothermal sound speed  $C_s$ , and truncation radius ( $R_{BE}$ ), through the equation:

$$\xi = \left( \frac{4\pi G \rho_0}{C_s^2} \right)^{1/2} R_{BE} \quad (2.31)$$

where  $G$  is the gravitational constant.

The sphere is marginally stable, i.e. on the cusp of its stability curve, when  $\xi \approx 6.5$ . At this point, with no added perturbation, the sphere may oscillate gently about its equilibrium profile. Likewise, collapse can proceed in this state with the application of small perturbations. The critical radius and external pressure of a marginally-stable BE sphere of mass  $M_{BE}$  are given by (Spitzer, 1968):

$$r_{crit} = 0.41 \frac{GM_{BE}}{C_s^2} \quad (2.32)$$

$$P_{crit} = 1.40 \frac{C_s^8}{G^3 M_{BE}^2} \quad (2.33)$$

The BE sphere module uses an approximate analytic solution of the Lane-Emden equation (Liu, 1996) to initialize the density profile of the BE sphere on the grid. For reference, the Lane-Emden equation is given by:

$$\frac{1}{\xi^2} \frac{d}{d\xi} \left( \xi^2 \frac{d\psi}{d\xi} \right) = e^{-\psi} \quad (2.34)$$

where  $\psi = \phi_g C_s^{-2}$ . The analytic approximation to the solution of this equation requires  $\xi$  and  $\rho_0$ , and returns the BE sphere's mass density profile  $\rho(r)$ . It is given by:

$$\omega = (1 + \alpha) \ln\left(1 + \frac{\xi^2}{6}\right) - \frac{\xi^2}{6} \frac{\alpha}{1 + \frac{\xi^2}{6}} - \alpha \ln\left(1 + \frac{\xi^2}{3^{1/\alpha} 12e}\right) + \ln\left[1 + (2^{-\alpha} - 1) \frac{D\xi^2}{1 + D\xi^2}\right] \quad (2.35)$$

where  $e^{-\omega} = \rho(r)\rho_0^{-1}$ , and  $\alpha$  and  $D$  are free parameters. By default, AstroBEAR uses  $\alpha = 0.551$  and  $D = 3.84 \times 10^{-4}$ , which reduces the relative error between the approximate solution and the Lane-Emden equation to 0.74% (Liu, 1996). Thus, the BE sphere module requires three user-defined input variables to be specified at run-time:  $\xi$  (XI),  $\rho_0$  (CENTRAL\_RHO), and  $R_{BE}$  (CLUMP\_RAD). These should be entered in CGS units (note, CENTRAL\_RHO should actually be entered as a number density for consistency with the problem module).

By default, the BE sphere is embedded within an ambient medium of the same pressure. The density of the ambient medium, however, can be specified at run time using the variable RHO\_WEIGHT, which is used to set the ambient density by dividing  $\rho(R_{BE})$  in the problem

module by this value. That is, if  $\text{RHO\_WEIGHT} = 4$ , then the density of the ambient medium will be a 1/4 of the density at the sphere's outer edge (i.e.  $\rho_{amb} = \rho(R_{BE})/4$ ). Given pressure equilibrium across the BE sphere/ambient boundary, if the density of the ambient medium differs from the sphere's outer edge, then the temperatures will be adjusted accordingly in the problem module. The magnetic field and velocity of the ambient medium is set to 0 by default for this problem module, but that can be changed at run-time using the ambient object's data file.

Lastly, the user can trigger collapse of the BE sphere by either uniformly reducing the thermal energy everywhere in the BE sphere, or by uniformly increasing the density within the BE sphere (by 10% for either method). These switches are hard-coded in the problem module, and can be turned on by uncommenting the desired switch there. By default, the BE sphere is non-rotating, and non-magnetized, although these settings can also be changed in the problem module by specifying these values in the clump object initialization subroutine.

## 2.5 Source Terms: Heating & Cooling

Heating and cooling was modeled using a parameterized cooling curve adapted from Inoue & Inutsuka (2008). This cooling function accounts for a variety of thermal processes relevant to the ISM, such as heating from X-rays and cosmic rays, and cooling due to molecular rotation/vibration and collisions. Additionally, it has been modified from its original form to include the effects of UV shielding by dust grains, which allows the gas to cool to  $T = 10 \text{ K}$  (as appropriate for protostellar cores).

The cooling function ( $\mathcal{L}$ ) enters the energy equation as a source term,

$$\frac{\partial e}{\partial t} + \nabla \cdot [\mathbf{v}(e + P)] = -\rho\mathcal{L} \quad (2.36)$$

and is operationally split from the hydrodynamic advance steps. Note,  $\mathcal{L}$  is the *net* cooling function, which accounts for both the heating and cooling rates per hydrogen nucleus ( $\Gamma$  and  $\Lambda$ , respectively) through the following parameterized equations:

$$\rho\mathcal{L} = n(-\Gamma + n\Lambda) \text{ erg cm}^{-3} \text{ s}^{-1} \quad (2.37)$$

$$\Gamma = 2 \times 10^{-26} \quad (2.38)$$

$$\frac{\Lambda}{\Gamma} = 1.0 \times 10^7 \exp\left(\frac{-118,400}{T + 1000}\right) + 1.4 \times 10^{-2} \sqrt{T} \exp\left(\frac{-22.75}{\max[1.0, T - 4]}\right) \quad (2.39)$$

where  $n$  is number density. For each density, a balance between heating and cooling is achieved at a certain pressure, determined by the equation  $\mathcal{L}(n, T) = 0$ . This equilibrium curve is plotted as a solid black line on top of a thermal pressure vs. density distribution in Figure 4.13. This figure also illustrates the typical thermal behavior of gas that is shocked, heated, and cooled, following an ISM cooling curve (notably, the generation of a thermally unstable regime between  $1 \lesssim n \lesssim 10 \text{ cm}^{-3}$ ).

## 2.6 Source Terms: Sink Particles

To model gravitationally-bound and collapsing objects beyond the resolution of the mesh, AstroBEAR uses a numerical sub-grid algorithm called sink particles. Before sink particles can form, a series of checks must be satisfied that ensure they form only where appropriate in the simulation. Following Federrath et al. (2010a), these checks are:

1. The grid must be on the finest AMR level
2. The cell in which a sink particle will form, and the surrounding spherical volume (of  $r_{\text{sink}} = 4\Delta x$ ), must be *bound*<sup>2</sup> and *Jeans unstable*<sup>3</sup>
3. The location of the potential sink must coincide with a local gravitational potential minima

---

<sup>2</sup>The sum of all energies within the volume must be negative.

<sup>3</sup>In terms of a critical mass, if the mass within a sphere ( $M$ ) exceeds the Jeans mass of the sphere ( $M_J$ ), i.e.  $M > M_J \equiv (4/3)\pi\rho\lambda_J^3$ , the sphere is too massive to be thermally supported against gravity. Such a sphere is *Jeans unstable*.

4. There must be a converging flow onto the location of the potential sink, within  $r_{\text{sink}}$
5. The location of the potential sink must not overlap with the radius of any other sink particles ( $r_{i,\text{sink}}$ )

Once formed, sink particles are able to accrete gas from the surrounding zones, but only when the density in the surrounding zones exceeds a given threshold, dictated by the Jeans condition (Truelove et al., 1997):

$$\lambda_J > 4\Delta x_{\min} \quad (2.40)$$

The Jeans condition prevents artificial fragmentation of the gas as would occur if the Jeans length were not sufficiently resolved. Additionally, it constrains accretion to occur only for gravitationally unstable gas which would otherwise collapse onto the sink particle if the gas were not restricted to the mesh. During the accretion step, only the *excess* gas (above the Jeans threshold) is removed from a given cell and accreted. Thus, depending on the size-scale of the simulation, sink particles may physically represent young stellar objects (as in Chapter 3), or entire protoclusters (as in Chapter 4).

In addition to accretion, sink particles interact with the gas (and other sink particles) gravitationally. However, they remain individual objects throughout the course of a simulation (i.e. do not merge), even if gravitational forces bring them close together. Sink particles have been modified in AstroBEAR to perform outflow and radiation feedback, which is described in the following section. While the thesis research does not include feedback, it will be used in future work as detailed in Chapter 6.2.2

### 2.6.1 Modification: Radiation Feedback from Sink Particles

Sink particles were modified to perform radiation feedback, using the flux-limited diffusion (FLD) radiative transfer solver in AstroBEAR (based on Krumholz et al., 2007). In the FLD limit, radiation

is produced in the grid as a result of thermal motions (i.e. black-body radiation,  $E_{\text{rad}} = aT^4$ ). Since sinks are a sub-grid model they are not assigned a temperature directly (the sub-grid model by definition does not track how big the forming star is that the sink represents, how fast it is growing by contraction, etc.). Thus, an estimate of the amount of radiation produced by the sink is needed, to be included as a source term in the radiation solver. To this end, the sink particle is envisioned as a protostar, i.e. not yet producing radiation through fusion, but through its accretion luminosity:

$$L_{\text{acc}} = \frac{G\dot{m}M_*}{R_*} \quad (2.41)$$

where  $\dot{m}$ ,  $M_*$ , and  $R_*$  are the protostellar accretion rate, mass, and radius, respectively.

The accretion energy produced from infall onto the particle each time-step is estimated using the RHS of Equation 2.41, as energy accretion onto sink particles is not explicitly calculated in AstroBEAR. More precisely, at each time-step  $i$ , the accretion energy is computed as:

$$E_{\text{acc},i} = \frac{GdmM_i}{R} \quad (2.42)$$

where  $G$  is the gravitational constant in computational units,  $dm$  is the total accreted mass for that time-step,  $M_i$  is the instantaneous mass of the sink particle at time-step  $i$ , and  $R$  is the radius of the protostar, taken to be 1 solar radius by default, but modifiable by the user at run-time. Once calculated, the accretion energy is distributed smoothly in a kernel surrounding the sink particle. From there, it diffuses away from the sink via FLD radiative transfer.

To ensure that the sum of the discretized accretion energy distributed over the kernel equals the total accretion energy calculated that time-step, we have the following equation:

$$\sum \Delta E_{\text{acc},i} * dV_i = E_{\text{acc},i} \quad (2.43)$$

where  $\Delta E_{\text{acc},i}$  is the differential amount of  $E_{\text{acc},i}$  to be distributed in the  $i$ th cell, and  $dV_i$  is the

volume of the  $i$ th cell. As written, the units do not balance in this equation (the RHS needs to be expressed as an energy *density*), and thus, a normalization constant  $k$  is needed with units of  $1/\text{volume}$ . This constant is given by a smoothing function for  $E_{\text{acc},i}$ , which is chosen to be a decaying exponential:

$$\Delta E_{\text{acc},i} = k E_{\text{acc},i} e^{-r_i/\sigma} \quad (2.44)$$

where  $\sigma$  is a scaling factor. In the code  $\sigma$  is chosen such that the smoothing function goes to zero at the boundary of the kernel over a range of 4 e-foldings. Inserting Equation 2.44 into Equation 2.43,

$$\sum k E_{\text{acc},i} e^{-r_i/\sigma} dV_i = E_{\text{acc},i} \quad (2.45)$$

yields the normalization constant:

$$k = \frac{1}{\sum e^{-r_i/\sigma} dV_i} \quad (2.46)$$

While the set of equations for the kernel is arbitrary, this normalization constant yields the necessary *specific* accretion energy (averaged over a radiative time-step), which is then passed into the radiation solver as a source term.

### 2.6.2 Modification: Outflow Feedback from Sink Particles

In addition to radiation feedback, sink particles were modified to perform outflow feedback. The outflow feedback module is based on Federrath et al. (2014), and models a two-component outflow: a fast, collimated, inner jet, embedded within a slow, wide-angle outflow. The injection kernel for the outflow is a cone, centered on the sink particle, with a radius of  $r_{\text{out}} = 16$  zones on the finest level. The opening angle of the outflow is set by the user at run-time, and defaults to  $\theta_{\text{out}} = \pi/6$ .

Within the outflow cone, the density and radial velocity to be injected are set according to

the following equations,

$$\rho_{\pm}(\mathbf{x}) = \alpha_{\pm}\rho(\mathbf{x}) \quad (2.47)$$

$$v_{\pm}(\mathbf{x}) = \alpha_{\pm}(a_{\pm}v_r(\mathbf{x}) + dv_{\perp,\pm} + b_{\pm}R_{\pm}v_{\Omega}) \quad (2.48)$$

where,  $\pm$  indicates the top and bottom outflow cones,  $\mathbf{x}$  gives the position vector from the sink particle to a given cell within the outflow cone, and  $\rho(\mathbf{x})$  and  $v_r(\mathbf{x})$  are the density and radial velocity profiles to be injected into the outflow cones, respectively. To ensure that the total momentum and mass injected into the top and bottom outflow cones are equal (and opposite in the case of the momentum), we have the following additional equations for constraining the system,

$$\sum \rho_{\pm} = f_m dM \quad (2.49)$$

$$\sum \mathbf{v}_+ = -\sum \mathbf{v}_- = \left(\frac{GM_*}{10R_{\odot}}\right)^{1/2} \hat{\mathbf{r}} \quad (2.50)$$

where  $f_m$  is the fraction of accreted material ( $dM$ ) to be injected back into the grid, and the injected velocity (the expression on the RHS of Eqn. 2.50) is the Keplerian velocity at the surface of a 10 solar radius protostar with mass given by the instantaneous sink particle mass ( $M_*$ ). Simultaneous solution of this system of equations (Eqn. 2.47-2.50) yields the scalar normalization constants  $\alpha$ ,  $a$ , and  $b$ . Then, the precise density and velocity to inject into each cell of the outflow cones is given by Equation 2.47 and 2.48, respectively.

To solve this system, the algorithm makes use of a shift operator normal to the spin axis,  $dv_{\perp}$ , and a rotation matrix,  $R$  (see Eqn. 2.47-2.48), to correct any differences imparted to the total momentum in the outflow cones after discretization and application of material into the kernel. To avoid sharp discontinuities at the boundaries of the kernel, the density profile is smoothed radially

and azimuthally according to:

$$\mathcal{R}(\mathbf{x}, r_{\text{out}}) = \begin{cases} \sin [\pi(x/r_{\text{out}})] & \text{for } x \leq r_{\text{out}} \\ 0 & \text{for } x > r_{\text{out}} \end{cases} \quad (2.51)$$

$$\Theta(\theta, \theta_{\text{out}}) = \begin{cases} \cos^p [(\pi/2)(\theta/\theta_{\text{out}})] & \text{for } \theta \leq \theta_{\text{out}} \\ 0 & \text{for } \theta > \theta_{\text{out}} \end{cases} \quad (2.52)$$

In addition to the radial smoothing of Eqn. 2.51, the velocity profile is smooth azimuthally according to:

$$\mathcal{V}(\theta, \theta_{\text{out}}) = \frac{1}{4}\Theta(\theta, \theta_{\text{out}}) + \frac{3}{4}\theta(\theta, \theta_{\text{out}}/6) \quad (2.53)$$

Equation 2.53 produces the characteristic two-component outflow of this feedback model.

The outflow algorithm begins with transforming the coordinates of the cell centers into the reference frame of the sink particle using the rotation matrix. The normalization factors  $\alpha_{\pm}$  are then trivially calculated by summing up the injected mass into each of the cones and setting this equal to the target value. Next, the outflow velocity is calculated for the top and bottom hemispheres using Equations 2.48 and 2.50, with the normalization constants set to 1,  $R$  to the identity matrix, and  $dv_{\perp} = 0$ . The normalization constants  $b_{\pm}$  are then adjusted, which is used for setting the magnitude of the outflow spin. To adjust the spin of the outflow,  $R$  is calculated for rotating the velocity vectors in the outflow frame along the jet axis, which is then applied to  $v_{\Omega}$ . Following rotation, the velocity vectors may need to be slightly adjusted so that they again adhere to the velocity constraint (Equation 2.50). To this end, the total momentum in both hemispheres is calculated and used to update the magnitude of the velocity component along the jet axis, using  $a_{\pm}$ . The remaining transverse components are then zeroed out using the shift operator  $dv_{\perp}$ . This sequence of steps is iterated until the momentum injection is balanced across the two hemispheres to machine precision.

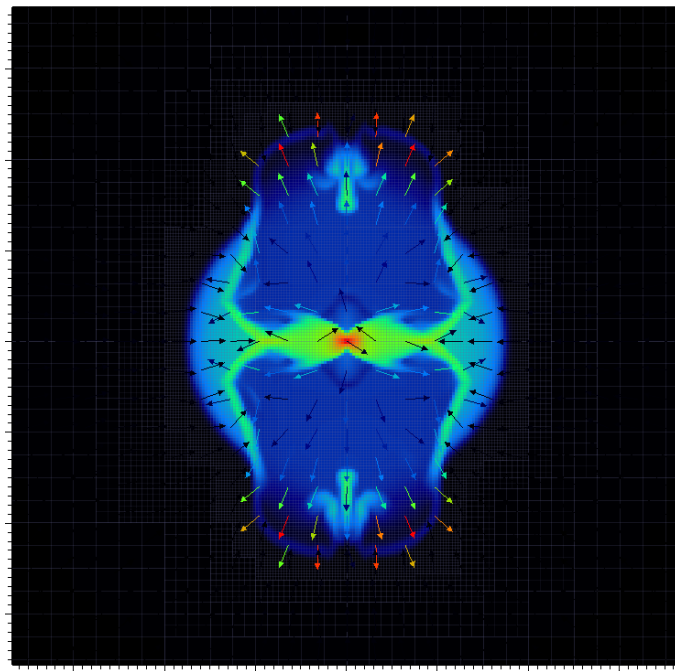


**Figure 2.4:** Density and velocity map of the newly incorporated outflow-feedback module in AstroBEAR. This image comes from initial exploratory simulations of a rotating, super-critical BE sphere, which collapsed to form a sink particle that is injecting mass and momentum back into the sphere following the outflow prescription of Federrath et al. (2014). Note that the sphere’s rotation axis (and thus, the spin axis of the sink particle which forms at its center) is oriented upward in this 2D slice through the mid-plane of the simulation.

A snapshot of the resultant outflow of this feedback module is shown in Figure 2.4 for a rotating, collapsing BE sphere that formed a sink particle at its center which is feeding back on its environment.

## Chapter 3

# The Effect of Environment on Single Star Collapse

### 3.1 Introduction

Bonnor-Ebert spheres (Section 2.4.2) have long been the favorite initial conditions for star formation simulations (Hunter, 1977; Foster, 1994; Banerjee et al., 2004). They are often constructed to be in pressure equilibrium with their ambient environments, making them effective ‘toy-models’ for investigations of protostellar collapse. Moreover, quasi-spherical clumps that appear to be in hydrostatic equilibrium (HSE) have been observed in the local interstellar medium. The classic example of such a prestellar core is the Bok globule, B68 (Alves et al., 2001).

In terms of theoretical studies, a particularly useful property of BE spheres is their stability criterion, which says that BE spheres with density contrasts between center and edge  $< 14.5$  (or, equivalently  $\xi < 6.5$ , Section 2.4.2) are *stable* to gravitational perturbations (Bonnor, 1956; Ebert, 1955). This simple stability criterion can be cast in terms of a critical mass ( $M_{BE}$ ), similar to the Jeans mass ( $M_J$ ) of uniform spheres (Jeans, 1929), but with a different leading coefficient (i.e.

$M_{BE} \approx 2M_J$ , for spheres of equal temperature and average density). Such a critical mass provides an easy interpretation of the relative importance of *thermal and gravitational* energies within the sphere: if this stability condition is violated (i.e.  $M > M_{BE}$ ), thermal pressure alone cannot support the sphere’s own internal gravity, and collapse is initiated (provided there are no other supportive forces in the sphere, such as a magnetic field).

While the hydrostatic profiles of isothermal spheres are easily derived analytically, formulating an analytical model of their dynamics is not trivial. As a result, there is an on-going debate about the true nature of the mechanisms involved in isolated star formation. Modern studies of the detailed dynamics of spherical, protostellar collapse include work by Larson and Penston (LP), who explored similarity solutions for the collapse of uniform density, isothermal spheres (Larson, 1969; Penston, 1969a). Later, Shu presented the “expansion wave” similarity solution for hydrostatic, singular ( $\rho \propto r^{-2}$ ), isothermal spheres (SIS) (Shu, 1977). The expansion wave solution dictates that the center of an infinitely-peaked SIS immediately collapses into a point mass. This results in an *inside-out* collapse: adjacent spherical shells collapse one after the next as the interior loss in pressure propagates outward via an expansion wave. Material from the surrounding collapsing envelope is then accreted by the central object at a constant accretion rate.

Shu and collaborators (Shu et al., 1987b; Shu & Adams, 1987) suggested this inside-out collapse would occur for *any* hydrostatic, isothermal, spherically-symmetric mass distribution, including BE spheres. They speculated that this would occur through quasi-static, subsonic adjustments as the mass relaxed toward a  $r^{-2}$  density profile characteristic of the SIS. Perturbations on the growing core would then irrevocably lead to inside-out collapse.

However, simulations of collapsing BE spheres revealed very different behavior than an outward-propagating rarefaction. Unlike the SIS, BE spheres have been shown to collapse from the *outside-in*: infall begins in the outer regions of gravitationally unstable BE spheres, and travels inward with time (Hunter, 1977; Foster & Chevalier, 1993; Foster, 1994; Banerjee et al., 2004; Anathpindika & Di Francesco, 2013). These motions result in the collapse of the interior ‘core’

of the BE sphere (the inner, uniform density portion of the BE sphere radial profile): over time, this core grows in density while shrinking in radial extent. Surrounding the collapsing core is an extended ‘envelope’, whose density approaches a  $r^{-2}$  profile. Eventually a collapsed object forms at the center of the BE sphere, and this object continues to grow in mass through the accretion of the surrounding, infalling envelope. In contrast to the expansion wave model of the SIS, the accretion rate onto this object is variable (Foster & Chevalier, 1993).

The complexity of dynamics shown in simulations has made it challenging to reconcile the collapse of BE spheres with the early similarity solutions. In Whitworth & Summers (1985) (from here on referred to as WS), a general set of similarity solutions for the isothermal sphere were derived, with the Shu and LP solutions appearing at varying limits. The WS solutions describe collapse of isothermal spheres as either being triggered, or enhanced by, an externally driven, inward propagating compression wave, depending upon the degree of initial stability of the sphere. At early times, the sphere is either in a static equilibrium state or condensing because it is initially far out of equilibrium (such would be the case for the uniform density sphere). The compression wave-front represents a region of enhanced density that propagates into the sphere from the ambient environment, and its strength depends on the magnitude of the external pressure at the sphere’s surface. Once the compression wave converges on the center, an accreting YSO forms.

Several authors have since studied BE collapse dynamics within the WS compression wave framework. For instance, Hennebelle et al. (2003) explored the effect of varying the magnitude and duration of external pressure increases on the surface of marginally-stable BE spheres. In each case studied, a compression wave was triggered at the surface of the sphere that propagated inward with time, converged on the center of the sphere, and triggered the formation of a numerical YSO. Moreover, the amplitude of each generated compression wave was found to depend upon the magnitude of the applied external pressure gradient, consistent with the WS model. In Anathpindika & Di Francesco (2013), externally-driven compression waves were found to either amplify condensation of BE spheres and lead to their collapse, or to generate stable oscillations, depending upon the initial

gravitational stability of a given sphere.

Despite the great deal of attention paid to BE spheres, numerical studies of their basic collapse properties have largely assumed highly artificial initial conditions: the great majority of work places BE spheres within extremely low-density ambient environments (sometimes orders of magnitude lower in density than the sphere itself), and collapse is triggered through some applied perturbation (such as a decrease in thermal energy within the sphere). This setup fundamentally ignores the interaction between the ambient environment and the sphere, which has been shown to be of importance (Whitworth & Summers, 1985; Hennebelle et al., 2003; Myers, P. C., 2008; Anathpindika & Di Francesco, 2013).

As a continuation of the work aimed at exploring the *interaction* between protostellar cores and their environments, a series of simulations was carried in which marginally-stable BE spheres were embedded within simple, uniform background environments of different masses. Instead of forcing the embedded sphere into collapse through some applied perturbation, the *system* (BE sphere + ambient environment) was allowed to evolve *dynamically*. That is, the evolution of the BE sphere was driven by the gravito-hydrodynamical interaction between the sphere and its environment.

## 3.2 Methods

### 3.2.1 Numerical Model

As AstroBEAR is not currently configured in spherical coordinates, the problem domain was a cube of side length  $L$ , with the marginally-stable ( $\xi = 6.5$ ) BE sphere located at the center. The fluid variables were initialized following Banerjee et al. (2004), henceforth BPH04, to check the fidelity of AstroBEAR’s results. Those authors chose parameters to match potential sites of massive star formation. Thus, the BE sphere was initialized to have an initial radius of  $R_{BE} = 1.62 \text{ pc}$ , central number density  $n_0 = 2004 \text{ cm}^{-3}$ , temperature  $T = 20 \text{ K}$ , mass  $M_{BE} = 151 M_{\odot}$ , and isothermal sound speed  $C_s = 0.4 \text{ km s}^{-1}$ . In addition, the sphere was set to be in pressure equilibrium with

its ambient environment. This means that for those cases with a density mismatch between the sphere’s outer edge and the ambient medium (i.e.  $\rho(R_{BE}) \neq \rho_{amb}$ ), there was also a temperature mismatch. Regardless of the initial radial temperature profile of the simulations, however, the simulations evolved isothermally. This was achieved using an ideal equation of state with a ratio of specific heats very close to 1 ( $\gamma = 1.0001$ ), but not exactly 1, to avoid infinities in the routine. This effectively gave the gas a nearly infinite heat capacity, which allowed the gas to maintain a nearly constant temperature when compressed. The gas was assumed to be monatomic ( $\mu = 1$ ).

As stated above, the BE sphere was placed at the origin of a spherically symmetric mass distribution inside of the simulation box. The boundaries of this simulation box were much larger than the radius of the BE sphere ( $L = 30 R_{BE}$ ), mitigating any potential boundary effects. Note, this setup models the special case of a protostellar core (the BE sphere) that is located at the center of mass position of an encompassing, concentric molecular cloud. If the parent cloud is gravitationally unstable, its collapse path will be toward the center of the box, coinciding with the position of the BE sphere. This implies a maximally disruptive system – collapse of the parent cloud will maximally disrupt the BE sphere. Thus, this setup represents an idealization of the process under study.

Given the symmetry of the problem, only the first octant of the domain was actually simulated. That is, the mesh extended from 0 to 25 pc in the  $x$ ,  $y$ , and  $z$  directions (Fig. 3.1). Boundary conditions on the outward-facing sides of the box were extrapolating. To prevent gas from leaving the box, the velocity was set to 0 along those faces. Boundary conditions were reflecting on those faces that intersected the BE sphere.

The resolution of the coarse grid was  $16^3$  cells. At the start of the simulation, five levels of AMR were initialized in the simulations, with the finest level fully encompassing the sphere and the remaining grids nested outward from there (c.f. Fig. 3.1). Thus, the BE sphere began with a finest cell size of  $\Delta x_{min} = 0.05$  pc and roughly 34 cells/ $R_{BE}$ . Additional resolution was added over the course of the simulation where needed, based on two refinement criteria. First, gradients in the fluid variables would initiate the addition of up to 5 levels of AMR. This resolution criterion was

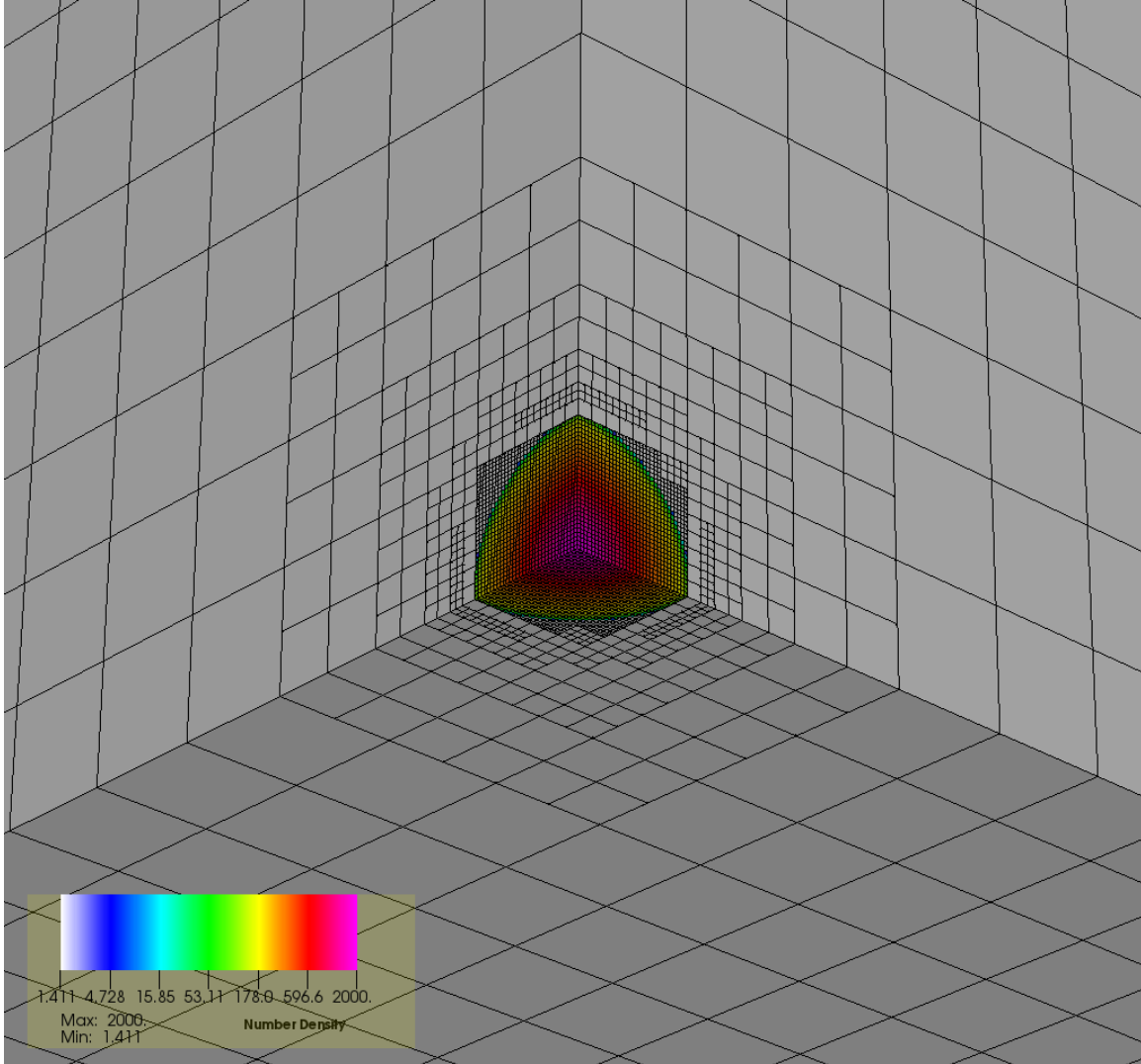


**Figure 3.1:** Schematic of the mesh with an octant of the Bonnor-Ebert sphere located at  $(0,0,0)$ . While all simulations were initialized with 5 levels of refinement to achieve  $\sim 34$  cells per initial clump radius, only the first 3 levels are plotted here for clarity. The mesh was dynamic in that additional levels of refinement were added as needed (see text). The color-bar shows variation in  $n$  ( $\text{cm}^{-3}$ ). Note that the maximum value in this plot is lower than the reported  $2004 \text{ cm}^{-3}$ , given the data from the finest cells are not plotted.

mainly used to track dynamics in the ambient medium. Second, two additional levels of refinement were possible (for a maximum of 7 AMR levels) if/when the following condition was violated in the simulations:

$$\lambda_J > 4\Delta x \quad (3.1)$$

This refinement criterion, known as the “Jeans Condition”, enforces adequate resolution of the local Jeans length ( $\lambda_J = (\pi C_s^2 / G\rho)^{1/2}$ ), so as to avoid unphysical fragmentation of the gas (Truelove et al., 1997).

Once the maximum resolution was achieved, sink particles (c.f. Section 2.6) could form in those regions where the gas continued to collapse. Recall that once formed, sink particles are able to accrete gas from the surrounding zones, but only if those zones themselves are gravitationally unstable, and then, only the excess gas is removed and accreted. In this way, sink particles represent a numerical approximation to YSOs, at least on the size scale of the present suite of simulations (in larger-scale simulations, they might represent entire clusters of newly forming stars, c.f. Chapter 4).

### 3.2.2 Simulation Parameters

A set of nine simulations were performed, as listed in Table 3.1. The density of the ambient environment (and hence, its total mass) varied between the simulations, from  $\rho_{amb} = .01\rho(R_{BE})$  to  $\rho_{amb} = \rho(R_{BE})$ . Each of the simulations were allowed to evolve dynamically (i.e. without the application of a perturbation to initiate the sphere’s collapse), with the exception of one run. In this case, the perturbation was a 10% density enhancement to all zones within the sphere. Because this is the common form of perturbation in BE collapse studies, as well as the common initialization of the BE sphere (in an ambient medium that is a factor of 100 lower in density), we named this case the ‘Classic’ case.

Run	$\rho_{amb}/\rho(R_{BE})$	Perturbation?
Sparse	1/100	No
Classic	1/100	YES
Matched	1	No
1/3	1/3	No
1/10	1/10	No
1/30	1/30	No
1/40	1/40	No
1/45	1/45	No
1/50	1/50	No

**Table 3.1:** Suite of simulations. The first column gives the name of the run, the second gives the initial density contrast between the ambient medium and the edge of the sphere, and the third states whether a perturbation was applied to initiate collapse.

### 3.3 Results

#### 3.3.1 A Test of Stability: The Sparse Ambient Medium Case

To begin, let us consider the case of a BE sphere embedded in a hot ( $T = 2000K$ ), low density ( $n = 1.4 \text{ cm}^{-3}$ ) ambient medium, and allowed to evolve for  $t_{sim} = 19 \text{ Myr}$  (or five sound crossing times,  $t_{sc} = C_s R_{BE}$ , of the sphere). This is the above described ‘Classic’ case, *without* a perturbation. As evident from the radial density profiles in Figure 3.2, this configuration of the BE sphere + ambient medium is dynamically stable. Over the course of the simulation, the sphere can be seen to gently oscillate about its initial equilibrium profile. A look at the corresponding radial velocity profiles confirms this (Fig. 3.3): fluid motions remained subsonic over the course of the simulation, evidenced by interior sound waves that traveled between the sphere’s edge and center as it gently relaxed on the grid.

That the sphere remained stable over 5 crossing times, with no indication of either runaway collapse or expansion (the largest radial excursion in the sphere’s radius represented only  $\sim .1R_{BE}$ ),

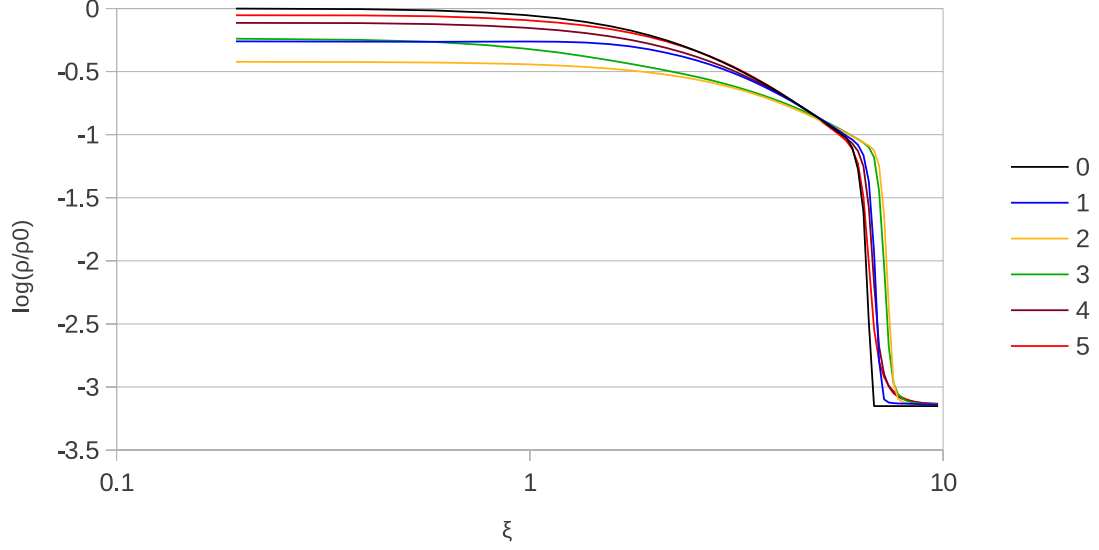


**Figure 3.2:** Radial density profiles for the Sparse case. The different profiles are calculated at different sound crossing times of the sphere,  $t_{sc}$ . The sphere’s outer boundary is traced by the discontinuous jump in density that occurs at the BE sphere/ambient border. Note, the data for this, and all subsequent radial profiles in this chapter, have been averaged over concentric, spherical shells to minimize any noise induced by the non-spherical mesh.

confirms AstroBEAR’s ability to recover appropriate, analytical solutions for self-gravitating fluids. Moreover, these results are consistent with previous findings that the marginally-stable BE sphere requires at least minor perturbations to initiate gravitational collapse (Foster & Chevalier, 1993; Banerjee et al., 2004).

### 3.3.2 Outside-in Collapse of BE Spheres: The “Classic” Case

As a second test of AstroBEAR’s self-gravity solver, the problem setup of BPH04 was replicated and compared with AstroBEAR’s results. Namely, a 10% density enhancement was applied to all

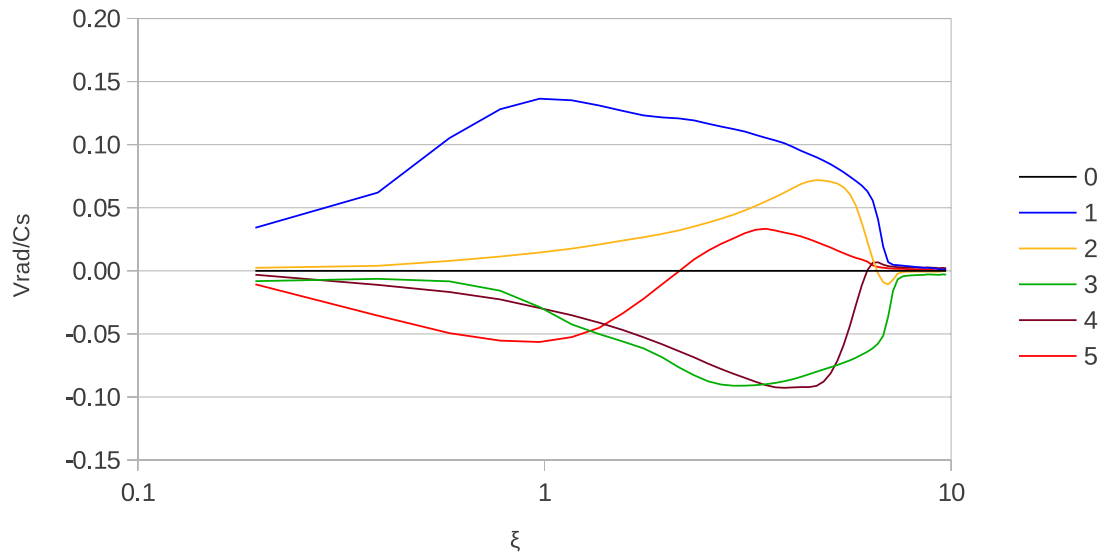


**Figure 3.3:** Radial velocity profiles for the Sparse case. Again, the different curves represent different times in the simulation, in units of the sphere’s sound crossing time,  $t_{sc}$ . Small subsonic radial motions (sound waves) are visible throughout the sphere over the course of the simulation. Negative velocities indicate radial infall.

interior zones of the BE sphere in the Sparse case (as detailed in Section 3.2.1). The effect was to increase the mass within the sphere above that which could be supported by thermal pressure alone, as dictated by the Lane-Emden equation ( $E_{th} < E_g$ ).

In agreement with BPH04 and others, the result of this perturbation was outside-in collapse, marked by an increase in density of the flat-topped, inner core as it shrank in radius (Fig. 3.4). Flanking this collapsing core was an extended envelope with a nearly  $r^{-2}$  density profile. From the radial velocity profiles, infall can be seen to start in the outer regions of the sphere, and move inward with time (Fig. 3.5). By  $t/t_{sc} = 0.82$ , a sink particle was created and the peak inward radial velocity had become marginally supersonic ( $v_{rad} \approx 2.2 C_s$ ), consistent with previous studies of BE sphere collapse (Banerjee et al., 2004; Foster & Chevalier, 1993; Hunter, 1977).

Finally, note that the peak density within the sphere at the moment of sink particle formation is a function of resolution (recall,  $\Delta x \propto \lambda_J \propto \rho^{-1/2}$ , c.f. Section 3.2.1). Thus, this density is the same between the different runs ( $n_{final} = 1.9 \times 10^6 \text{ cm}^{-3}$ ). Moreover, that this density is lower than the density at which the gas would become optically thick ( $n = 10^7 \text{ cm}^{-3}$ , Banerjee et al., 2004), supports the isothermal treatment of the gas.

### 3.3.3 Varying the Ambient Density: New Collapse Modes

Having established the code’s ability to recover both hydrostatic solutions and previously explored BE collapse dynamics when triggered by an arbitrary density perturbation, we now turn to the results for collapse under more self-consistent conditions. In these simulations, the Classic model setup of the previous section was adjusted in two ways. First, the density profile across the BE sphere/ambient boundary was matched (while maintaining pressure equilibrium). Second, the simulation was allowed to progress without added perturbations. Following this ‘Matched’ case, the unperturbed evolution of 3 intermediate ambient density cases, log-spaced between the Sparse and Matched cases, are presented.

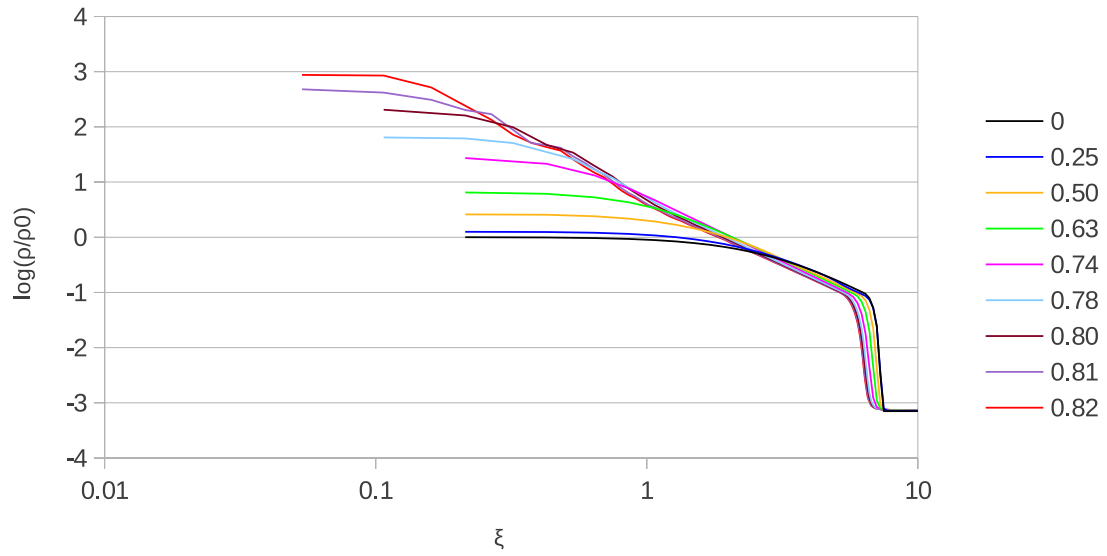


**Figure 3.4:** Radial density profiles for the Classic case, over time. Time is in units of the sphere’s sound-crossing time,  $t_{sc}$ . As shown, outside-in collapse is marked by a flat, inner collapsing core, trailed by a  $r^{-2}$  envelope. A sink particle forms in the center of the sphere by the last time state plotted in this and all remaining figures in this chapter.

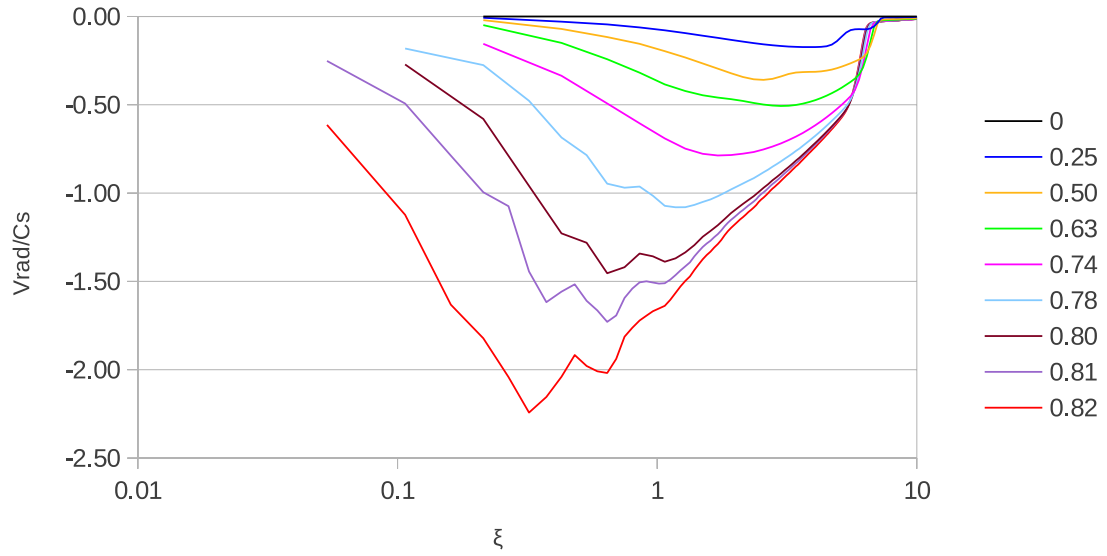


**Figure 3.5:** Radial velocity profiles for the Classic case, over time. Outside-in collapse is marked by an inward radial flow that begins at larger radii, and moves inward with time. The peak velocity in this run becomes marginally supersonic, approaching  $\sim 2.2 C_s$ , as expected (see text).

Run	$t_{ff}$ (Myr)	$t_{sim}$ (Myr)	$t_{sc}$ (Myr)
Classic	41.5	3.3	6.1
Matched	4.4	3.7	57.5
1/3	7.8	4.9	33.1
1/10	13.8	7	19.2
1/30	24.4	12.2	10.5

**Table 3.2:** Thermal and gravitational timescales for the ambient medium, along with the simulation times for the different runs. The free-fall time ( $t_{ff}$ ) is calculated using Eqn. 3.2 and the initial ambient density. Note, this is a rough approximation, as this equation assumes a spherical mass distribution and ignores the embedded BE sphere. The ambient sound crossing time ( $t_{sc}$ ) is calculated using the ‘radius’ of the ambient environment (i.e.  $r = L/2 = 25 \text{ pc}$ ), and its initial isothermal sound speed  $C_s$ .

### 3.3.3.1 Matched Ambient Medium

When the density in the ambient medium is equal to the density at the BE sphere’s outer radius, we see qualitatively different behavior leading to collapse. As can be seen in the density plot (Fig. 3.6), the Matched collapse mode is marked by an initial infall of material from the ambient medium onto the BE sphere. This is to be expected for two reasons. First, the sphere represents a gravitating source for the ambient material. Second, the higher density ambient material leads to a shorter collapse time based on its own self gravity. That is, because this run’s ambient medium has the greatest density, it also has the shortest free-fall time ( $t_{ff}$ ),

$$t_{ff} \approx \frac{1}{4} \left( \frac{3\pi}{2G\rho} \right)^{1/2} \quad (3.2)$$

Since this time scale is on the order of the simulation time ( $t_{sim}$ ), and is much less than the corresponding ambient medium sound crossing time (see Table 3.2), it is clear that the ambient medium experiences its own homologous collapse. This can be seen in the continual increase in density of material on the sphere’s outer surface.

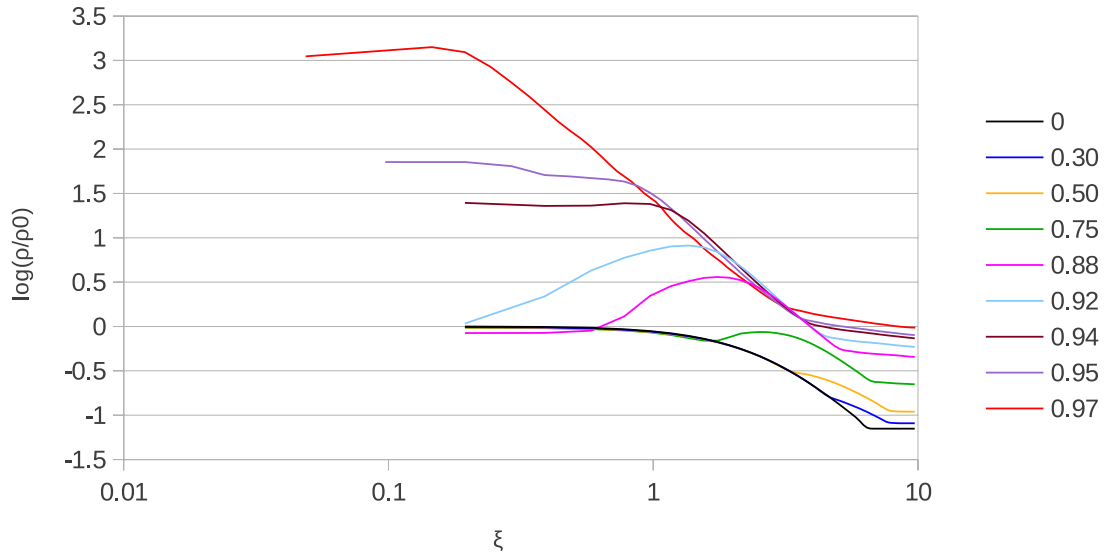


**Figure 3.6:** Density profiles for the Matched run,  $\rho(R_{BE}) = \rho_{amb}$ , over time. As shown, infalling material from the ambient medium builds up on the surface of the BE sphere. The ram pressure from this infalling material triggers a compression wave that propagates into the interior of the BE sphere, thereby triggering collapse. Interestingly, by  $t/t_{sc}=0.94$ , the Classic collapse profiles are recovered.

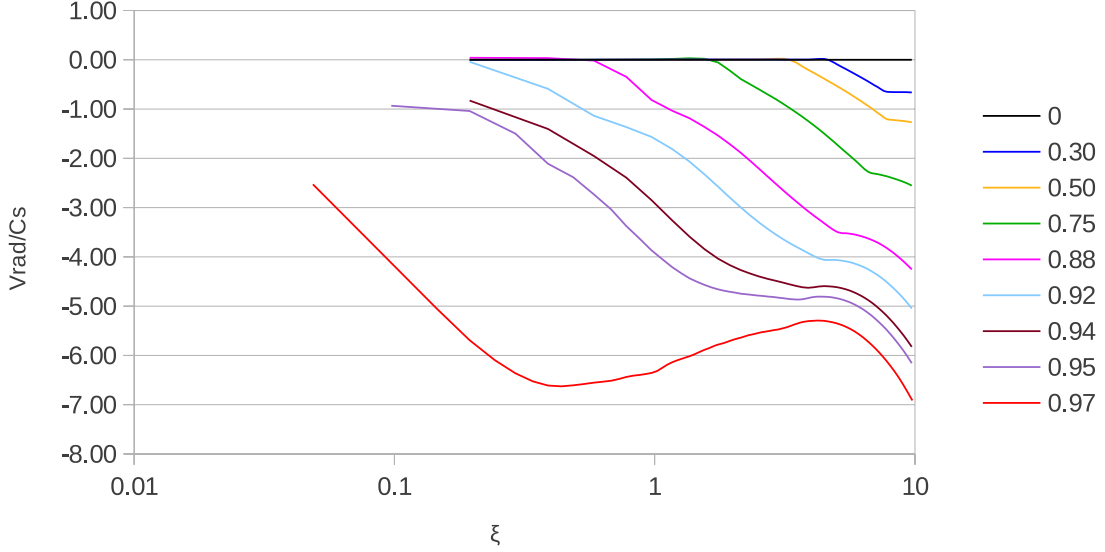


**Figure 3.7:** Radial velocity profiles for the Matched run,  $\rho(R_{BE}) = \rho_{amb}$ , over time. As in the density plot, late times indicate that the radial velocity profiles assume their classic shape, within  $\xi \approx 3$  by  $t/t_{sc} = 0.94$ .

The evolution in the Matched case is, therefore, dominated in the early stages by the infall of the ambient medium. In Figure 3.7, we see negative velocities (infall) develop in the ambient gas as soon as the simulation is initiated. Material initially builds up on the surface of the BE sphere, and it is both the gravitational force of this material and its inward directed ram pressure that eventually overwhelms the sphere's hydrostatic equilibrium and drives it into collapse. The explicit agent initiating collapse in this case is an inward directed compression wave induced at the BE sphere surface from the infall of the ambient environment.

Examining the profiles at  $t = 0.3 t_{sc}$  shows that this raining down of ambient gas onto the BE sphere has increased the density at its outer edge. In particular, the inflection point of the density profile, representing the transition from the BE sphere to the ambient environment, has

increased from  $r = 1.62 \text{ pc}$  to  $\approx 2 \text{ pc}$  (or,  $\xi = 6.5$  to  $\approx 8$ ). This represents a shell of new material that has been added to the BE sphere, which acoustic waves must attempt to redistribute. By  $t = 0.75 t_{sc}$ , the outer radius of the BE sphere has returned to its initial value and a strong peak in the density profile at  $r \approx 0.6 \text{ pc}$  ( $\xi \approx 2.5$ ) is now apparent. This feature marks the inward traveling compression wave. Note that as ambient material falls inward from larger radii, the density at the BE sphere boundary increases, as would be expected for the collapse of a homologous sphere. Thus, the BE sphere finds itself being crushed. Consideration of the ambient flow on larger scales (not shown) confirms it takes the form of a homologous collapse.

By  $t = 0.88 t_{sc}$ , the compression wave within the sphere has altered what remained of the original BE density profile. By  $t = 0.94 t_{sc}$ , the dynamics *switches to that seen in the Classic model*: the inner flat core increases in density and shrinks in radial extent, while the outer regions form an infalling envelope whose density profile does not change. A sink particle eventually forms in the inner most cell of the simulation by  $t = 0.97 t_{sc}$  (14% longer than in the Classic case).

Consideration of the radial velocity profiles also demonstrates the change from the compression wave phase to the later classic, outside-in collapse phase. During the compression wave phase ( $t/t_{sc} = 0 - 0.88$ ), inward directed fluid motions originate in the ambient gas. This negative velocity region moves inward with time, with its position corresponding to the location of the compression wave front. By about  $0.5 t_{sc}$ , the flow becomes supersonic.

For most of the early evolution, the highest velocities are seen in the infalling ambient gas. By  $t/t_{sc} = 0.94$ , however, a collapsing core within the BE sphere is established. By the time of sink formation, the peak velocity inside of the sphere corresponds with the edge of the core, as in the Classic case. In contrast, however, this flow has a peak mach number of  $M \approx 7$ , compared to the  $M \approx 2.2$  in the Classic case.

Thus, collapse was triggered in the Matched case by the dynamics of the ambient gas alone (i.e. without an applied perturbation). To explore the limits of this ambient triggering, we now turn to simulations with intermediate ambient densities, between the Matched and Sparse cases.

### 3.3.3.2 Intermediate Run 1/3

Evolution of the BE sphere in the densest of our intermediate runs ( $\rho_{amb} = \rho(R_{BE})/3$ ) proceeds similarly to the Matched case, but on different timescales. Consideration of the density plots in Figure 3.8 shows an initial accumulation of ambient material on the BE sphere/ambient boundary (which can be tracked by the discontinuity at this edge). By  $t/t_{sc} = 0.75$ , the BE sphere decreased in radial extent as well as increased in density at its outer edge (via a subsonic adjustment, evident in the corresponding radial velocity profile, Fig. 3.9). As material continued to rain down on the BE sphere, its outer radius decreased and mass accumulated in its outer regions ( $t/t_{sc} = 0.98$ ). The coeval velocity profiles show the flow to be subsonic up to and including this time. Thus, we see what appears to be a subsonic compression wave propagating inward from the (shrinking) outer radius of the BE sphere.

Unable to incorporate the new ambient material into an approximate hydrostatic equilibrium distribution, the sphere is unable to support itself against gravitational collapse. Thus, we see collapse proceeding by  $t/t_{sc} = 1.13$ . As in the Matched case above, the collapse resembles the Classic BE collapse profiles in this later phase of evolution ( $t/t_{sc} = 1.13 - 1.26$ ). As can be seen in the density plots, elements of the Classic collapse, such as a shrinking inner flat core trailed by an  $\sim r^{-2}$  density envelope, are associated with what appears to be a smaller and denser counterpart to the original BE sphere. The velocity profiles in this phase of evolution also approach the outside-in profiles within this ‘modified’ BE sphere ( $\xi < 4$ ).

Compared to the Matched case, there are some important points to note. First, the relative times for each phase of the evolution are different. For the Matched case, the compression phase corresponds to the early equilibration and subsequent compression wave propagation. This is the dominant phase of the Matched Case evolution, taking up a larger fraction of the total simulation time. In other words, the simulation switched to the Classic phase later in time in the Matched case than in Run 1/3. This occurred because of the stronger perturbation afforded by the ambient

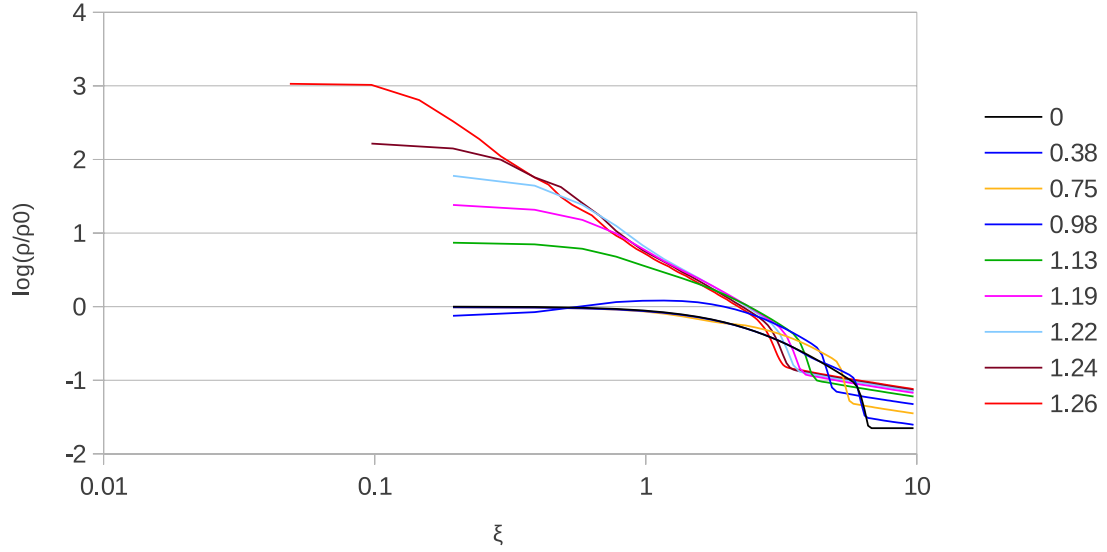


**Figure 3.8:** Density profiles for Run 1/3, over time. The legend is time in units of the sphere’s sound-crossing time,  $t/t_{sc}$ . Visible in this plot is a weak density wave traveling through the BE sphere after the ambient material sufficiently collects at the BE sphere surface ( $t/t_{sc} = 0 - 0.98$ ). The BE sphere was squeezed into a smaller radius with higher density, driving gravitational instability that results in collapse. The classic outside-in collapse dynamics are achieved, as evident by the shrinking flat core region and extended  $r^{-2}$  envelope ( $t/t_{sc} = 1.13 - 1.26$ ).

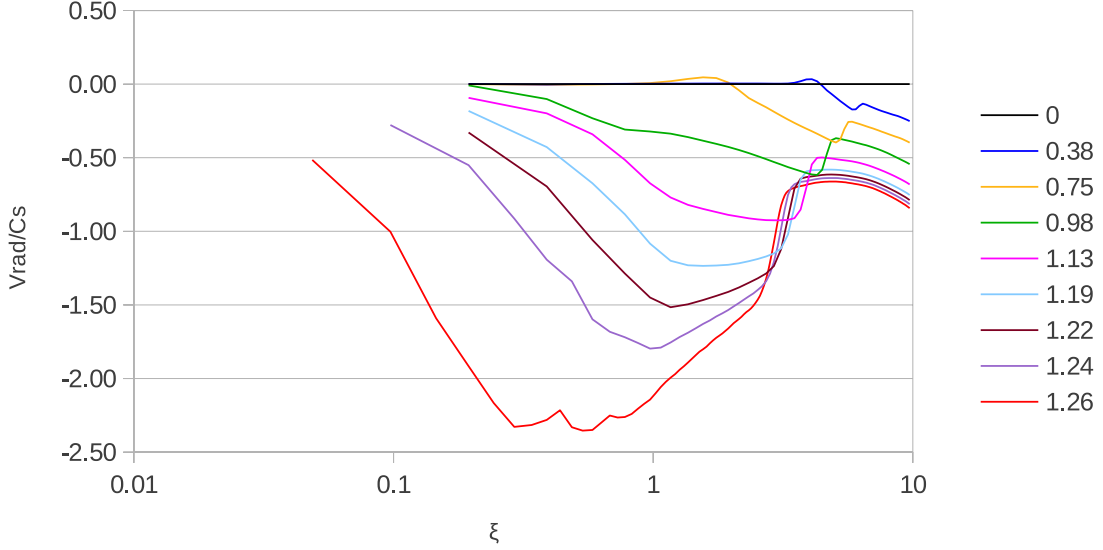


**Figure 3.9:** Radial velocity profiles for Run 1/3, over time. The flow is shown to slowly become marginally supersonic as it approaches the classic results inside a truncated region of the initial BE sphere.

material in the Matched case. Second, the slower flow in Run 1/3 (only marginally supersonic) led to a longer collapse time (i.e. the time until sink particle formation) of  $t_{\text{sink}}/t_{\text{sc}} = 1.26$  compared to the Matched case's  $t_{\text{sink}}/t_{\text{sc}} = 0.97$ .

Lastly, it is interesting to note that Run 1/3 was comparable to the Classic collapse in a number of ways. If we assign the beginning of the ‘Classic collapse phase’ for Run 1/3 to be  $t/t_{\text{sc}} = 1.19$ , we see an associated  $\log(\rho/\rho_0) \approx 1.2$  and  $v_{\text{rad}}/C_s \approx -1.25$ . Looking at the same part of the evolution in the Classic case (now corresponding to  $t/t_{\text{sc}} = 0.78$ ), we see that  $\log(\rho/\rho_0) \approx 1.8$  and  $v_{\text{rad}}/C_s \approx -1.1$ . By the end of the simulation, the peak velocities are nearly the same,  $v_{\text{rad}}/C_s \approx -2.25$ , although again the simulation evolved over longer time scales for this intermediate case compared to the Classic model. *Thus, once the perturbation provided by the ambient gas was*

established, the flow followed the classic outside-in evolution.

### 3.3.3.3 Intermediate Run 1/10

In the sparser ambient medium of Run 1/10 ( $\rho_{amb} = \rho(R_{BE})/10$ ), the evolution and collapse of the BE sphere proceeded differently than in the Matched and 1/3 runs. In the density plot of Figure 3.10, we see less accumulation of material on the outer surface of the BE sphere at  $t/t_{sc} = 0.55$ . The increase in density there contributed to a *slight* gravitational contraction that reduced the BE sphere radius ( $t/t_{sc} = 1.10$ ). Further accumulation of falling ambient material onto the BE sphere after this time was negligible, yet the sphere continued to contract. As the inner regions grew in density ( $t/t_{sc} = 1.42$ ), the sphere eventually began to collapse under its own self-gravity, once its critical mass had been exceeded. The collapse then proceeded classically until sink particle formation at  $t_{sink}/t_{sc} = 1.83$ .

Consideration of the corresponding velocity profiles in Figure 3.11 shows a subsonic adjustment of the BE sphere to material accumulating on its surface ( $t/t_{sc} = 0.55$ ). By  $t/t_{sc} = 1.42$ , outside-in collapse is clearly underway, reaching a peak velocity close to the Classic result of  $v_{rad}/C_s \approx -2.5$  by sink particle formation, as in Run 1/3.

### 3.3.3.4 Intermediate Run 1/30

Unlike the compression wave collapse cases, but similar to the 1/10 case, the BE sphere enters a breathing mode over the first sound crossing time, as evident by the outward motions of the  $t/t_{sc} = 0.95$  radial velocity curve in Figure 3.12. During this oscillation, we see the interior density decrease (for  $\xi < 4$ ), without a concomitant decrease in the BE sphere radius (location of the kink in density, Fig. 3.13), indicating the breathing mode initially vacates mass from the inner regions of the BE sphere. This mass is small relative to the mass of the sphere (recall,  $M_{BE} \approx 150M_\odot$ ), only about  $0.4 M_\odot$ . The sphere attempts to redistribute its interior mass into a rough HSE, through local pressure gradients. This re-equilibration, however, leaves the the BE sphere in the unstable

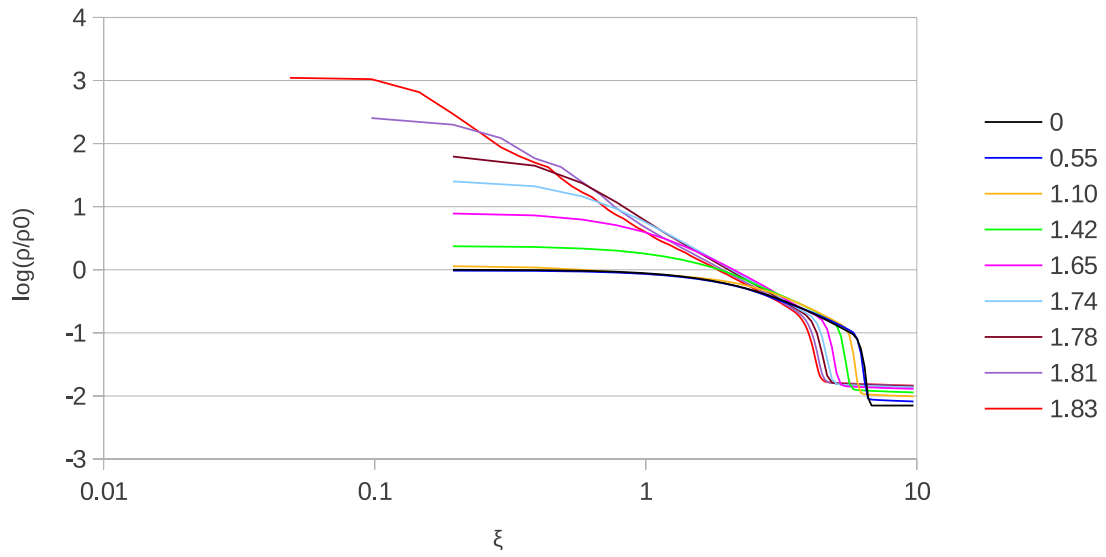


**Figure 3.10:** Density profiles for Run 1/10,  $\rho_{amb} = \rho(R_{BE})/10$ , over time. The legend is time in units of the sphere's sound-crossing time,  $t/t_{sc}$ . A light rain of ambient material can be seen to accumulate on the BE sphere surface at ( $t/t_{sc} = 0.55$ ). Amassed material squeezes the BE sphere into a smaller radial volume ( $t/t_{sc} = 1.10 - 1.42$ ), eventually triggering classic, outside-in collapse for ( $t/t_{sc} = 1.65 - 1.83$ ).

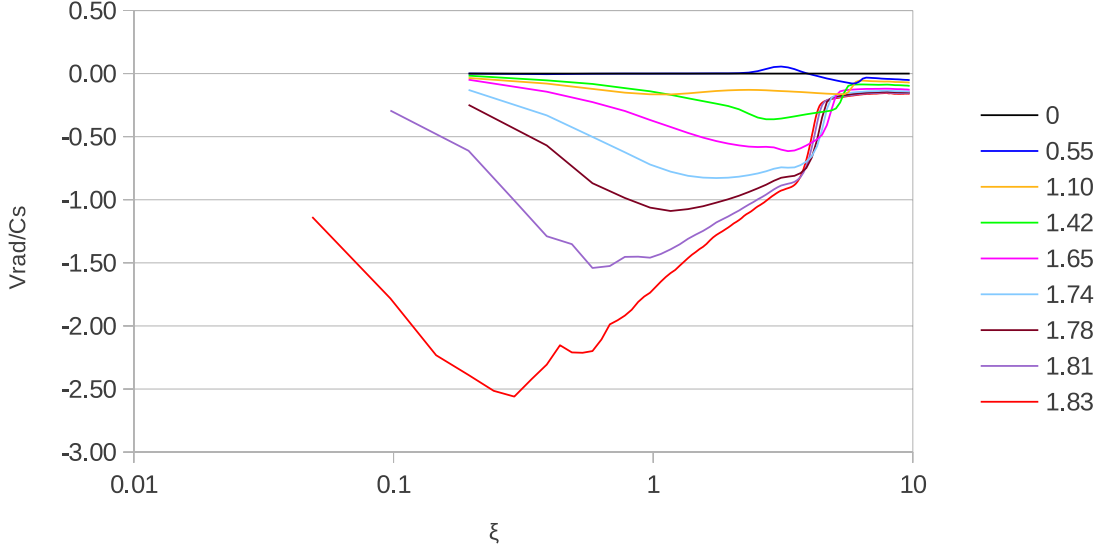


**Figure 3.11:** Radial velocity profiles for Run 1/10,  $\rho_{amb} = \rho(R_{BE})/10$ , over time. For times ( $t/t_{sc} = 0.55$ ), small subsonic adjustments to the ambient flow is visible within the sphere. Classic outside-in velocity profiles are recovered by ( $t/t_{sc} = 1.65$ ).

regime of its equilibrium curve, with its non-dimensional radius  $\xi > \xi_{crit}$  (Fig. 3.14). In this state, even small perturbations induced by numerical noise are sufficient to trigger the collapse of the re-configured sphere. Indeed, for  $t > 2.46$ , classic outside-in collapse ensues, with inflows becoming supersonic by  $t/t_{sc} = 2.85$ .

### 3.4 Discussion

The above presented results support that the collapse of BE spheres strongly depends on the nature of their encompassing medium. For those ambient environments with densities large enough to collapse on time scales comparable to the embedded BE sphere, strong compression waves can be

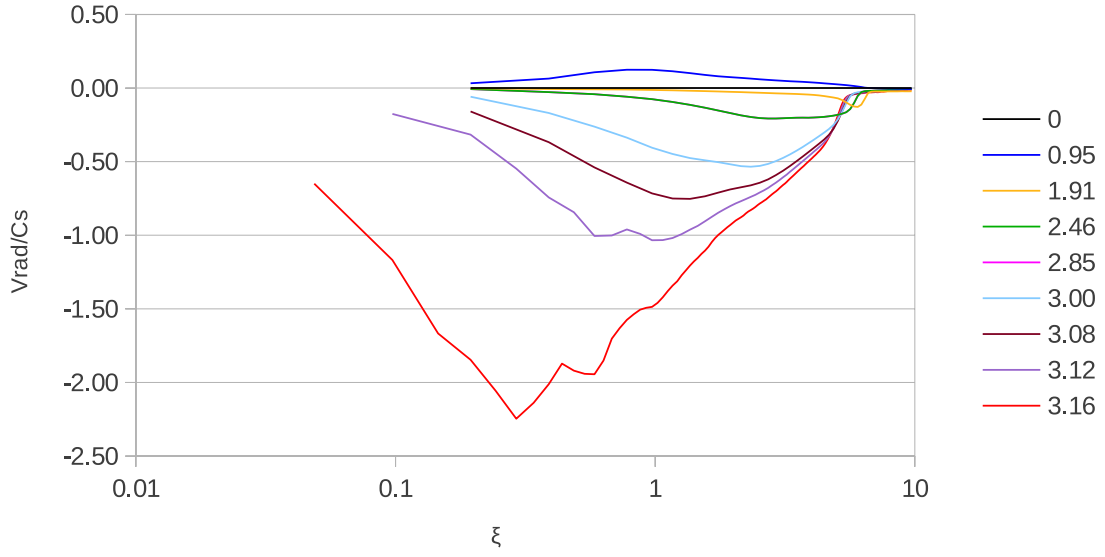


**Figure 3.12:** Radial velocity profiles for Run 1/30,  $\rho_{\text{amb}} = \rho(R_{BE})/30$ , over time. The sphere gently adjusts to its initialization as visible by interior sound waves for times  $t/t_{sc} = 0 - 2.46$ . By  $t/t_{sc} = 2.86$ , gravitational instability has set in and classic, outside-in collapse is underway. Collapse concludes with sink particle formation at  $t_{\text{sink}}/t_{sc} = 3.16$ .

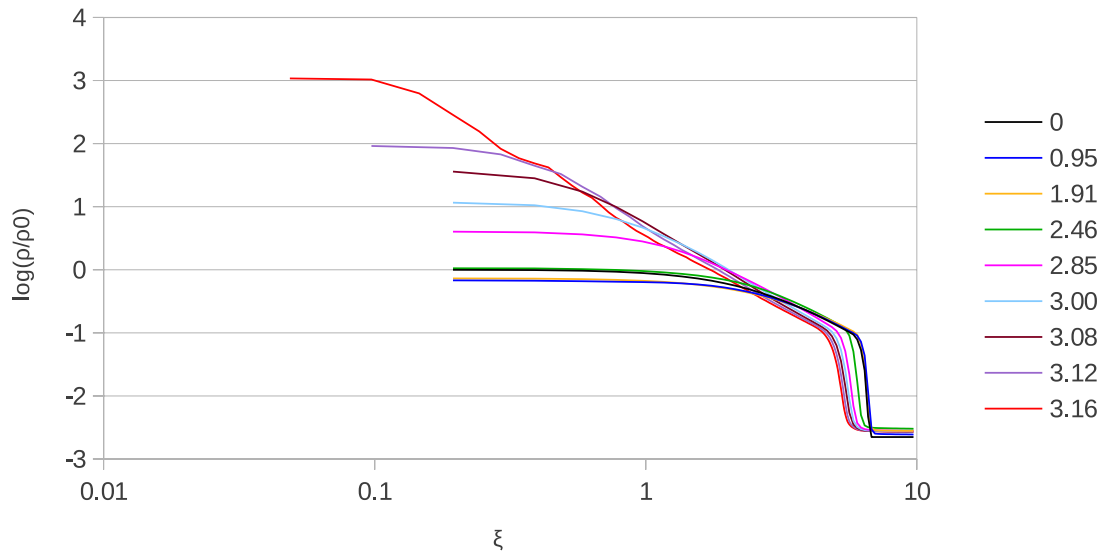


**Figure 3.13:** Density profiles for Run 1/30,  $\rho_{amb} = \rho(R_{BE})/30$ , over time. The legend is time in units of the sphere's sound-crossing time,  $t/t_{sc}$ . As can be seen in this plot, the BE sphere enters a breathing mode for time states  $t/t_{sc} = 0 - 2.46$ , where the interior density rises and falls. By  $t/t_{sc} = 2.86$ , gravitational instability has set in and classic, outside-in collapse is underway. Collapse concludes with sink particle formation at  $t_{sink}/t_{sc} = 3.16$ .

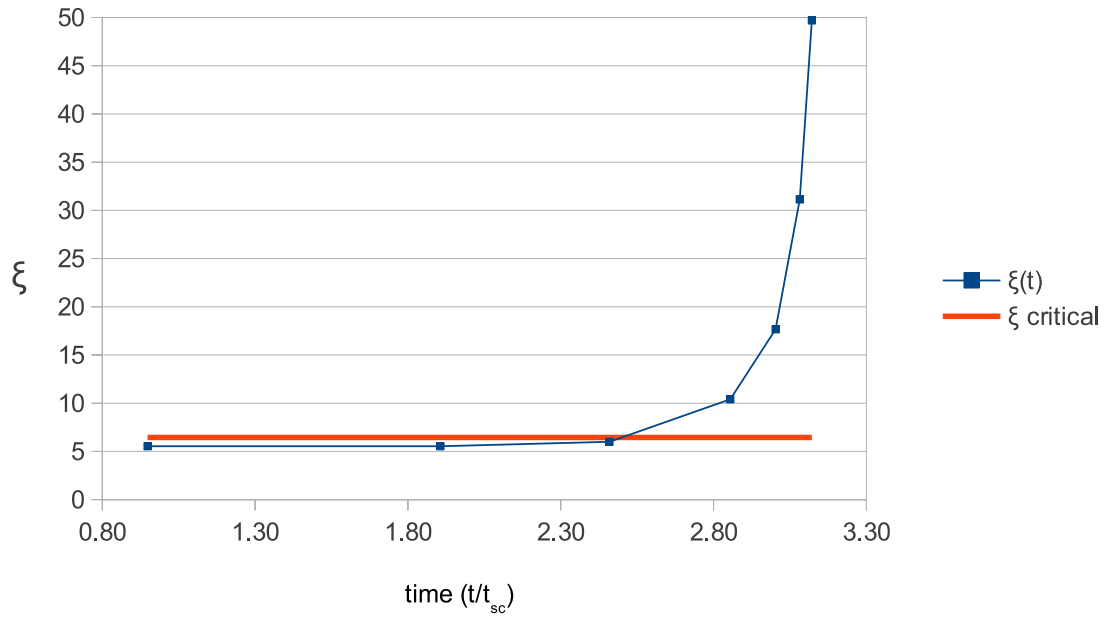


**Figure 3.14:** Variation of the non-dimensional radius ( $\xi$ , Eqn. 2.31) with time for Run 1/30.  $\xi$  is calculated for each time shown in Figure 3.13, with  $\rho_0$  and  $r$  being those instantaneous values of the central density and radius of the BE sphere for that time state. Since  $\rho_0$  and  $r$  change over the course of the simulation (c.f. Fig. 3.13), we see a change in  $\xi$  that takes the BE sphere from the sub-critical to super-critical regime by  $t/t_{sc} = 2.85$ .

induced on the surface of the sphere, mediating its own collapse. For densities low enough, the direct role of the ambient medium is diminished, and instead a slow increase in pressure at the sphere's edge (as well as an accumulation of ambient mass) can be the trigger of collapse. Depending upon the density of the ambient medium, early periods of the collapse follow one of two discrete modes discussed below. By late times, however, the collapse assumes the classic outside-in profiles, *in all cases*.

The first mode is a compression wave induced collapse, which was most strongly present in the Matched case. To understand this, consider that for a sufficiently large ambient medium, the collapse time of the ambient medium can be approximated by the free-fall time ( $t_{ff}$ ) of a uniform sphere (Eqn. 3.2). For the Matched ambient medium, this time is on the order of the BE sphere's sound crossing time ( $t_{ff}/t_{sc} \approx 4.3 \text{ Myr}/3.5 \text{ Myr} \approx 1$ ), indicating that the time needed for the sphere to adjust thermally via sound waves to gravitational instability induced at its boundary is comparable to the collapse time of the ambient gas. In addition, a sufficiently dense ambient medium (i.e. the Matched case) will be Jeans unstable. That is, the sound crossing time of the ambient medium is much greater than its freefall time ( $t_{sc,amb}/t_{ff} \approx 130$ , for the Matched case). If the ambient medium is gravitationally unstable on time scales comparable to the evolution of the BE sphere, we can expect strongly driven inward motions onto the BE sphere to drive compression and eventual collapse of the sphere.

In the second mode of collapse, the trigger of gravitational instability is the slow *accumulation* of infalling ambient material. This mode of collapse occurred in Runs 1/10 and 1/30. In these cases, the sphere was slowly compressed, ultimately changing configuration from marginally-stable to unstable. This was confirmed by computing the non-dimensional radius  $\xi$  of the evolving BE sphere in Run 1/30. As the ambient gas exerted both increasing thermal and ram pressure on the BE sphere,  $\xi$  was driven above the critical value of  $\xi = 6.5$  (Fig. 3.14), thereby forcing the sphere into collapse.

If the density contrast between the marginally-stable BE sphere and the ambient medium is

high enough, the embedded sphere will not collapse. As evident from the Sparse run, the embedded sphere will instead remain dynamically stable over many sound crossing times. Thus, there exists a critical value of the ambient density, defining a turnover between too heavy to sustain the BE sphere, and too light to induce collapse. To explore this critical value, additional simulations were performed between  $\eta = 30$  and 100, where  $\eta$  is the density contrast between the sphere's edge and ambient medium. Within 5 sound crossing times (the same final simulation time of the Sparse run), the  $\eta = 45$  was found to collapse, but the  $\eta = 50$  case did not. Running the  $\eta = 50$  case out longer showed it does eventually collapse. Together, these results indicate that the turn-over in the stability of the system occurs due to slow gravitational settling of the ambient material onto the BE sphere. Within some time range, the amount of material that has fallen onto the sphere may or may not be sufficient to induce collapse.

To derive an approximate critical value of the turn-over between stable and unstable configurations, let us consider the ambient gas as a slowly settling atmosphere responding to the gravity of the BE sphere. Imagine at  $t = 0$  the ambient medium begins to fall in toward the surface of the BE sphere. The material that reaches the surface is heated by compression, and then expands to create an atmosphere in hydrostatic equilibrium of scale height  $h$ . For an isothermal, plane parallel atmosphere, the scale height is given by,

$$h = \frac{K_B T}{m_H g} \quad (3.3)$$

where  $K_B$  is the Boltzmann constant,  $T$  is the temperature,  $m_H$  is the atomic mass unit, and  $g$  is the gravitational acceleration. Assuming  $g$  is constant, we can approximate  $g$  as,

$$g = \frac{GM_{BE}}{R_{BE}^2} \quad (3.4)$$

where  $M_{BE}$  and  $R_{BE}$  are the initial mass and radius of the BE sphere, respectively. This atmosphere induces an increased pressure on the surface of the BE sphere, which grows with time as the amount

of mass that has fallen into the atmosphere increases. The pressure at the surface ( $P_{atm}$ ) can then be approximated as,

$$P_{atm}(t) = F/A = \frac{GM_{BE}M_{atm}(t)}{4\pi R_{BE}^2(R_{BE} + h)^2} \quad (3.5)$$

To get an approximation for the mass of the atmosphere,  $M_{atm}(t)$ , we consider the collection of mass parcels that have had enough time to reach the BE sphere via freefall. Considering each parcel of gas in the ambient medium to only be gravitationally attracted by the BE sphere, the freefall time for each parcel is approximately,

$$t_{ff} = \frac{\pi}{2} \frac{(r)^{3/2}}{\sqrt{2GM_{BE}}} \quad (3.6)$$

Inverting this equation for the freefall radius gives,

$$r_{ff} = \left( \frac{2\sqrt{2GM_{BE}}}{\pi} t \right)^{2/3} \quad (3.7)$$

The mass within this freefall radius is then given by,

$$M_{atm}(t) = \frac{4}{3} \pi r_{ff}^3 \rho_{amb} \quad (3.8)$$

where we take the ambient density  $\rho_{amb}$  to be its initial value. Combining this with the pressure expression above yields,

$$P_{atm}(t) = \frac{8}{3\pi^2} \left( \frac{GM_{BE}}{R_{BE}} \right)^2 \frac{\rho_{amb}}{(R_{BE} + h)^2} t^2 \quad (3.9)$$

This expression can be used to calculate the pressure perturbation induced by atmospheric settling at the BE sphere surface over time. Since the turn-over occurs in the limit of a Jeans stable ambient environment, let us consider only those cases where the Jeans length of the ambient environment is

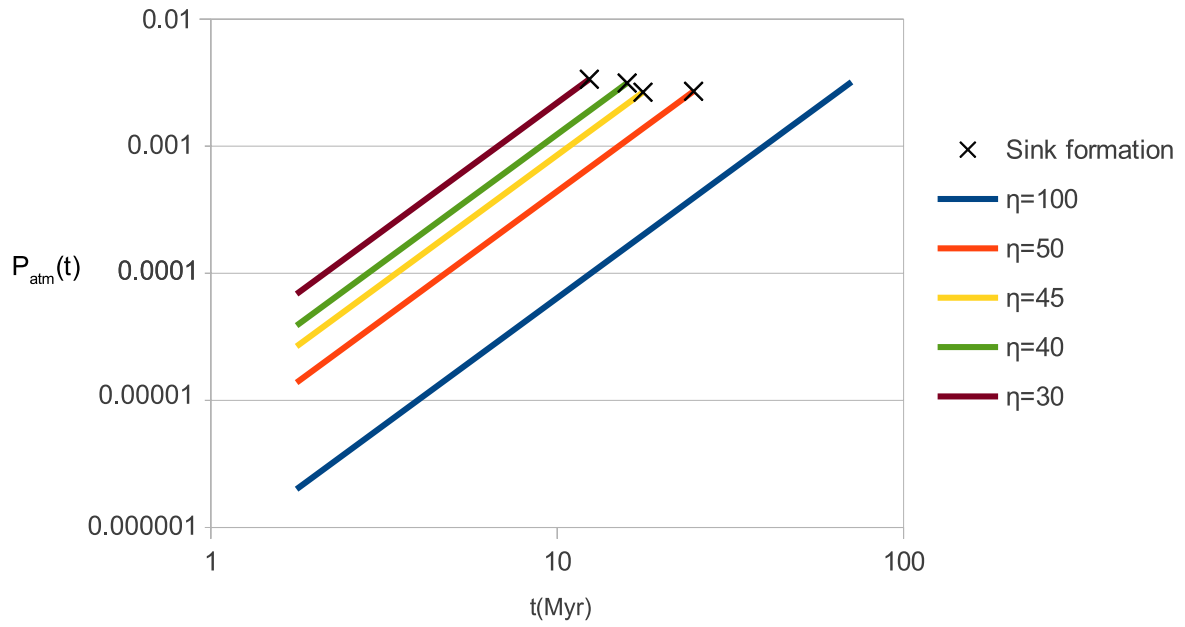
larger than the box size.

Figure 3.15 shows that this atmospheric settling model accurately predicts the threshold value of the pressure perturbation, as indicated by the nearly equal magnitude of the perturbation at sink particle formation in the different simulations. The model also predicts that as the ambient density is decreased ( $\eta$  increased), the time it takes to reach this threshold grows. This allows a prediction of when collapse might be triggered by calculating when the pressure perturbation meets this critical value. Thus, this simple model appears to capture the threshold in  $\eta$  for which configurations should collapse. The model would break down obviously when the scale-height exceeds the box size, as is the case for  $\eta = 100$ , which remained dynamically stable beyond the time predicted.

It should again be emphasized that the work presented here was an idealization of the system studied. This is because of the placement of the BE sphere at the center of mass position of a concentric, spherically symmetric ambient environment. This assumption is convenient, but it is of course a special case that makes the environment in the Matched case “maximally crushing”. If the BE sphere’s position did not coincide with the center of mass, or if it were embedded in a cylindrical filament instead of a sphere, the evolution might be more representative, and less dominated by global infall. However, the connection between our simulations and the astrophysical environment can still be drawn. The Matched case bears a resemblance to the cores described by Teixeira et al. (2005) in the Lupus complex, where dense cores within the star-forming Lupus 3 molecular cloud have a gradual decrease in density moving outward from the core center. In contrast, the mismatched cases are more like static gas with a phase change from core to environment, such as cold, dense neutral globules embedded in hot, rarefied, ionized HII regions.

## 3.5 Conclusions

The focus of this chapter was on the role of the ambient medium in triggering the collapse of marginally-stable Bonner-Ebert spheres. First, it was confirmed that AstroBEAR could reproduce



**Figure 3.15:** Pressure perturbation induced at the surface of the sphere as a function of time, as derived from the atmospheric settling model. The y-axis is given in scaled units, where  $P_{atm}(ba) = P_{atm}(t) \cdot \text{Pscale}$ , and  $\text{Pscale} = 2.77e - 13 \text{ ba}$ . For the cases  $\eta = 30 - 50$ , there is a threshold value of this perturbation that is reached by sink particle formation. The  $\eta = 100$  case did not form a sink particle by the time this perturbation pressure should have been reached, but for this case the approximation would be expected to break down (see text).

both long-lived stable BE spheres, as well as recover previously measured outside-in collapse modes driven by an arbitrarily imposed perturbation. Next, the results of a series of simulations of increasing density contrast between the BE sphere and encompassing ambient medium were presented. For the Matched case,  $\eta = \rho(R_{BE})/\rho_{amb} = 1$ , the ambient medium was itself Jeans unstable. Its infall drove a strong compression wave that triggered the classic outside-in collapse of the BE sphere. This compression wave-triggered collapse mode held for density contrasts up to  $\eta = 10$ . In contrast, for  $\eta > 10$ , a form of gravitational settling led to increased pressure on the BE sphere surface. The higher pressure forced the sphere to adjust such that it eventually switched from being marginally-stable to unstable, and then followed an outside-in collapse. For low enough ambient densities (for a given computational box size), BE spheres remained dynamically stable for the duration of the simulations.

Given there is a cut-off to the induced dynamical instability when the ambient density becomes low enough, these results indicate that BE sphere type solutions for isolated starless cores/clumps require high values of the density contrast to be long-lived. Lower density contrasts imply the cores will not be stable structures. Instead, they will most likely be part of a larger region undergoing collapse. Given the rapid crushing of the BE spheres by the infall of highly Jeans unstable environments, only high  $\eta$  solutions may be models for long-lived cores (with properties like a BE sphere).

While a distinction between the different triggers of collapse was found, there was little difference in the late phase of evolution (i.e. after collapse had been initiated). The systems that went unstable *always* eventually followed outside-in dynamics, which included the formation of a collapsing flat-topped core surrounded by a  $r^{-2}$  envelope and supersonic radial inflow tracking the core/envelope boundary. Thus, the well known features of BE sphere collapse are robust, once collapse is initiated. Furthermore, these results provide support for the WS framework in matching the predicted roles of compression waves with the collapse of embedded BE spheres.

In conclusion, this work emphasizes the likely unitary nature of star forming environments,

---

such that separations between core and inter-core medium may be largely a matter of definition only. For the above presented simulations, it appears that unless cores are formed with very large density contrasts relative to their surroundings, the ambient gas will play an important and ongoing role in the core's dynamics. This is consistent with previous models that attempt to consider continuous distributions of variables between embedded cores and their environments (such as, Myers, 2008).

## Chapter 4

# Molecular Cloud Formation in High-shear, Magnetized Colliding Flows

### 4.1 Introduction

The interstellar medium is a dynamic environment where material cycles from a warm, tenuous phase to a cold, dense phase and back again. The evolution of the gas through these phases establishes limits on star formation in the galaxy. Understanding the details of such dynamics is crucial as theoretical scenarios for molecular cloud evolution (and hence star formation) have shifted away from models based on long molecular cloud lifetimes (i.e. steady states where  $\tau_{cloud} \gg \tau_{ff}$ ; cf. Shu et al., 1987; Mouschovias, 1991). Over the last decade or more, evidence has grown that instead supports a scenario in which clouds are *transient* structures born out of the cold, dense phase of the ISM. For example, starless clouds appear to be scarce, meaning clouds do not slowly evolve towards conditions in which star formation begins (Beichman et al., 1986; Dame et al., 2001). Also, the

majority of stars in clouds are, in general, young showing ages  $< 5 \text{ Myr}$  (Hartmann et al., 2001a). This implies that star formation begins soon after the cloud itself forms and that clouds are not generally long-lived due to the absence of older stars (Fukui & Yonekura, 1998; Palla & Stahler, 2000; Carpenter, 2000). Finally, high degrees of hierarchical structure in molecular clouds should have short lifetimes due to star-star scattering or tidal interactions (Lada & Lada, 1995; Eisenhauer et al., 1998; Beck et al., 1998). While observational support for short cloud lifetimes has grown steadily, we note that scenarios invoking rapid cloud and star formation are not new (Hunter, 1979; Larson, R. B., 1981; Hunter et al., 1986; Ballesteros-Paredes et al., 1999). Given the complexity that comes with a dynamical theory of molecular cloud evolution, however, exploring the full dynamics of these scenarios depends heavily on high performance computational methods.

One scenario that generates transient molecular clouds and whose exploration has been possible with modern numerical simulations is the ‘colliding-flows’ model of molecular cloud formation. In this model, molecular clouds are formed in the shocked collision layer between two large-scale colliding streams of gas. Simulations of colliding flows have shown that nonlinear density structures readily form in the shocked collision region between the flows via a variety of instabilities (cf. Heitsch et al., 2005 for a discussion of the unstable modes). Further, these structures develop column densities high enough for effective UV-shielding, and thus,  $H_2$  formation ( $N \approx 1 - 2 \text{ cm}^{-2}$ ; van Dishoeck & Black, 1988; van Dishoeck & Blake, 1998). Gravitational instabilities then cause the turbulent, shocked gas in the dense structures to collapse and form stars. Given the highly dynamical environment, the transition from the beginning of molecular cloud formation to star formation to cloud destruction occurs in roughly a dynamical time (Audit & Hennebelle, 2005; Heitsch et al., 2006; Vázquez-Semadeni et al., 2006; Heitsch et al., 2008), matching observations (Elmegreen, 2000; Ballesteros-Paredes & Hartmann, 2007, and references therein). The clouds produced in colliding flows simulations are similar in many ways to those seen in observation.

While colliding-flows models tend to be idealized, they are not without motivation. Coherent large-scale streams of gas are plausible in many situations in the ISM, such as, expanding bubbles

driven from energetic OB associations and/or supernovae, turbulent motions arising from gravitational instabilities, density waves in the spiral arms of galaxies, and cloud-cloud collisions (Hartmann et al., 2001b; Inutsuka et al., 2015). Observational evidence supporting these various scenarios, as well as their association with molecular cloud formation, takes a number of forms. Atomic inflows surrounding molecular gas have been observed in Taurus (Ballesteros-Paredes et al., 1999) and other molecular clouds (Brunt, 2003). Looney et al. (2006) show that the active star forming molecular cloud core in BD +40 4124 likely arose from cloud-cloud collisions (a localized version of a colliding flow). Molecular clouds have been found at the edges of supershells (Dawson et al., 2011, 2013), which are a form of colliding flows driven by multiple supernovae.

If molecular clouds form via the accumulation of gas on dynamical time scales (Hartmann et al., 2001a), then magnetic fields are expected to be dynamically important on similar time scales. Some colliding flows simulations have studied the role of magnetic fields in molecular cloud formation (Heitsch et al., 2007; Hennebelle et al., 2008; Banerjee et al., 2009; Heitsch et al., 2009; Vázquez-Semadeni et al., 2011; Chen & Ostriker, 2014; Körtgen & Banerjee, 2015). Some of these simulations (Heitsch et al., 2007; Hennebelle et al., 2008; Banerjee et al., 2009) have found power law relations between the magnetic field strength and density, similar to what is seen observationally, i.e.  $B \propto n^k$ , where  $1/2 < k < 2/3$  for  $n > 100 \text{ cm}^{-3}$ , and  $k = 0$  for  $n < 100 \text{ cm}^{-3}$  (Troland & Heiles, 1986; Crutcher, 1999; Crutcher et al., 2010; Tritsis et al., 2015). The inclusion of fields in the models also reduces the star formation rates to values more in agreement with observations (Vázquez-Semadeni et al., 2011; Chen & Ostriker, 2014). Such a reduction has been claimed to result from lower degrees of turbulent substructure found in the simulations (Heitsch et al., 2007; Hennebelle et al., 2008; Heitsch et al., 2009; Chen & Ostriker, 2014).

While the colliding-flows model has proved useful for understanding transient molecular cloud formation, the great majority of work has focused on head-on collisions, with no obliquity in the initial shocks formed in the flow. It is therefore worthwhile to explore the consequences of allowing the flows to interact at an interface initially inclined relative to incoming velocity vectors. Strong

shear in the interaction region will lead to significant shear in the post-shock flows, which can lead to stretching of embedded field lines and the possible generation of turbulence from KH modes. Recently, Körtgen & Banerjee (2015) studied the effect of varying the intersection angle between colliding flows. They found the high shear generated in the collision region reduced the star formation efficiency in the post-shock gas by disrupting the formation of high density structures.

The role of shear and magnetic fields in molecular cloud and protocluster formation is the subject of the present chapter, with a particular focus on the bulk fluid dynamics of these processes. Shear was generated in the models by keeping the converging flows parallel and varying the obliquity of the shock interface between the flows from normal (with respect to the oncoming flows), to highly inclined. All of the simulations included a uniform magnetic field aligned with the flows to simulate idealized ISM conditions. Self gravity, time-dependent cooling, and sink particles were also included in the models.

## 4.2 Methods

### 4.2.1 Numerical Model

The model setup was of two 40 *pc* diameter cylinders colliding in a 3D box under the influence of gravity, magnetic fields, and cooling (Fig. 4.1). Gravity and cooling source terms were solved using a Strang-split corner upwind transport (CTU) scheme that was 2nd-order accurate in time, as described in Chapter 2 (Sections 2.5 and 2.4). This was combined with a directionally unsplit CTU scheme for the 3D ideal magnetohydrodynamics (MHD) equations, using the HLLD Riemann solver. Gravitational interactions included both the self-gravity of the gas, as well as the gravitational acceleration due to sink particles.

A uniform magnetic field was initialized everywhere in the box, parallel to the flows. The field was initially dynamically weak, with  $\beta = 10$  and  $\beta_{ram} \approx 3.8$  at the start of the simulations (note,  $\beta$  is the ratio of thermal to magnetic pressure, and  $\beta_{ram}$  is the ratio of ram to magnetic

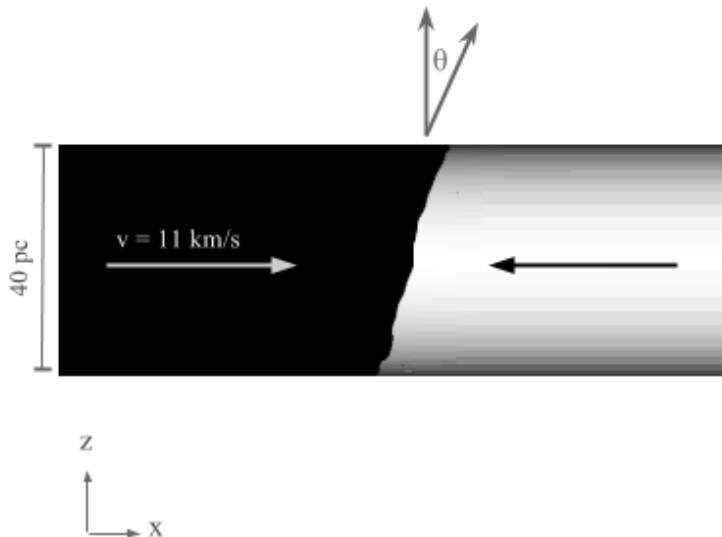


**Figure 4.1:** Physical model. Two oppositely driven cylindrical flows intersected at an angle  $\theta$ , rotated about the  $y$ -axis. The interface was perturbed with a random sequence of sine waves. The flows were homogeneous and embedded in a stationary, uniform ambient medium of the same density and pressure. The setup was initialized with a uniform magnetic field in  $x$ , parallel to the direction of the colliding flows.

pressure). The field had an initial strength of  $B = 1.3 \mu\text{G}$ , which is at the lower end of current ISM magnetic field estimates (Beck, 2001; Heiles & Troland, 2005). Cooling and heating were included using a parameterized cooling curve adapted from Inoue & Inutsuka (2008) to include the effects of self-shielding, as described in Chapter 2 (Section 2.5).

The simulations had 5 levels of AMR for a finest cell size of  $\Delta x_{\min} = 0.05 \text{ pc}$ . Given this resolution, individual sink particles that formed within the collapsing gas represented *protoclusters*, rather than protostars (as they did in previous work, c.f. Chapter 3 on single protostellar collapse models). The names ‘sink’ and ‘protocluster’ will therefore be used interchangeably throughout this

**Table 4.1:** The suite of simulations.  $\theta$ ,  $L_x$ ,  $L_y$ ,  $L_z$ , and  $t_{sim}$  denote the inclination angle, box dimensions, and final simulation time, respectively. The box size was increased in two of the runs to accommodate the steeper angle. The final simulation time was extended in the  $\theta = 60^\circ$  case to check for sink particle formation.

$\theta$ ( $^\circ$ )	$L_x$ (pc)	$L_y, L_z$ (pc)	$t_{sim}$ (Myr)
0	62.5	75	27.3
15	62.5	75	27.3
30	200	75	27.3
60	200	75	32.8

chapter.

### 4.2.2 Simulation Parameters

The suite of simulations consisted of four runs, each with a different orientation of the collision interface, specified by the inclination angle  $\theta$  (Table 5.1). The inclination angle was varied between  $\theta = 0^\circ$  and  $\theta = 60^\circ$ , i.e. between a head-on and highly inclined collision. This translated into the difference between a normal shock at the collision layer and an oblique shock. All parameters for the present suite of runs were the same as the ‘smooth’ model of Carroll-Nellenback et al. (2014), with the exception of the magnetic field and the variation of the collision interface (the smooth run was a hydro, head-on collision). We will therefore compare the  $\theta = 0^\circ$  run to the smooth run to study the effect of the magnetic field alone. Hence, the smooth run from here on out will be called the ‘hydro version of the  $\theta = 0^\circ$  case’ (or, the ‘hydro run’, for short).

The flows had a mach number of  $M = 1.5$  and were injected into a stationary ambient medium at a velocity of  $v = 11 \text{ km s}^{-1}$ . The mean molecular weight was constant and set to  $\mu = 1.27$ , and the ratio of specific heats to  $\gamma = 5/3$ . The gas was initially in thermal equilibrium at a uniform number density of  $n = 1 \text{ cm}^{-3}$ , corresponding to the linearly stable, warm neutral medium (WNM)

phase of the cooling curve. This set the thermal pressure and temperature everywhere inside the box to be  $P_{therm} k_B^{-1} = 4931 \text{ K cm}^{-3}$ , and  $T = 4931 \text{ K}$ , where  $k_B$  is the Boltzmann constant. The ram pressure of each flow was  $P_{ram} k_B^{-1} = 18,500 \text{ K cm}^{-3}$ , giving a total mass flux into the collision region of  $M_{flux} \approx 886 M_\odot \text{ Myr}^{-1}$ .

As in previous simulations, the collision interface was seeded with a set of random sinusoidal perturbations to excite the nonlinear thin shell (NTS) and Kelvin Helmholtz (KH) instabilities (Heitsch et al., 2006; Carroll-Nellenback et al., 2014). These perturbations had a maximum amplitude of  $A = 2 \text{ pc}$ , spectral index  $\alpha = -2.0$ , and maximum wave number  $k_{max} = 16 \text{ pc}^{-1}$ . Boundary conditions on the box were set to inflow-only on the faces where the flows were injected, and extrapolating on all other faces. The boundary conditions for the gravity solver were set to multipole expansion.

The simulations were initialized to 3 levels of AMR, with the finest cells centered on the collision interface within a cylindrical volume  $40 \text{ pc}$  in diameter and  $20 \text{ pc}$  long, and the coarser meshes nested outwards from there. This made for an *initial* effective resolution of  $\Delta x_{eff} = 0.2 \text{ pc}$ . Two additional levels were triggered throughout the simulation based on gradients in the fluid variables, as well as resolution of the local Jeans length ( $\lambda_J$ ), such that if a cell's  $\lambda_J$  was smaller than 64 zones on that cell's level, another level of AMR would be added. This brought the finest cell size to  $\Delta x_{min} = 0.05 \text{ pc}$ , as previously stated. The final simulation time for all of the runs was  $t_{sim} = 27.3 \text{ Myr}$ , with the exception of the  $\theta = 60^\circ$ . This was the only run that did not form any sink particles by this time, and so was extended out until  $t_{sim} = 32.8 \text{ Myr}$ .

In what follows, the analysis will focus mainly on the  $\theta = 0, 15$ , and  $60^\circ$  cases, as the  $\theta = 30^\circ$  case did not significantly differ from the  $\theta = 15^\circ$  case.

### 4.3 Generating Shear via an Oblique Collision Interface

The jump conditions across an oblique, 1D, shock-bounded slab convert initially intersecting velocity vectors into a shear flow field. As a measure of the shear for the present setup, mass weighted histograms of the magnitude of the vorticity were produced ( $||\nabla \times \vec{v}||$ ) in cylindrical analysis regions centered on the collision region. Each of these ‘hockey pucks’ encompassed the corresponding collision region by tracing the collision interface and extending out to  $5 pc$  on either side of the interface. They were normalized to contain the same amount of mass ( $1,000M_{\odot}$ ). Histograms were generated at  $t = 1 Myr$ , which is approximately the time it would take a post-shock sound wave to travel from the center of the CF cylinder to the outer boundary.

As can be seen in Fig. 4.2, lower shear runs (i.e.,  $\theta = 0 - 15^{\circ}$ ) have significantly more mass at lower vorticity ( $||\nabla \times \vec{v}|| < 100$ ), than at higher. As the collision angle increases to  $\theta = 30^{\circ}$ , two changes occurred. First, the amount of mass at  $||\nabla \times \vec{v}|| \leq 1$  decreases considerably. Second, more of the mass moves to higher vorticity. As the collision angle steepens to  $60^{\circ}$ , this trend strengthens. For the  $\theta = 60^{\circ}$  case, there is negligible mass at the lowest  $||\nabla \times \vec{v}||$ . That is to say, nearly all of the mass has acquired vorticity in this run. Moreover, *most* of the mass has acquired high vorticity ( $||\nabla \times \vec{v}|| > 10$ ).

Thus, as the inclination angle increases, more vorticity is generated in the collision layer. This vorticity can be associated with the solenoidal mode of the post-shock turbulence (Federrath et al., 2010b). Turbulent solenoidal fluid motions are efficient in providing support against collapse. Compared to compressive modes of turbulence, Federrath & Klessen (2012) show that solenoidal modes greatly reduce the star formation rate in turbulent, magnetized clouds. The passage of gas through the oblique shocks of our simulations thus transforms the compressive nature of the flows into solenoidal. In this way, our higher shear cases should exhibit greater degrees of turbulent support.

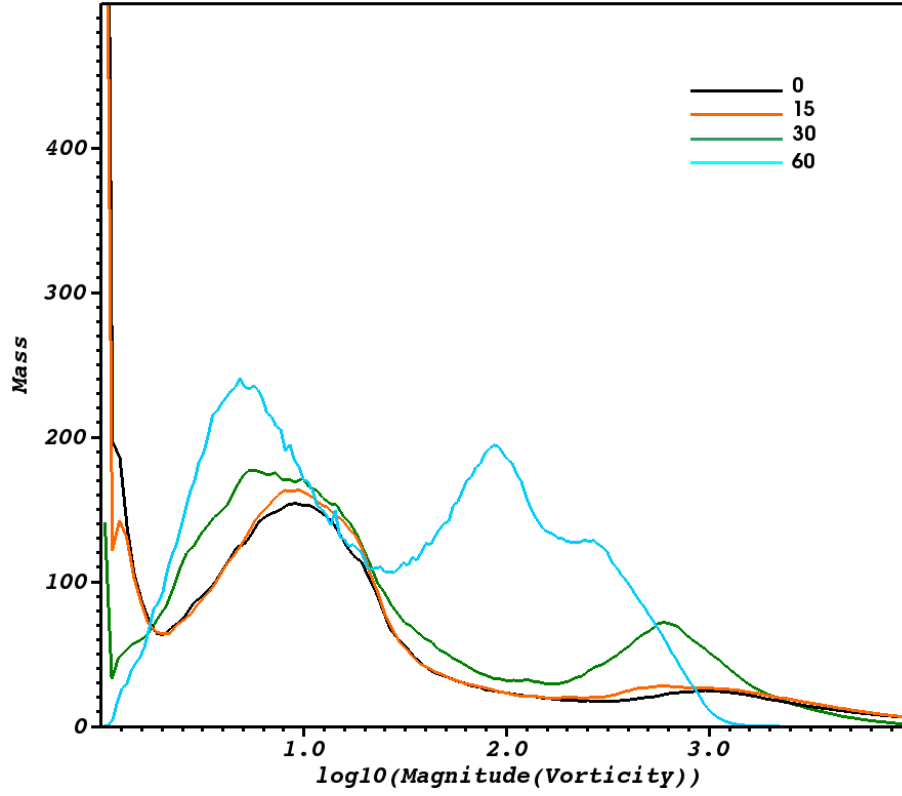


**Figure 4.2:** Mass-weighted vorticity histograms at  $t = 1 \text{ Myr}$ . The legend gives the inclination angle ( $^\circ$ ) of the given run. Each of the histograms were binned from a cylindrical analysis region centered on the given collision interface (see text), and were normalized to contain  $1,000 M_\odot$ . Units are scale-free, where the scale factors are given by  $MM_\odot^{-1} = 100$ ,  $ll^{-1}(pc) = 1$ ,  $vv^{-1}(cms^{-1}) = 8091$ .

## 4.4 Mass-to-flux Ratio

Before reviewing the results of the simulations, let us first consider some general issues associated with gravitational stability and magnetic fields that are relevant to the present work, beginning with the critical mass-to-flux ratio (M2FR) of cylindrical uniform flows. The M2FR compares the relative strength of the magnetic field to gravity. It does not take into account other forces which oppose gravity, such as thermal or ram pressure forces. The M2FR is given by

$$\mu_{crit} = \frac{\Sigma}{B} \approx \frac{1}{\sqrt{4\pi^2 G}} \quad (4.1)$$

where  $\Sigma$  is the mass column density and  $B$  is the magnetic field threading the cylinder (Nakano & Nakamura, 1978). Equation 4.1 can be rearranged for the *critical length* of the cylinder. In terms of typical ISM values, this is given by

$$L_{crit} \approx 470 \text{ pc} \left( \frac{B}{5 \mu G} \right) \left( \frac{n}{\text{cm}^{-3}} \right)^{-1} \quad (4.2)$$

where  $n$  is the number density (Vázquez-Semadeni et al., 2011). For the initial WNM values of the flows ( $n = 1 \text{ cm}^{-3}$ ,  $B = 1.3 \mu G$ ), Eqn. 4.2 gives a critical length of

$$L_{crit,WNM} \approx 122 \text{ pc} \quad (4.3)$$

for the WNM component of the gas. Using this, we can ask whether we would expect the warm gas to be magnetically supercritical. We first have to define a length scale over which we will check stability. Naturally this would be the collision region, as this is where the molecular clouds will be forming. As we will see, the width of this region ( $L_{coll}$ ) is on the order of  $10 \text{ pc}$ . This means that over the length scale of the collision region, the flow would be *sub*-critical. That is, given  $L_{crit} \gg L_{coll}$ , the magnetic field, at least initially, should be strong enough to withstand gravity.

Given the mass flux into the collision region along the colliding flows, one can ask ‘*how*

long will it take to accumulate enough mass into the collision region for the collision region to go unstable?’ For this, it is helpful to recast Eqn. (4.2) in terms of the critical column number density

$$N_{crit} \approx 1.45 \times 10^{21} \left( \frac{B}{5\mu G} \right) cm^{-2} \quad (4.4)$$

(Vázquez-Semadeni et al., 2011). For simplicity, we imagine the collision region to be initially massless. Its column density as a function of time is then

$$N(t) = 2nvt \quad (4.5)$$

where  $v$  is the speed of the flows. Equating this to Eqn. (4.4) and solving for  $t$  gives the time scale for the collision region to become magnetically supercritical:  $t_{crit} \approx 6 \text{ Myr}$ . Thus, the collision region is expected to *very quickly* (i.e.  $t_{crit} \ll t_{sim}$ ) become magnetically supercritical. While this is only an order of magnitude estimate, when taken in an average sense (over the collision region), it implies that the *mean* field is unable to support the collision region against collapse.

Despite this prediction of a weak field, large-scale, global collapse did not occur in the simulations. This can be attributed to the kinetic energy of the flows themselves, which also prevented global collapse in the hydro version of the  $\theta = 0^\circ$  case (Carroll-Nellenback et al., 2014), rather than the magnetic field. Thus, the M2FR should be used with caution for estimating global stability within the colliding flows model.

Next, let us consider smaller scales – those associated with the cold, dense phase out of which molecular clouds form. The cold neutral medium (CNM) in the simulations had number densities of approximately  $n \approx 500 \text{ cm}^{-3}$ . For the same initial uniform magnetic field, the critical length for the CNM is,

$$L_{crit,CNM} \approx 0.2 \text{ pc} \quad (4.6)$$

As we will see, column density structures associated with the CNM were typically much larger in width than this. Thus, widespread *local* collapse (i.e. over length scales associated with the cold component of the gas) might be expected to occur in the simulations.

However, widespread local collapse did not occur. Clearly, the magnetic field assumption in the M2FR calculation was in error. Turbulent instability behind the shocks would have deformed the magnetic field, thereby producing strong field fluctuations. It can thus be expected that field amplification within the cold, dense gas inhibited collapse *locally*, and only after this excess magnetic energy was lost (e.g. through numerical reconnection), could collapse proceed. Thus, the cold clumps were likely to be largely *sub*-critical in these simulations, and this could have been shown through a more rigorous calculation of the local M2FR. While such a calculation was beyond the scope of the present study, others have worked on calculating the local M2FR in simulations (Banerjee et al., 2009; Vázquez-Semadeni et al., 2011; Chen & Ostriker, 2014).

Thus, issues of local vs. global collapse, and the mechanisms by which collapse can be inhibited, such as, turbulence and field amplification, will be emphasized in the following sections. In particular, consider that for large values of the inclination angle  $\theta$ , post-shock flows can retain a significant fraction of their pre-shock velocity. As shear leads to turbulence, it can be expected that the turbulent velocity will be some fraction of the incoming velocity ( $v_{turb} \propto f v_o$ ). If turbulence provides support to the cloud against collapse, then enhancements of the local Jeans length due to turbulence ( $\lambda_{turb}$ ) can be expected to be on the order of,

$$\frac{\lambda_{turb}}{\lambda_J} \propto \frac{f v_o}{c_s(\mathbf{x})} \quad (4.7)$$

where  $c_s(\mathbf{x})$  is the local sound speed. Thus, depending on the fraction of inflow velocity retained by the turbulence, the collision region in flows with shear should be more stable to collapse than those without shear. In addition, any degree of turbulence will produce local field amplifications (i.e. additional support against collapse), which as stated, was not accounted for by the M2FR analysis

presented above.

## 4.5 Protocluster Formation and Evolution

Let us now turn to the principle result of this chapter, which is how shear and magnetic fields directly affect star formation in terms of the creation of sink particles. Again, while sink particles in the simulations had masses that should be associated with clumps (i.e. protoclusters), if higher levels of resolution were included, these clumps would be expected to form cores, which would then collapse to form individual stars.

Fig. 4.3 presents the final masses of sink particles as a function of their formation time for the various runs. This plot relays three pieces of information that show the effect of shear. First, the total number of protoclusters formed in each of the runs *decreased* with shear. The number decreased from four protoclusters in the  $\theta = 0^\circ$  case, to one in the  $\theta = 30^\circ$  case, to zero in the  $\theta = 60^\circ$  case (within  $t = 27 \text{ Myr}$ ). Only after extending the  $\theta = 60^\circ$  case out another  $5 \text{ Myr}$  did a protocluster eventually form, as shown in the figure. While this trend did not hold for the  $\theta = 15^\circ$  case, which formed a couple of low mass protoclusters late in the simulation, it is clear that the initial inclination angle of the colliding flows interface directly impacted post-shock support against collapse.

Second, higher levels of shear *delayed* the formation of protoclusters. The  $\theta = 0^\circ$  case produced a protocluster by  $\approx 11 \text{ Myr}$ , whereas the  $\theta = 15^\circ$  case did not produce a protocluster until  $\approx 18 \text{ Myr}$ . As stated above, the  $\theta = 60^\circ$  was inhospitable enough to star formation that protocluster formation was delayed until  $\approx 32 \text{ Myr}$ . This shows that the various simulations were evolving under different time scales. This can be understood by considering  $t_{crit}$  – the time it takes to acquire enough material into the central region to go magnetically supercritical. As the inclination angle was varied, the velocity in Eqn. 4.5 would have become  $v' = v \cos \theta$ , due to deflection at the collision interface (i.e. the generation of shear). Thus, the critical time scale for shear environments is related

to  $t_{crit}$  by,

$$t'_{crit} \propto t_{crit}(\cos \theta)^{-1} \quad (4.8)$$

This equation predicts longer time scales for gravitational instability in higher shear environments, consistent with the increased time to form protoclusters, and the overall reduction in protocluster number. Note that while the  $\theta = 30^\circ$  case does disagree with this result (forming its single protocluster before the  $\theta = 15^\circ$  case), this sink particle was extremely low mass despite having ample time to grow. This indicates that while local collapse occurred in the region where the protocluster formed, the shearing motions generated by the initial inclination angle of the interface inhibited further growth.

Third, shear *slowed* growth of protoclusters, i.e. higher shear cases had lower average accretion rates ( $\langle \dot{M} \rangle = M_{final}/(t_{sim} - t_{sink})$ ). For example, consider the two protoclusters that formed at  $t \approx 24 \text{ Myr}$ . For this pair, the  $\theta = 0^\circ$  protocluster grew to be  $\approx 3\times$  more massive than its  $\theta = 15^\circ$  counterpart. This indicates that the environments surrounding the protoclusters were less bound in the higher shear runs (recall, only gravitationally bound and unstable gas in the surrounding zones can be accreted onto sink particles). The higher accretion rates of the lower shear simulations translated into more massive protoclusters.

The role of magnetic fields on dynamics can also be extracted from Fig. 4.3, as there was a significant reduction in the number of protoclusters formed in the  $\theta = 0^\circ$  case, compared to the pure hydrodynamic version of this run in Carroll-Nellenback et al. (2014). For the same final simulation time resolution, multiphysics, and sink particle algorithm, the hydro run formed a total of 27 protoclusters compared to the 4 formed in the  $\theta = 0^\circ$  case. Moreover, Carroll-Nellenback et al. (2014) found differences in the mass distributions of protoclusters depending on whether there was global or local collapse. The present protocluster masses are consistent with the mass distribution of the hydro run, which only exhibited local collapse. Taken together, this demonstrates the *local*

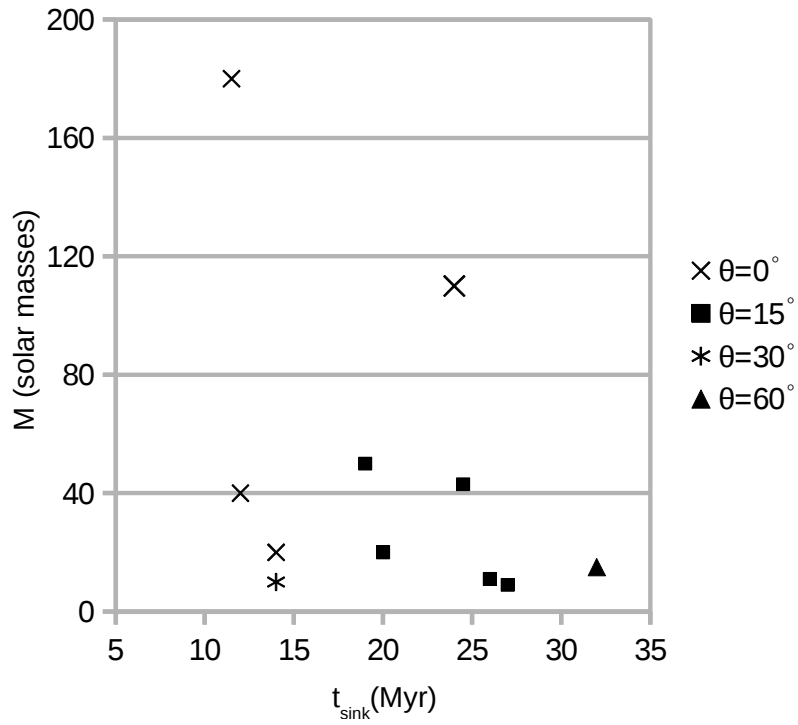


**Figure 4.3:** Final mass distribution of protoclusters as a function of formation time,  $t_{\text{sink}}$ . Note, the final simulation time was the same for the  $\theta = 0, 15$ , and  $30^\circ$  runs ( $t_{\text{sim}} = 27.3 \text{ Myr}$ ), but was longer for the  $\theta = 60^\circ$  case ( $t_{\text{sim}} = 32.8$ ). Also, mass accretion was not constant over time, but rather depended on environmental conditions.

support magnetic fields are providing against collapse, since neither the hydro or MHD runs showed evidence of global collapse.

Let us now compare the sink particles at a similar evolutionary time. Figure 4.4 shows the mass distribution of the sink particles at 1 *Myr*, post-formation. This time was chosen as it maximizes the accretion time of the  $\theta = 60^\circ$  sink. However, this time loses the final sink of the  $\theta = 15^\circ$  run, which had a lifetime  $< 1$  *Myr*. In the figure, each sink's mass at 1 *Myr* post-formation is connected by a line to the final mass of that sink. This provides a quick reference of the average accretion rates of the sink particles. Figure 4.4 shows that both the initial peak mass, as well as the average initial mass, decline with increasing shear (focusing on the left-most points of each pair). It is interesting that the  $\theta = 60^\circ$  case seems to contradict this behavior. However, this has to do with the reorientation of the collision interface (discussed in more detail below): by the time this sink particle forms, the initially steep collision angle had become largely normal to the oncoming flows. This would have reduced the degree of post-shock shear, and consequently the amount of support afforded to the surrounding envelope. Thus, the  $\theta = 60^\circ$  sink particle was able to accrete at a rate comparable to lower shear runs. Mass-weighted histograms of the vorticity in the collision region for the  $\theta = 60^\circ$  case shows that this has indeed occurred (Fig. 4.5).

To conclude this section, note that the accretion rates of the various sink particles were highly environmentally dependant. Some sinks were positioned in large regions of gravitationally unstable, collapsing gas compared to others, and this would have caused their accretion rates to be larger. This is why some of the sinks that have formed later in time have grown to be more massive than older sinks.

## 4.6 Morphology

Let us now turn to column density maps for a more detailed comparison of the flow evolution. Column density maps of the  $\theta = 0^\circ$  case are shown in Fig. 4.6. As can be seen in the left hand

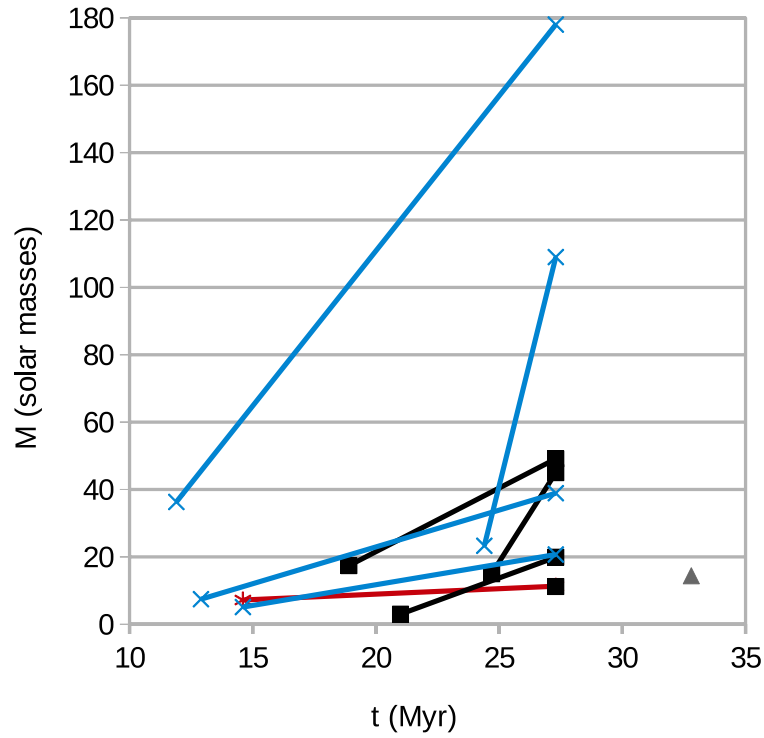


**Figure 4.4:** Masses of the various sink particles at 1 *Myr* after their formation with corresponding final masses. Each set of points (early and final mass), is connected by a line. The  $\theta = 0, 15, 30, 60^\circ$  cases are given by the blue, black, red, and grey lines, respectively. Note that the last sink particle for the  $\theta = 15^\circ$  case is not plotted, as that sink's lifetime was less than 1 *Myr*. The  $60^\circ$  is a single point as that sink lived for exactly 1 *Myr*.

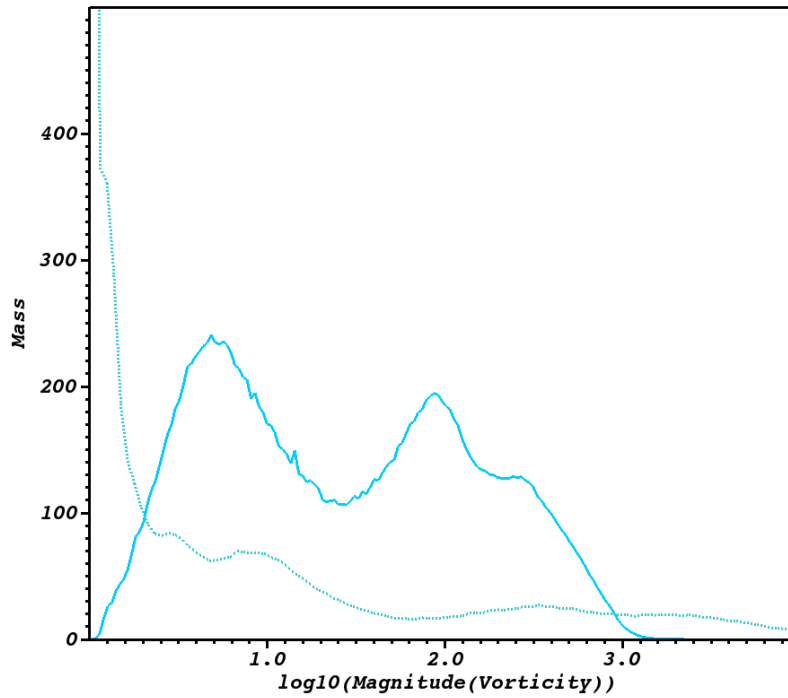


**Figure 4.5:** Mass-weighted vorticity histograms for the  $\theta = 60^\circ$  case at early and late times. Solid line is at  $t = 1 \text{ Myr}$ , dotted is at the end of the simulation ( $t = 32.8 \text{ Myr}$ ). Each of the histograms were binned from a cylindrical analysis region that was tilted  $60^\circ$  and contained  $1,000 M_\odot$ . Units are again scale-free.

panel, there is a large, ring-like structure surrounding the flows. This ring is an artifact of the simplified initial conditions, and its formation can be understood as follows. Initializing colliding flows as cylinders naturally produces a region where shocked gas is expelled laterally with respect to the cylindrical axis. Any colliding-flows geometry will produce a characteristic two shock structure (one to decelerate each flow), separated by a contact discontinuity. For finite-sized flows, there must also be a region where high pressure post-shock material is driven out of the collision region. Analysis of a similar process in time variable protostellar jets (which, with a change in reference frame are similar to the configuration studied here), shows that lateral motions on the order of the post-shock sound speed ( $c_{ps}$ ) carry material away from the interaction region along radial streamlines into the ambient gas (Raga, 1992). In this way, converging flows along the length of the cylindrical regions are converted into radial flows expanding away from the axis of the cylinders.

When magnetic fields are present, tension forces can restrict these lateral motions. The length and time scales for this restriction depend both on the field strength and geometry. Studies of magnetized time variable jets with strong cooling show that even initially weak toroidal fields can lead to the collapse of post-shock flows onto the axis (De Colle et al., 2008; Hansen et al., 2015). Thus, the ring-like structure present at approximately 30  $pc$  away from the center of the colliding flows can be attributed to the effect of magnetic tension, since it was not seen in the pure hydro case (Carroll-Nellenback et al., 2014). Such rings were also seen in other MHD colliding flows runs (Vázquez-Semadeni et al., 2011; Banerjee et al., 2009). Note that in the simulations presented here, the initial field was parallel to the colliding flows. Thus, as post-shock gas was driven outward from the interaction region, the flow drove arcs in the magnetic field (Fig. 4.7), whose tension eventually halted further expansion. The result is a ring of high density material in the collision plane. A calculation for the location of this ring is carried out in the appendix, and is in good agreement with the position of the ring visible here.

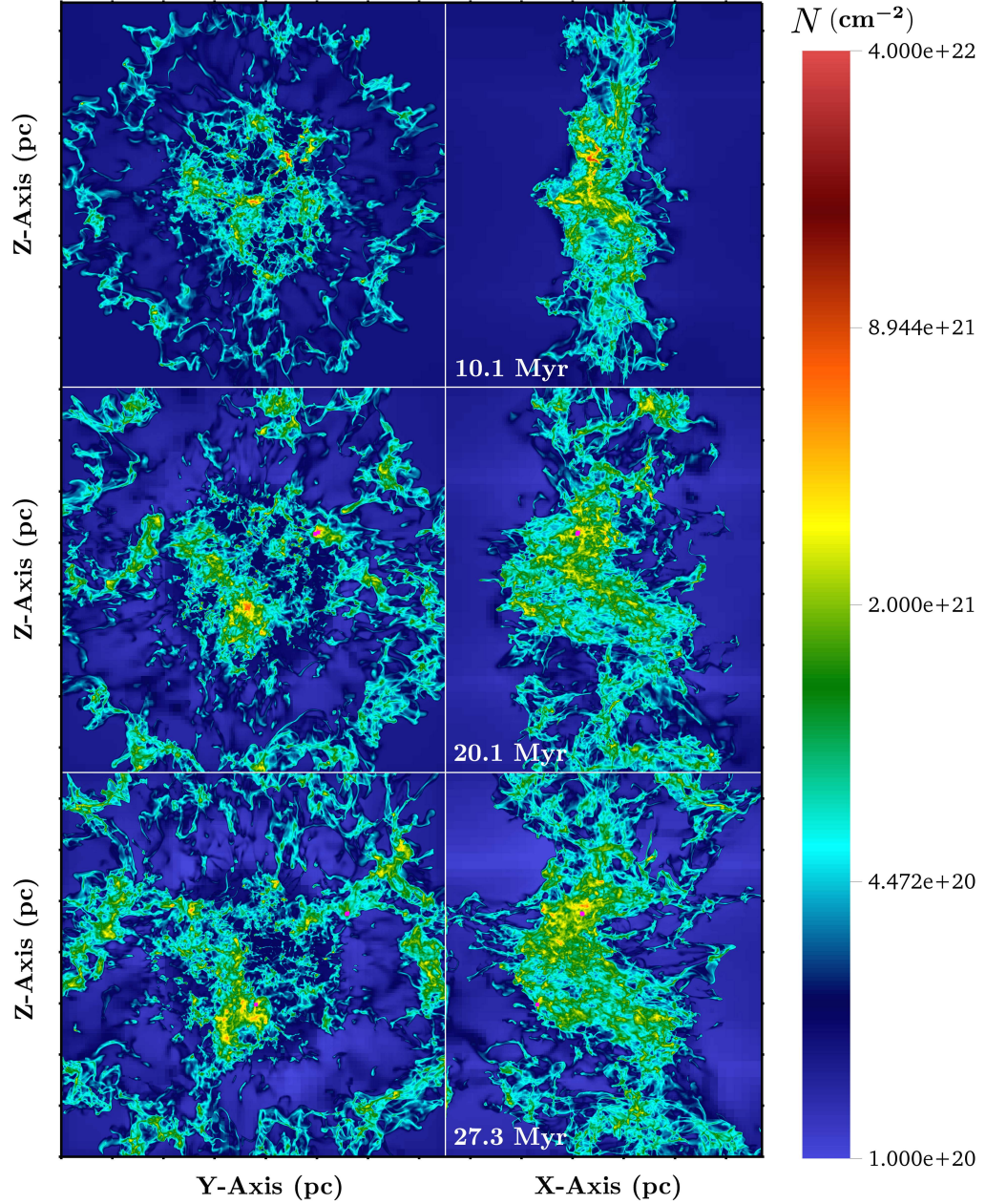


**Figure 4.6:** Column density map for the  $\theta = 0^\circ$  case. The integration length is the  $62.5\text{ pc}$  for the left-hand column and  $75\text{ pc}$  for the right-hand column in these and all subsequent column density maps. Sink particles are given as fuchsia points. Each tick mark represents  $10\text{ pc}$ .

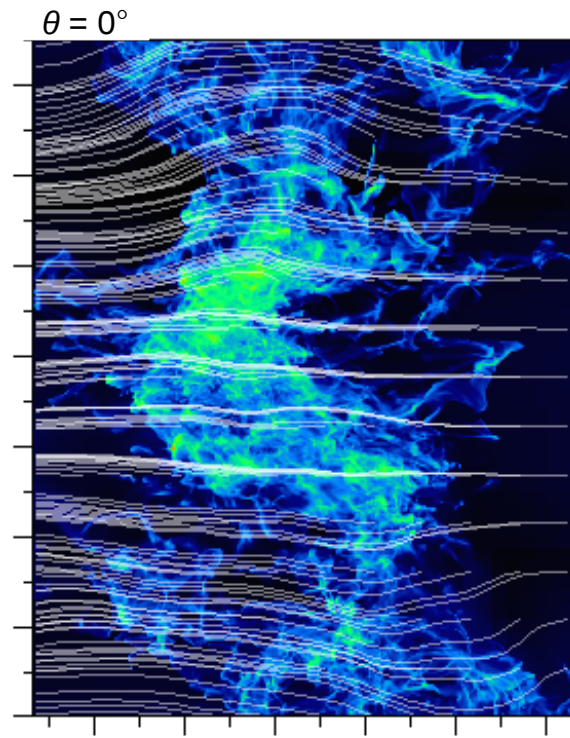


**Figure 4.7:** Streamline plot of  $B_x$  and  $B_z$  components of the magnetic field averaged along  $y$  as shown in the  $x - z$  plane for the  $\theta = 0^\circ$  case. Note the bending of the field lines as material is expelled from the collision region (see text for description).

### 4.6.1 Main Features in Column Density

Moving past considerations of the ring, let us now focus on the details of the flow in the collision region. Note that the incoming flows corresponded to WNM, which was at a column density of  $N \approx 2 \times 10^{20} \text{ cm}^{-2}$ . After passing through the shocks, the gas entered the collision region where the thermal instability drove the gas into the CNM state, which the probability density functions (PDFs) of Section 4.8 show was  $\approx 500\times$  denser. Note, the different phases in column density are identified loosely, based on morphology and relative mass fraction from previous studies (Heitsch et al., 2007; Hennebelle et al., 2008; Banerjee et al., 2009). In addition, the minimum  $H_I$  column density for UV-shielding ( $N_{HI} \approx 1 - 2 \times 10^{21} \text{ cm}^{-2}$ ) is used to label regions that have effectively become ‘molecular’ (van Dishoeck & Black, 1988; van Dishoeck & Blake, 1998). This is because to have accurately tracked the formation of molecular gas in these simulations, the code would have needed to include the physics of UV shielding by dust grains. In the images, dark blue regions are the initial WNM, cyan regions are thermally unstable gas, from which the CNM phase and subsequent molecular clouds form (green-yellow), and denser gas (i.e. clumps) within the molecular phase is shown in orange and red.

The structures visible within the interaction region of the  $\theta = 0^\circ$  case (Fig. 4.6) are morphologically similar to those of the hydrodynamic version of these runs (see fig. 2 in Carroll-Nellenback et al., 2014). However, the degree of heterogeneous or ‘clumpy’ structure appears to be lower in the present magnetized run. This impression is in-line with previous findings (Heitsch et al., 2007; Hennebelle et al., 2008; Heitsch et al., 2009; Chen & Ostriker, 2014), which report that fields tend to produce larger, more coherent filamentary structures, compared to their hydrodynamic counterparts.

The first frame of Fig. 4.6, taken at  $t = 10 \text{ Myr}$ , shows the gas shortly before the first protoclusters formed. By the next frame ( $t = 20 \text{ Myr}$ ), three protoclusters had formed close enough to each other that two of them overlapped and nearly overlapped the third (as can be seen by zooming in on the figure). The location of these sink particles was off-center from the flow axis,

indicating they did not form out of a global collapse mode. Instead, they were within local potential minima, associated with regions of high density gas that condensed out of the background turbulent environment and had become gravitationally unstable. By the last time panel of Fig 4.6, another protocluster had formed off-axis, roughly  $25 \text{ pc}$  away. This sink particle was in a large region of high  $N$ . Given this sink had the fastest average accretion rate of the  $\theta = 0^\circ$  run's protoclusters (Fig. 4.3), this region represents a large and deep potential well. Finally, we note that there was significant widening of the collision zone with time, due to the NTS, KH and thermal instabilities.

Let us now shift our attention to column density maps of the  $\theta = 15^\circ$  case (Fig. 4.8). At  $t = 10 \text{ Myr}$ , the collision region was structurally similar to the  $0^\circ$  case, except for regions of lower maximum  $N$  (see the left hand column of the plot). Thus, even at low inclination angles, the shear generated by the oblique shocks at the interface disrupted substructure formation to some degree. However, the flows were capable of assembling some localized structures dense enough to become molecular by this time.

By  $t = 20 \text{ Myr}$ , the first protocluster can be seen, having formed at  $t_{\text{sink}} \approx 17 \text{ Myr}$ . It is located near the axis as seen in the left hand panel of Fig. 4.8, but off-center, in one of the NTSI nodes as seen in the right-hand panel. Over time, the fingers of the NTSI grew, and by  $t = 27.3 \text{ Myr}$  the instability had become ‘z-shaped’, with a large component aligned with the flow axis. Also by this time, four additional protoclusters had formed. Two of these were in the same NTSI node mentioned above, and the other two were roughly  $10.2$  and  $21.9 \text{ pc}$  away, near the edge of the cylinder. The positions of all of these sink particles was again consistent with local instability being triggered in the flow.

Finally, let us consider the extreme  $\theta = 60^\circ$  case, which exhibited very different behavior than the other runs. Namely, the initial steep angle of the collision interface *reoriented over time* and became normal to the oncoming flows. Animations of the runs suggest the reorientation is due to perturbations at the collision interface seeding the NTSI. However, field line tension may have also played a role, as realignment is not as evident in the hydro version of this run (Haig & Heitsch

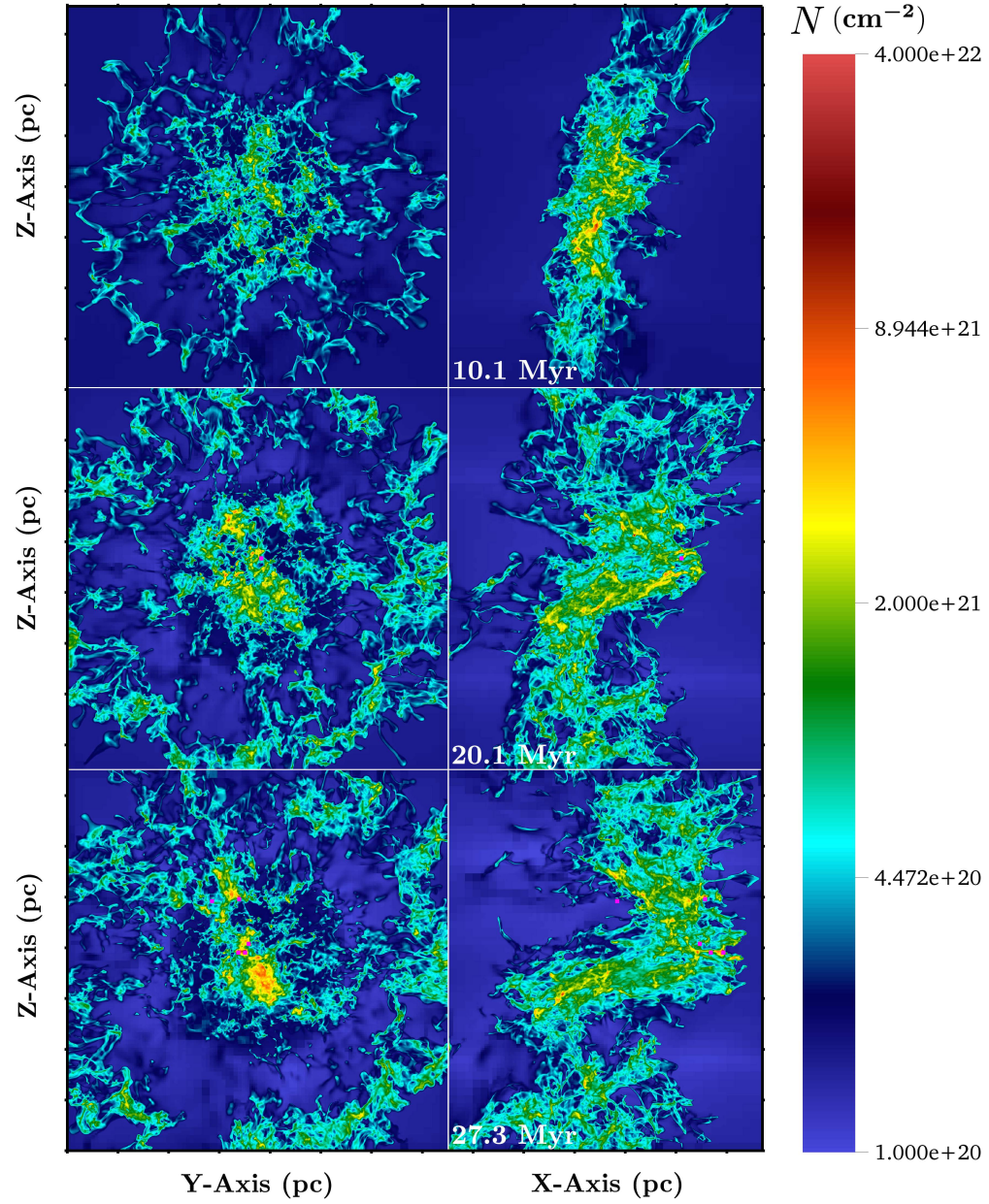


**Figure 4.8:** Column density map for the  $\theta = 15^\circ$  case. Sink particles are given as fuchsia points. Each tick mark represents 10 pc.

in prep).

Reorientation appears to begin in a region where the flow was nearly normal to the surface of an NTSI node (see the right panel of Fig. 4.9 at  $t = 10.1 \text{ Myr}$ ). Because of the high angle of the collision interface, most incoming material was deflected by the oblique shocks to flow parallel along the shock face. The NTSI node created a local distortion of the shock, allowing oppositely driven material to meet at lower obliquity. The gas behind this stronger shock had higher thermal pressure and began expanding in the (y,z) plane. This expansion increased the area of the low obliquity regions of the flow, which led to more high pressure post-shock gas as seen by  $t = 20.1 \text{ Myr}$  (Fig. 4.9, right). In this way, it appears the initially highly oblique shock region was transformed into a shock that was more normally directed, relative to the incoming flows. By  $t = 32.8$ , the shock had become nearly fully normal.

Beyond the reorientation behavior of this case, there are a few general characteristics of the  $\theta = 60^\circ$  collision interface to note. First, the collision region was less dense than in the other runs at  $t = 10.1 \text{ Myr}$  (Fig. 4.9, left). This suppression of growing high density regions arose from the strong shear. Incoming material was sharply deflected away from the axis of the cylinder, and thus less gas accumulated at early times. Second, the collision interface was thinner compared to the other runs at early times, because of this deflection of material away from the interaction region: material streamed out into the ambient medium, rather than building up along the flow axis. Only by  $t = 20 \text{ Myr}$ , given the reorientation of the shocks bounding the interaction region (and corresponding weaker degree of shear), did material begin to accumulate in the collision region (Fig. 4.9, left). By  $t = 32.8 \text{ Myr}$ , local collapse had set in and a single protocluster is visible on the CDM, again having formed away from the global potential minimum.

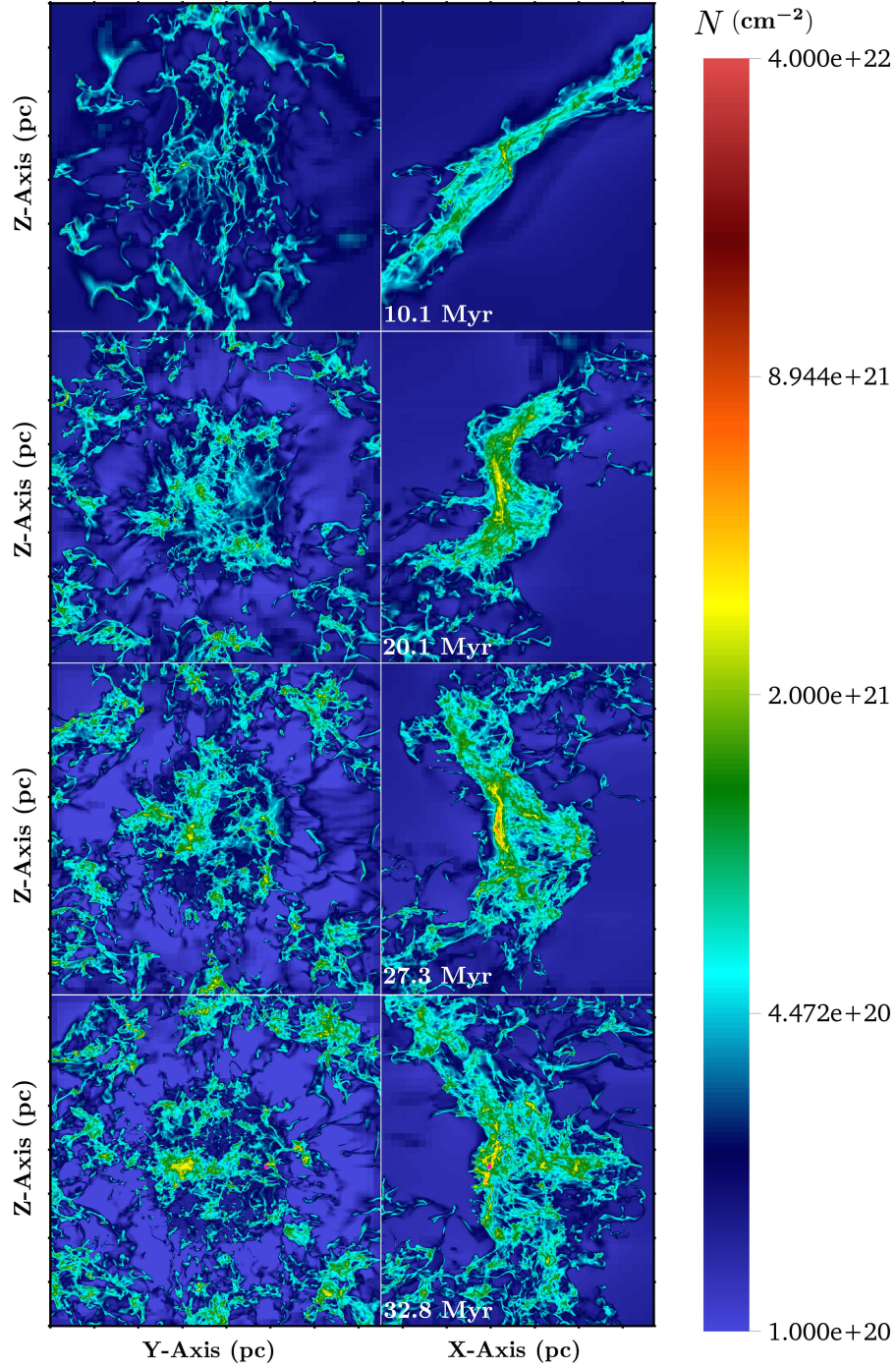


**Figure 4.9:** Column density map for the  $\theta = 60^\circ$  case. The single sink particle is given as a fuchsia point. Each tick mark represents 10  $pc$ .

## 4.7 Magnetic Fields and Dynamics: $\langle \beta^{-1} \rangle$ maps

To compare with the column density maps presented above, average  $\beta^{-1}$  maps were generated by discretely summing  $\beta^{-1}$  through the grid along the same lines of sight,

$$\langle \beta^{-1} \rangle = \frac{1}{L} \sum_{i=1}^{i=m_x} \beta_i^{-1} dx_i \quad (4.9)$$

where  $L$ ,  $m_x$ ,  $\beta_i^{-1}$ , and  $dx_i$  are the length of the box along the given dimension, number of cells along that dimension, value of  $\beta^{-1}$  at the  $i$ th cell, and the  $i$ th cell's width, respectively.

Beginning with the  $\theta = 0^\circ$  case, field amplification associated with the radial ejection of gas from the collision region (discussed in Section 4.6) produced a ring of high  $\langle \beta^{-1} \rangle$  at  $r \approx 30 \text{ pc}$  (Fig. 4.10, left). Additionally, there was another, inner ring present from  $t = 10.1 \text{ Myr}$  on at a distance of  $r \approx 15 \text{ pc}$  from the center of the colliding flows that did not appear in the CDM's. This ring was not contained in the collision region itself, as can be seen from the right-hand frames of Fig. 4.10. Rather, it stretched down the length of the cylinder, peaking in brightness near the outer edge. This indicates it was generated by the strong shear present at the boundary between the colliding flows and the stationary ambient medium. This shear layer would have caused strong cooling and therefore a decrease in thermal pressure (hence the increased  $\langle \beta^{-1} \rangle$  along this boundary).

Looking along the colliding flows axis at  $t = 10.1 \text{ Myr}$  (Fig. 4.10, left), there are regions inside of the collision region where  $\langle \beta^{-1} \rangle$  had increased above its initial value of  $\beta^{-1} = 0.1$ . A glance back at Fig. 4.6 shows these regions are co-located with regions of high column density  $N$ . In some of these regions,  $\langle \beta^{-1} \rangle$  had increased by a factor of 10 or more. Since this material is associated with the CNM phase (as discussed in Section 4.6), its thermal pressure was *at least* equal to its initial value (cf. Section 4.8). Thus, in order for  $\beta^{-1}$  to have increased by this amount, the magnetic pressure must have increased by a factor of 10 or more. This supports that the field was being strongly amplified in the high density gas.

On the other hand, regions where  $\langle \beta^{-1} \rangle$  was reduced below its initial value are also visible.

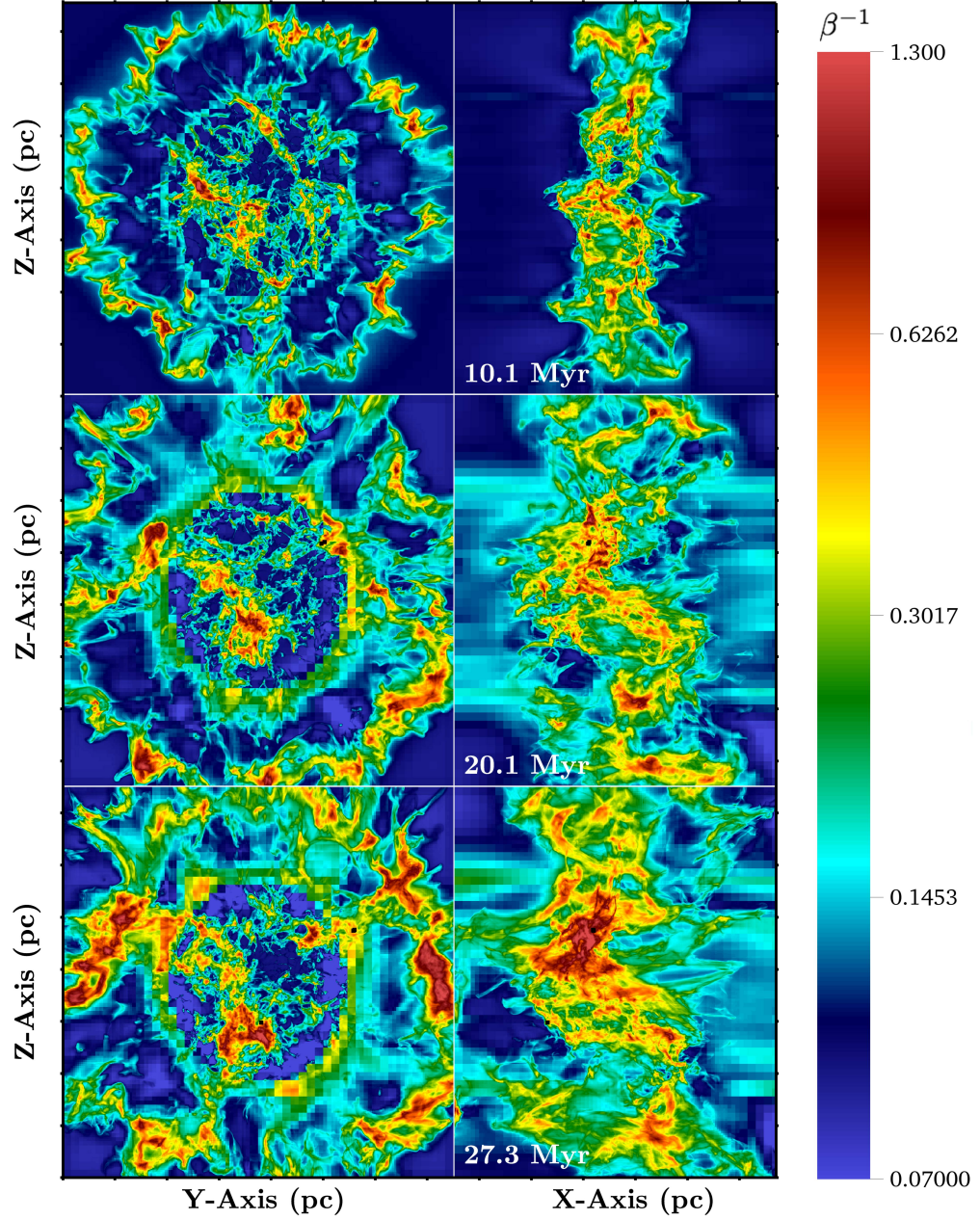


**Figure 4.10:** Average  $\beta^{-1}$  map for the  $\theta = 0^\circ$  case (see Eqn. 4.9 for definition). Sink particles are given as black points. Each tick mark represents 10 pc.

These ‘voids’ (shown in the lowest color on the color bar) generally correspond with regions of low  $N$ . Since flux freezing implies the accumulation of flux is co-extensive with regions of high density, the voids were formed as material was swept away by both turbulence and the collapse of gas into neighboring potential minima. In other words, voids are associated with regions that have a net positive  $\nabla \cdot v$ . Thus, regions of low  $N$  should not be strongly magnetized, consistent with the voids in Fig. 4.10. As the simulation evolved, there was an increase in the size of both the magnetic voids, as well as the ‘magnetic islands’ (regions of high  $\langle \beta^{-1} \rangle$ ).

The ramifications of magnetic fields on the dynamics of the flow were already discussed in Section 4.5. The presence of magnetic islands co-located with regions of high  $N$  support that magnetic fields suppress star formation *locally*. This is further supported by the location of forming protoclusters. As seen in the  $t = 20.1$  and  $27.3 \text{ Myr}$  panels, protoclusters formed *away* from regions of highest  $\langle \beta^{-1} \rangle$ . That is, protocluster formation was inhibited where the field was the strongest. Instead, protoclusters formed where the gas was dense, but  $\langle \beta^{-1} \rangle \lesssim 0.6$ .

$\langle \beta^{-1} \rangle$  maps of the  $\theta = 15^\circ$  case (Fig. 4.11) are similar to the case with no shear. Regions of high  $\langle \beta^{-1} \rangle$  are associated with high  $N$  structures. There was also a similar formation of magnetic voids. The shear angle present in these runs does, however, leave a signature in the  $\langle \beta^{-1} \rangle$  maps early in the simulation. Looking down the axis of the flows at  $t = 10.1 \text{ Myr}$ , it is evident that there are weaker regions of enhanced  $\langle \beta^{-1} \rangle$  (Fig. 4.11, left). This likely occurs because of the way incoming flows were redirected away from the axis, due to the oblique shocks. Whereas material was driven away from the collision region with radial symmetry in the  $\theta = 0^\circ$  case, material here picked up positive and negative  $v_z$  components across the contact discontinuity. The field lines threading the interaction region must have therefore undergone a local stretching and may have been shorted out by numerical diffusion. This is in contrast to the large scale arcs of field which formed in the purely radial flows of the  $\theta = 0^\circ$  case.

Fig. 4.12 shows a very different set of  $\langle \beta^{-1} \rangle$  maps for the  $\theta = 60^\circ$  case. First note that projected along the axial view almost no regions of high  $\langle \beta^{-1} \rangle$  are visible. This is because the

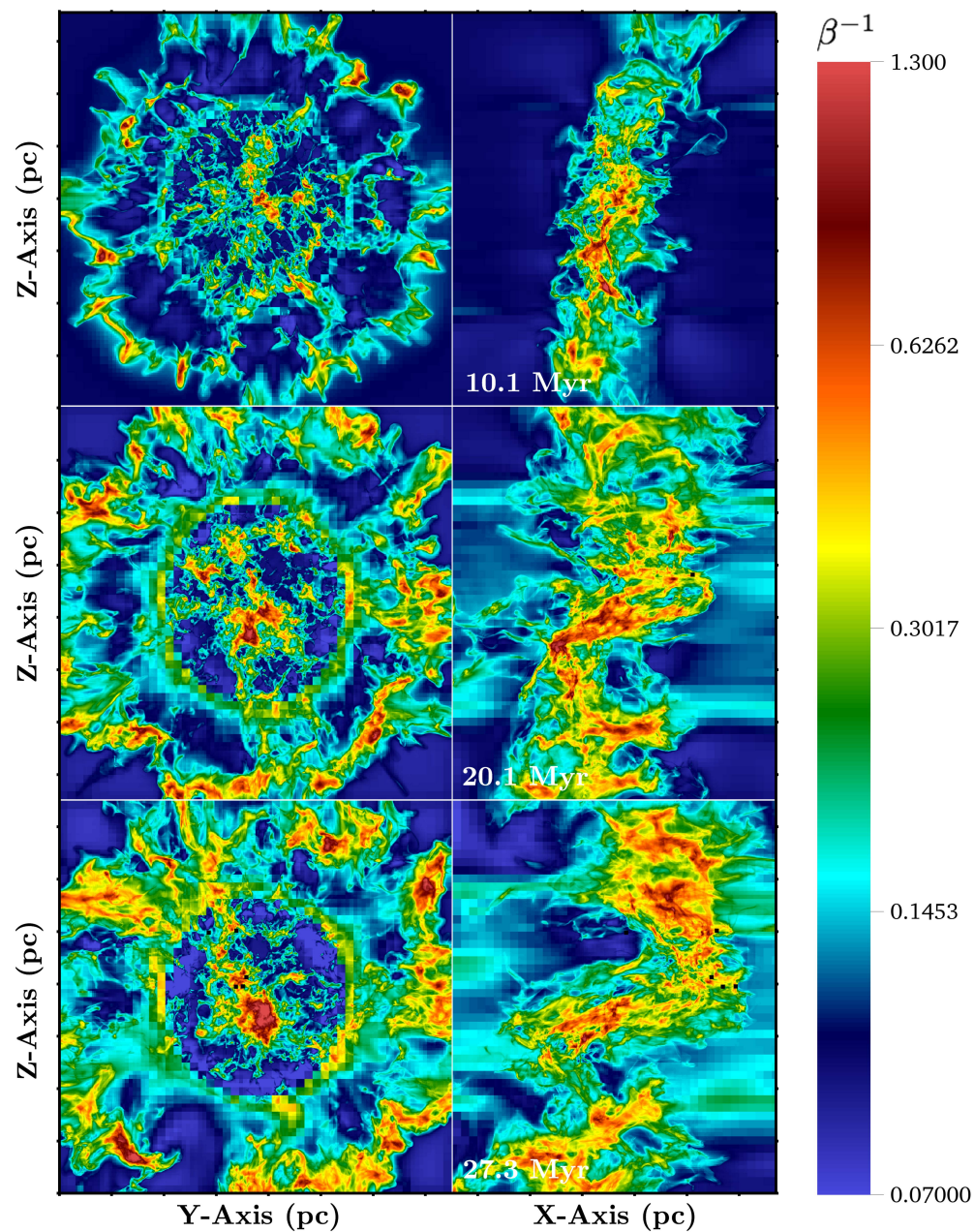


**Figure 4.11:** Column  $\beta^{-1}$  map for the  $\theta = 15^\circ$  case. Sink particles are given as black points. Each tick mark represents 10 pc.

interaction region remained quite thin early on as gas passed through the oblique shock and was quickly shunted away from the central region. When seen from the side, however, (Fig. 4.12, right) significantly higher values of  $\langle \beta^{-1} \rangle$  are visible within the collision region. This reflects both the projection through the thin interaction region, as well as the strong local field amplification that occurred due to the shear: field lines must have assumed a ‘z’-shaped configuration as gas moving from the left was driven upward by the oblique shock it encountered, and gas moving from the right, across the contact discontinuity, was driven downward by the oppositely oriented oblique shock it encountered.

Note that as the collision region reoriented from  $t = 20.1 \text{ Myr}$  onward, more material and field collected inside of the interaction region in the same manner as was discussed in the lower shear cases. This accounts for the increased regions of high  $\langle \beta^{-1} \rangle$  seen in the left hand side of Fig. 4.12 at later times, although overall these regions were much smaller than their lower shear counterparts.

## 4.8 Thermodynamics: Probability Density Functions

The thermodynamic evolution of the gas is now examined, as gas was first shocked in the flow collision and then cooled into a cold, dense state, which could then undergo further compression due to gravity, or expansion due to magnetic fields. The probability density functions (PDFs) in this section give the amount of mass at a given pressure and number density. The  $y$ -axis gives both scaled magnetic *and* thermal pressure (marked by the color and gray scales, respectively), and the  $x$ -axis gives number density  $n \text{ (cm}^{-3}\text{)}$ . Isotherms are straight lines of slope  $m = 1$  on these PDF log-log plots, and increase in temperature diagonally from the bottom-right corner of the panels to the upper-left.

To begin, note that the thermal pressure distribution in all of the runs was identical to previous colliding flows studies (i.e. *grey-scale* PDFs, Fig’s 4.13-4.15). Namely, gas was shocked and heated as it entered the collision region and via the thermal instability, cooled down until it reached the

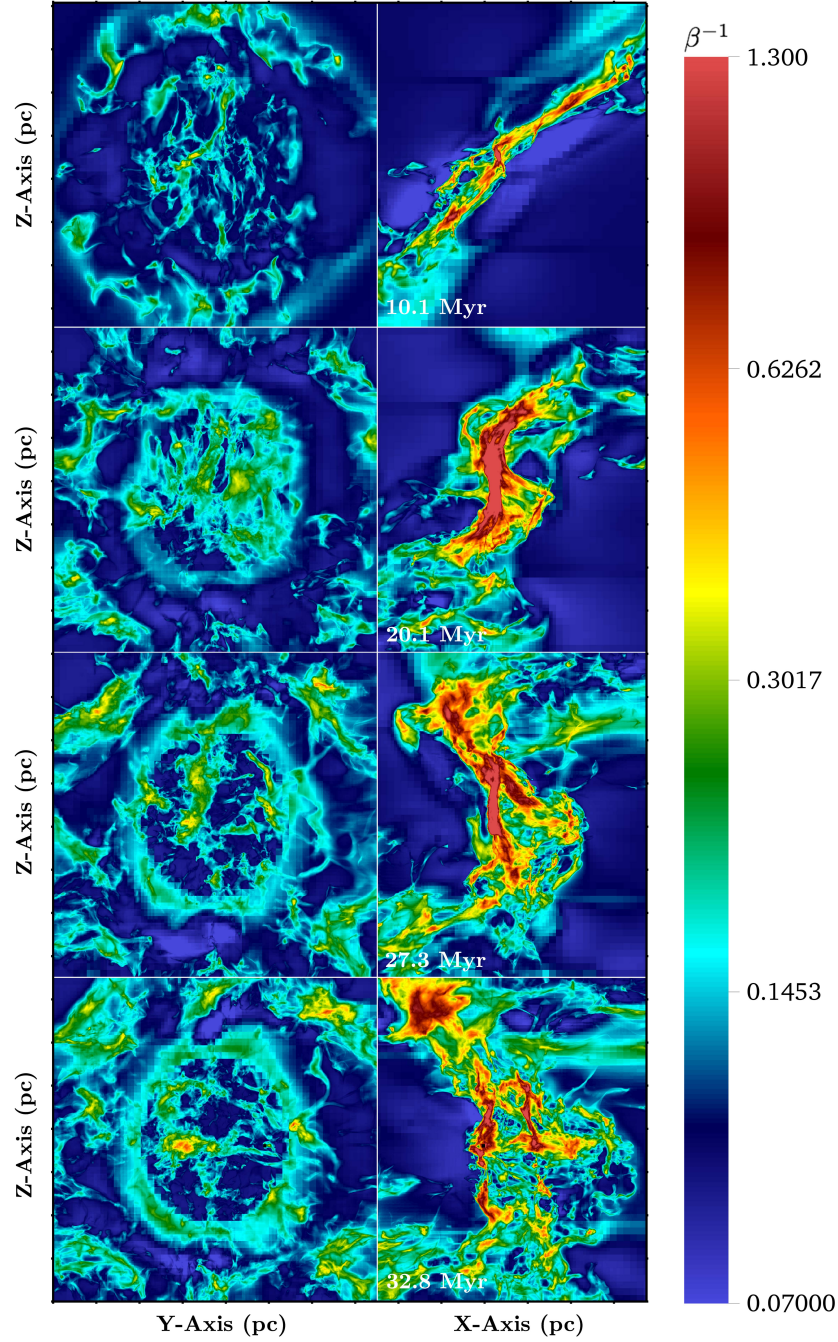


**Figure 4.12:** Column  $\beta^{-1}$  map for the  $\theta = 60^\circ$  case. The single sink particle is given as a black point. Each tick mark represents 10 pc.

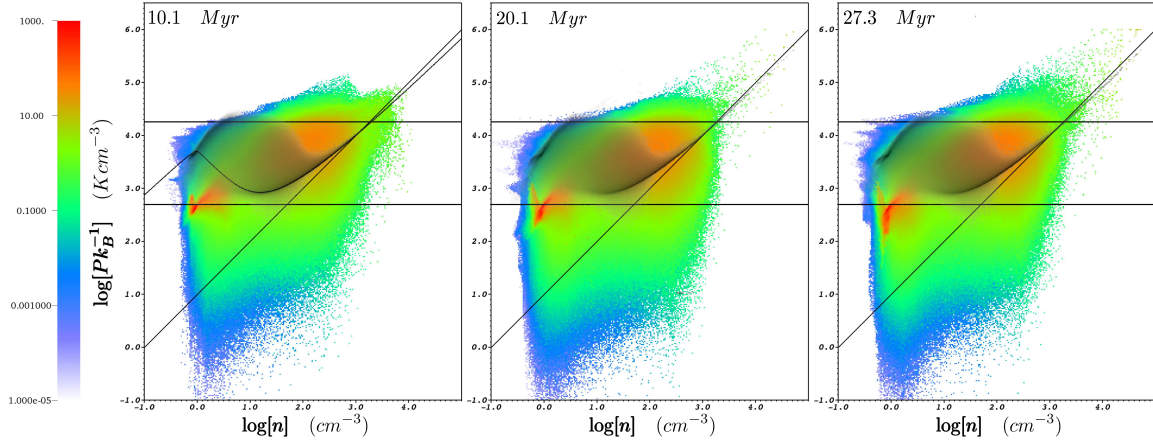


**Figure 4.13:** Pressure vs. density histograms for the  $\theta = 0^\circ$  case. The y-axis gives both the thermal (*grey scale distribution*) and magnetic (*color scale distribution*) pressure as a function of number density (the logs of these quantities, that is). The color bar gives the amount of mass at a given pressure and density. The thermodynamic equilibrium curve is given on the plot, as well as the initial magnetic pressure of the flows (*bottom horizontal line*), ram pressure of the flows (*top horizontal line*), and  $T = 10\text{ K}$  isotherm (*diagonal line*).

equilibrium curve. For a more detailed discussion of the dynamics relayed by the thermal pressure PDF, we refer the reader to previous work (e.g. Carroll-Nellenback et al., 2014). Presently, the focus will be on the *simultaneous* thermal and magnetic evolution of the gas, as shown by overlaying the  $P_{mag}, n$  PDF in color.

As can be seen in Fig. 4.13, *most* of the mass at low densities (i.e. near  $\log n = 0$ ) had  $\beta > 1$ , consistent with the notion of magnetic voids discussed in Section 4.7. This follows from comparing the  $P_{mag}$  distribution with the  $P_{therm}$  distribution at these densities. While the distribution of  $P_{mag}$  had a much higher spread, this spread was *mostly* below the  $P_{therm}$  distribution. In contrast, gas at higher densities ( $\log n > 2.5$ ) was mostly on top of the equilibrium curve, implying most of the densest gas had  $\beta < 1$ . This is in agreement with the densest gas having had enhanced magnetic support (and thus greater support against collapse), as was also discussed in Section 4.7. Despite

the spread in  $P_{mag}$  at these high  $n$ , the gas was entirely at  $T = 10K$ , as the  $P_{therm}$  distribution was constrained to lie on the equilibrium curve at these densities. Lastly, the  $P_{mag}, n$  PDF tended to shift toward the upper right of the plot while becoming more tightly distributed. If a line were drawn through the middle of the entire distribution, it would be roughly linear until about  $\log n \approx 1$ , and would then shift upwards, which on this log-log plot would correspond to a power law relationship similar to what is observed in other work (Heitsch et al., 2007; Hennebelle et al., 2008; Banerjee et al., 2009).

The dynamics attributable to these various features of the  $P_{mag}, n$  PDF can be seen as follows. As the simulation proceeded, turbulence at the collision interface (produced by the KH and NTS instabilities) generated magnetic field fluctuations. Reconnection diffusion, effective at removing excess magnetic energy from magnetized, turbulent flows (Lazarian et al., 2010; see also Klessen et al., 2000; Federrath et al., 2011), created the *large* (i.e. many orders of magnitude) spread in  $P_{mag}$  at low  $n$ . This spread in  $P_{mag}$  persisted as the gas was cooled and compressed. Flux-freezing, which accompanied this compression, then led to a sharp increase in  $P_{mag}$ , as seen by the rather large island of material (in red shading) up and to the right of the initial values. Note that colors correspond to a log scale, and so the amount of mass within this population was significantly greater than any other  $P_{mag}, n$  combination of the flow.

As time continued, a high  $P_{mag}, n$  ‘tail’ of the PDF formed that, 1) followed the equilibrium curve, 2) was above the ram pressure line of the flows, and 3) only appeared after protocusters had formed in the flow. Thus, this tail traced gravitational instability in the flow. Most of the mass in the tail was at a  $\beta < 1$ , consistent with the discussion from Section 4.7 that regions of high density were correlated with regions of high  $\beta^{-1}$ . Additionally, there was a spread in  $\beta$  for the population of gas parcels in this tail, as was also discussed in Section 4.7. In particular, protocusters formed in dense *enough* gas that was at lower average  $\beta^{-1}$  than the surroundings. Numerical reconnection within this high  $P_{mag}, n$  tail reduced the local field strength, thus enabling protocuster formation.

The PDFs for the  $\theta = 15^\circ$  case (Fig. 4.14) were similar to those for the  $\theta = 0^\circ$  case. The

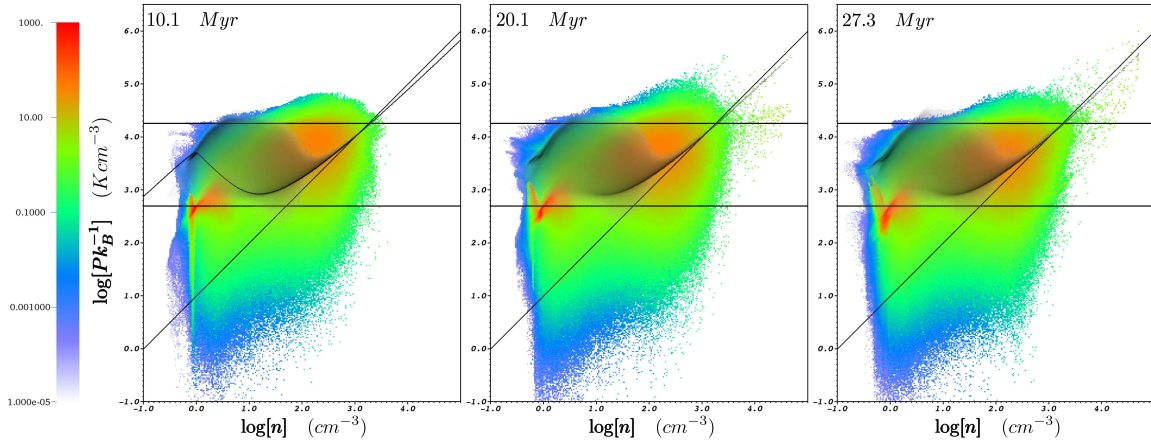


**Figure 4.14:** Pressure vs. density histograms for the  $\theta = 15^\circ$  case. As before, the y-axis gives both the thermal (*grey scale distribution*) and magnetic (*color scale distribution*) pressure as a function of number density (the logs of these quantities, that is). The color bar gives the amount of mass at a given pressure and density. The thermodynamic equilibrium curve is given on the plot, as well as the initial magnetic pressure of the flows (*bottom horizontal line*), ram pressure of the flows (*top horizontal line*), and  $T = 10\text{ K}$  isotherm (*diagonal line*).

largest difference was the delayed growth of the high  $P_{mag,n}$  tail in the higher shear run. Thus, the plot offers further evidence that shear suppressed compression in the flows. Eventually collapse was triggered in localized pockets of the flow, allowing gas parcels to begin to climb the equilibrium curve, as seen by  $t = 20.1\text{ Myr}$ . As in the previous case, this coincided with the presence of newly formed protoclusters in the flow.

Keeping in mind the trends discussed previously, Fig. 4.15 shows an even longer delay in collapse/compression in the highest shear angle case,  $\theta = 60^\circ$ . This is evident by the diminished upper-right island of high  $P_{mag,n}$  material early on. It is also shown by the greater delay in the high  $P_{mag,n}$  tail compared to the lower shear runs, which was still not visible by  $t = 27.3\text{ Myr}$ . Only by  $t = 32.8\text{ Myr}$  did the high  $P_{mag,n}$  tail emerge in the PDF, again corresponding with the presence of a newly formed protocluster in the flow.

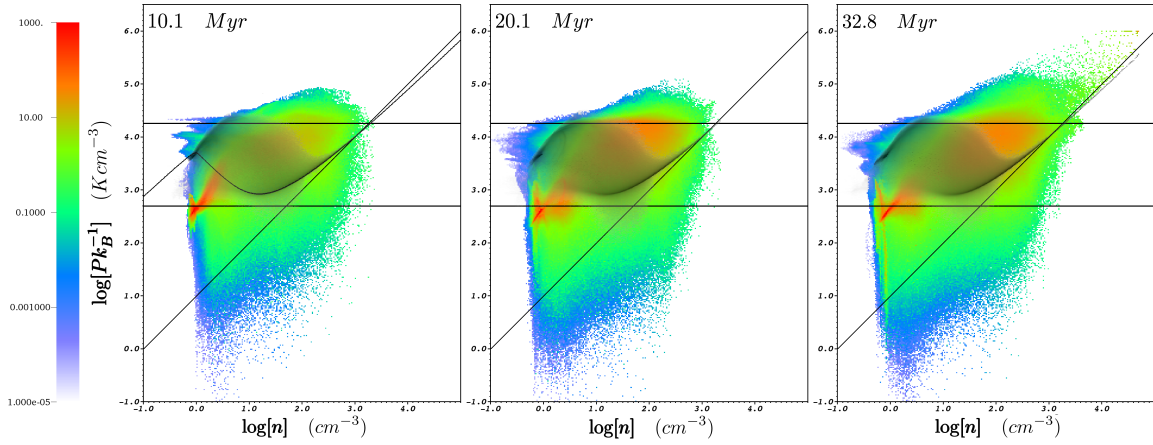


**Figure 4.15:** Pressure vs. density histograms for the  $\theta = 60^\circ$  case. As before, the y-axis gives both the thermal (*grey scale distribution*) and magnetic (*color scale distribution*) pressure as a function of number density (the logs of these quantities, that is). The color bar gives the amount of mass at a given pressure and density. The thermodynamic equilibrium curve is given on the plot, as well as the initial magnetic pressure of the flows (*bottom horizontal line*), ram pressure of the flows (*top horizontal line*), and  $T = 10\text{ K}$  isotherm (*diagonal line*). Note, the PDFs were similar enough between  $t = 20.1$  and  $27.3\text{ Myr}$  that we do not include the  $t = 27.3\text{ Myr}$  panel in the figure.

## 4.9 Energy Spectra

As insights into the energetics of the flow over different spatial scales cannot be drawn from the above thermodynamic analysis, let us now turn to power spectra of the gas in the collision region for kinetic, gravitational, and magnetic energies ( $E_{kin}$ ,  $E_{grav}$ , and  $E_{mag}$ , respectively), following Carroll-Nellenback et al. (2014). To accommodate steeper shear angles, the  $x$  dimension of the analysis region increased with  $\theta$ , and a  $10\text{ pc}$  buffer was added to either side. The dimensions of the analysis region for the different runs are given in Table 4.2.

Spectra for the different runs are shown in Fig. 4.16, for three different times. Note, the  $x$ -axes in the spectra are equivalent to  $\lambda_{max}\lambda^{-1}$ , where  $\lambda_{max}$  is given in Table 4.2. Thus, each unit on the  $x$ -axis represents that fraction of  $\lambda_{max}$ . A  $k^{-2}$  line (solid, red) is over-plotted to compare

**Table 4.2:** Analysis region for the different runs. Each were centered on the collision interface and had lengths in  $x$ ,  $y$ , and  $z$ , given by  $L_x$ ,  $L_y$ ,  $L_z$ . The maximum wavelength  $\lambda_{max}$  ( $\propto k_{min}^{-1}$ ) for each run is also given, which was equal to the longest dimension of the analysis region.

$\theta(^{\circ})$	$L_x$ (pc)	$L_y, L_z$ (pc)	$\lambda_{max}$ (pc)
0	20	40	40
15	31	40	40
60	90	40	90

with the spectra of  $v^2$  (dotted-dashed line, black) at  $t = 10.1$  Myr. The  $v^2$  spectrum is not included for other times, as it was largely unchanged throughout the course of the simulations.

As can be seen by the  $v^2$  spectrum, gas displayed the Burger’s turbulent spectrum ( $v^2 \propto k^{-2}$ ) in all of the runs over some range of  $k$ . For the  $\theta = 0^{\circ}$  case, this was  $3 < k k_{min}^{-1} < 40$ , corresponding to length scales of roughly  $13 \text{ pc} > \lambda > 1 \text{ pc}$ . At the low  $k$  end of the spectra, the driving scale of the turbulence is apparent and was on the order of the colliding flows radius ( $\lambda \approx 40 \text{ pc}$ ). At higher  $k$ , both dissipation and gravitational collapse limited the inertial range captured in the grid.

The dominant energy on all size scales for all of the runs was  $E_{kin}$  (smooth, black lines), and remained so throughout the course of the simulations. This was due to the power being generated in the colliding flows themselves. In the hydro version of the  $\theta = 0^{\circ}$  case (Carroll-Nellenback et al., 2014),  $E_{kin} > E_{grav}$  at late times in the flow on large scales ( $\lambda > 10 \text{ pc}$ ) was interpreted as a lack of global collapse. The much stronger suppression of  $E_{grav}$  (fine-dashed lines) in the present MHD runs (i.e.  $E_{kin} \gg E_{grav}$ ), supports that large-scale global collapse was not occurring. On the other hand, a marker of *local* collapse in the hydro run was that  $E_{kin} < E_{grav}$  on small scales ( $\lambda < 10 \text{ pc}$ ). That  $E_{kin} > E_{grav}$  on similar scales in the MHD cases further supports that magnetic fields have impaired local collapse: a diminished degree of local collapse occurred in the MHD runs, and only in regions where  $E_{grav} > E_{mag}$ .

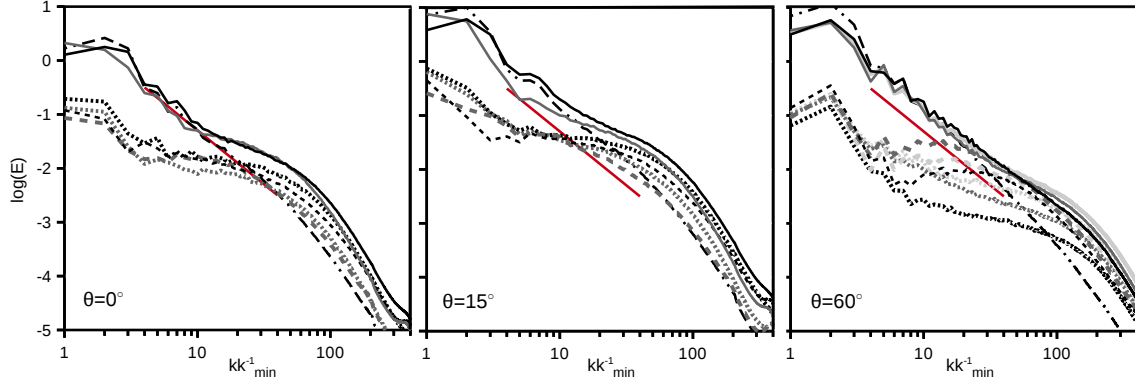


**Figure 4.16:** Energy spectra for the various runs. Shown are the kinetic (*smooth lines*), magnetic (*dashed*), and gravitational energies (*fine-dashed*) over time (increasing in time from dark to light). There is also a  $v^2$  line (*dotted-dashed line*) and corresponding  $k^{-2}$  line (*red line*) to measure the degree of Burger’s type turbulence in the runs. For the  $\theta = 0 - 15^\circ$  plots, black and gray lines are  $t = 10.1$  and  $27.3 \text{ Myr}$ , respectively. For the  $\theta = 60^\circ$  run, black, gray, and light gray lines are for  $t = 10.1$ ,  $20.1$ , and  $32.8 \text{ Myr}$ , respectively.

Indeed throughout the runs,  $E_{grav}$  was comparable to  $E_{mag}$ , on most scales. However, in the  $\theta = 0^\circ$  case,  $E_{grav}$  was generally higher than  $E_{mag}$  for  $10 < kk_{min}^{-1} < 100$ . Note, this corresponds to a length scale of  $.4 < \lambda \text{ (pc}^{-1}\text{)} < 4$ , which is the size scale of protoclusters. This is consistent with weak, localized collapse, due to a stronger gravitational field on these scales. By  $t = 27.3 \text{ Myr}$ , there was a slight increase in  $E_{mag}$  relative to  $E_{grav}$ , which may reflect an enhancement of the field due to compression from gravitational collapse.

The  $\theta = 15^\circ$  spectra show similar behavior to the  $\theta = 0^\circ$  case. At intermediate scales,  $E_{mag}$  and  $E_{grav}$  were comparable. At smaller scales, as gravitational collapse set-in,  $E_{grav} > E_{mag}$ . The effect of shear in this case did not make itself readily apparent in the energy spectra.

The spectra for the  $\theta = 60^\circ$  case, however, show clearly the effects of imposed shear on the distribution of energies at different scales. At  $10 \text{ Myr}$ ,  $E_{mag} > E_{grav}$ , on all size scales. In the range of  $9 < kk_{min}^{-1} < 90$ , corresponding now to size scales of  $1 < \lambda \text{ (pc}^{-1}\text{)} < 10$  (cf. Table 4.2), we see

$E_{mag} \gg E_{grav}$ , with  $E_{mag}$  approaching  $E_{kin}$  near  $kk_{min}^{-1} \sim 60$  ( $\lambda \sim 1.5$  pc). Note that this is the only run in which such an equipartition occurred. This enhanced  $E_{mag}$  relative to  $E_{kin}$  occurred with a simultaneous decrease in power of  $E_{grav}$  on all scales compared to the other runs. Thus, the signature of high shear was a relative amplification of the field on protocluster scales, as well as a decrease in  $E_{grav}$  on all scales, which is attributed to the disruption of dense structures forming in the flow as already discussed. Only by the end of the simulation ( $t = 32.8$  Myr) did  $E_{grav}$  become comparable with the energy locked up in the magnetic field (which was itself comparable to  $E_{kin}$ ). Thus, the spectra are consistent with the formation of a sink particle at late times.

## 4.10 Discussion

The focus of this chapter was on 3D, adaptive mesh refinement simulations of magnetized, shear colliding flows including self-gravity, sink particles, and cooling. Feedback was not included in the present work and thus these simulations only followed the formation and early evolution of molecular clouds. The simulations were of two colliding flows, intersecting at an inclined interface under a dynamically weak magnetic field. The inclined interface was used to generate shear at the collision layer, and was varied from not-inclined (normal incidence of the colliding flows) to highly inclined. As molecular clouds are unlikely to form from perfectly head-on collisions between two large-scale streams of gas, breaking the symmetry of the collision interface in this way was a previously unexplored next step in the colliding flows model exploration. The purpose of this set of experiments was to study the effect of shear on molecular cloud formation in magnetized colliding flows.

This work has shown that shear, imposed by an inclined collision interface, impacts cloud dynamics and reduces protocluster formation. In particular, as shear increased (i.e. the inclination angle steepened), *it took longer to form protoclusters, they formed in lower numbers, and they were lower in mass due to diminished accretion rates.* These effects are consistent with recent work by

Körtgen & Banerjee (2015), who found that higher degrees of inclination between colliding flows leads to a reduced number of sink particles, as well as a delay in their formation. Additionally, Chen & Ostriker (2014) show that under ideal MHD conditions, increasing the angle between upstream colliding flows and the magnetic field (which, with a change of reference frame is similar to our setup here) decreases the number of gravitationally bound cores that form in the post-shock region.

It was also shown that without shear, protocluster formation is greatly impeded in the presence of even a weak field ( $\beta = 10$ ,  $\beta_{ram} \approx 3.8$ ) alone. This was evidenced by the stark difference in protocluster number between the no-shear, MHD case ( $\theta = 0$ ) and the hydro version of this simulation in Carroll-Nellenback et al. (2014). More than 5 times as many protoclusters formed in the hydro run ( $n=27$ ) compared to the MHD run ( $n=4$ ). This result fits in with other colliding flows studies that have shown magnetic fields impair gravitational collapse. For instance, Hennebelle et al. (2008) shows that it takes longer to form self-gravitating objects in MHD colliding flows (aligned field,  $B_0 = 10 \mu G$ ), compared to flows without a field. Heitsch et al. (2009) also compared colliding flows with and without a magnetic field and found that the degree of post-shock turbulence decreases with a magnetic field. This led to a suppression of dense cores forming in the magnetized cases. Additionally, Vázquez-Semadeni et al. (2011) found that increasing the magnetic field strength in colliding flows simulations decreases the SFE of forming clouds.

To understand the flow dynamics responsible for the weaker protocluster formation, the distinction between 'global' and 'local' collapse was emphasized, and it was shown that collapse in the simulations was due to *localized* regions becoming unstable, rather than the entire collision region. Indicators of local collapse included the positions of sink particles *away* from the global potential minimum, weak mass 'fall-back' into the collision region, and power spectra that showed  $E_{kin} > E_{grav}$  on large scales, but  $E_{kin} < E_{grav}$  on small scales (Carroll-Nellenback et al., 2014). The above presented results are consistent with these indicators: sinks formed away from the center of the collision region, they had variable accretion rates, and both  $E_{grav}$  and  $E_{mag}$  were  $\ll E_{kin}$  on large scales, but  $E_{grav} \sim E_{kin} > E_{mag}$  on small scales. All of the runs ( $\theta = 0 - 60^\circ$ ), as well as

the hydro run, exhibited local collapse *only* (i.e. did not collapse globally).

Compared to the hydro run, collapse was weakened in the  $\theta = 0^\circ$  case due to the interplay between the turbulent post-shock velocity field and the magnetic field. Turbulence in the interaction region introduced distortions to the magnetic field, which produced regions of local field amplification. These were shown to be co-located with regions of high density (Sections 4.7 and 4.8). Thus, local collapse had an additional form of support in the MHD case(s) – magnetic support, due to field amplification, consistent with previous work (Banerjee et al., 2009; Heitsch et al., 2009)). Over time, numerical reconnection would have reduced the field strength in these pockets of dense gas (Lazarian et al., 2010; Vázquez-Semadeni et al., 2011; Federrath et al., 2011; Chen & Ostriker, 2014), thereby allowing highly localized regions to become magnetically super-critical and produce protoclusters (should the gas also be Jeans unstable).

As shear increased in the flows, a higher degree of post-shock turbulent velocity resulted. This disrupted the formation of dense structures in the flow, which further inhibited local collapse and protocluster formation (by locally decreasing the M2FR, as well as, increasing the Jeans length). This seemed to be the dominant effect of shear, as the stronger shear field was not found to necessarily lead to greater field amplification. The reasons for this were likely two-fold. First, while the shear generated by the oblique shocks at the collision interface would have led to greater distortions of the field (Hartmann, 2001; Heitsch et al., 2007; Chen & Ostriker, 2014), they were also likely shorted out faster in the higher shear cases. Additionally, given the disruption of high density structures forming in the flow, regions of increased field strength due to flux freezing would have also been diminished. Both the PDFs and spectra (Sections 4.8 and 4.9, respectively) support the conclusion that field amplification did not increase with shear. They do, however, show decreases in high density structures. This is consistent with Körtgen & Banerjee (2015), who attribute declining sink particle formation to shear disrupting the formation of high density structures.

Lastly, we discussed the large-scale realignment of the collision interface that took place in our highest shear angle case,  $\theta = 60^\circ$ . This unexpected result may have arisen from the orientation

of an NTSI node with respect to the oncoming flows, as discussed in Section 4.6. However, tension in the magnetic field may have also contributed to the realignment. A realignment of the collision interface was also mentioned in Körtgen & Banerjee (2015).

## 4.11 Appendix

### 4.11.1 Magnetized Ring Model

To make calculations simplest, let us envision the following scenario. At  $t = 0$ , the magnetic field is  $\vec{B} = B_0 \hat{x}$  for  $r > R$ , where  $R$  is the colliding flows radius. For  $r < R$ , we take  $B = 0$ . This is a fine approximation, given the field is dynamically weak within the flows (recall,  $\beta_{ram} \approx 3.8$ ). As material enters the collision region, it is shocked and then expands away from the collision region, as described above. We can approximate this expansion as being spherically symmetric.

Now, the ram pressure of the ejecta pushes outward on the surrounding low density, magnetized ambient medium. In 2D, this leads to a ‘ring’ of flux that moves outward (in 3D, a spherical ‘shell’; Fig. 4.17). This ring has two boundaries, an outer radius,  $r_o$ , and an inner radius,  $r_i$  (Fig. 4.17, *bottom panel*). Once this ring comes to steady state, the magnetic pressure at  $r_o$  will be balanced by the unperturbed, ambient magnetic pressure,  $P_{mag}$ , which is  $\propto B_0^2$ . At  $r_i$ ,  $P_{mag}$  will be balanced by the ram pressure of the ejecta. A reasonable approximation for this ram pressure is the pre-shock ram pressure, given the low Mach of the flows. Note, we will ignore edge effects near the colliding flows themselves, and instead focus on the dynamics of the ring *perpendicular* to the flows (Fig. 4.17, *top panel*).

Assuming the magnetic field is the dominant force in the ambient (therefore, ignoring gravity and pressure forces), the steady-state ideal MHD momentum equation for the ring is given by

$$\nabla \frac{B^2}{2\mu} = \frac{B^2}{\mu r} \hat{\mathbf{n}} \quad (4.10)$$

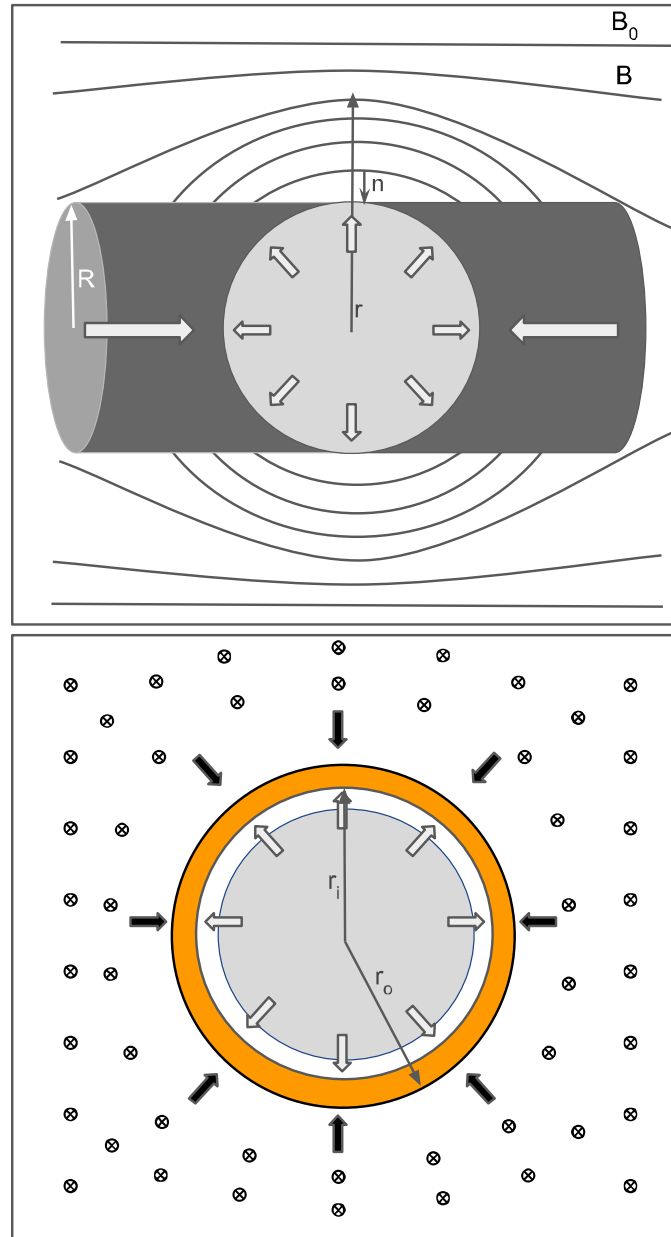


**Figure 4.17:** Diagram of the magnetic ring model. *Top panel* shows the incoming flows, spherical post-shock expansion region and corresponding magnetic field arcs, and the direction along which we are integrating the momentum equation ( $r$ ). Also given is the unperturbed field value ( $B_0$ ), the cylindrical radius of the colliding flows ( $R$ ), and the normal unit vector ( $\hat{n}$ ) discussed in the text. *Bottom panel* shows the ring of high density material (in the mid-plane of the flows) with inner radius  $r_i$  and outer radius  $r_o$ .

where  $\mu$  is the magnetic permeability,  $r$  is the radius of curvature, which is taken to just be the distance from the center of the colliding flows to a position in the ring, and  $\hat{\mathbf{n}}$  is a unit vector normal to the field line that is anti-parallel to  $r$  (i.e.  $\hat{\mathbf{n}} = -\hat{\mathbf{r}}$ ). Defining the radius of curvature in this way is equivalent to assuming the field is being bent along *spherical* arcs. Equation 4.10 says that in steady state, the magnetic tension of the curved field lines (RHS) is balanced by the gradient in magnetic pressure (LHS). Projecting Eqn. 4.10 onto the  $r$ -axis and integrating gives the following expression for  $B^2(r)$  in the ring,

$$B^2 = B_0^2 \left(\frac{r_o}{r}\right)^2. \quad (4.11)$$

Using this and balancing the magnetic and ram pressures at the ring's inner radius  $r_i$ , we have

$$\frac{B_0^2}{2\mu_0} \left(\frac{r_o}{r_i}\right)^2 = \rho v^2 \left(\frac{R}{r_i}\right)^2, \quad (4.12)$$

which reduces to

$$r_o = \sqrt{\beta_{ram}} R. \quad (4.13)$$

Now, the inner radius is where ejected material is being decelerated. To estimate this edge of the ring for comparison with the simulations, let us use flux-freezing. Equating the flux in the ring at steady state,

$$\theta_1 = \int_{r_i}^{r_o} \frac{B_0 r_o}{r} 2\pi r dr = 2\pi B_0 r_o (r_o - r_i), \quad (4.14)$$

to the flux in the ring initially

$$\theta_2 = \int_R^{r_o} B_0 2\pi r dr = \pi B_0 (r_o^2 - R^2), \quad (4.15)$$

gives

$$r_i = \frac{r_o^2 + R^2}{2r_o}. \quad (4.16)$$

Plugging in for  $r_o$  (Eqn. 4.13) yields

$$r_i = R \frac{(\beta_{ram} + 1)}{\sqrt{4\beta_{ram}}}, \quad (4.17)$$

which is approximately

$$\boxed{r_i \approx \frac{1}{2} \sqrt{\beta_{ram}} R} \quad (4.18)$$

or  $r \approx 3R$ . As seen from the left-hand panel of Fig. 4.6, this simple model reproduces the ring's position to within a factor of two.

## Chapter 5

# The Formation of Prestellar Filaments by MHD Shock Processes

### 5.1 Introduction

Filaments (elongated, high-density structures) are ubiquitous to star forming regions. Many have been found to contain young protostellar cores (André et al., 2010; Arzoumanian et al., 2011; Polychroni, 2012; Lee et al., 2014), and thus, are considered some of the earliest structures of star formation. The formation of filaments is still an open-ended question. Observations indicate that they might be tied to colliding flows: measurements of velocity gradients perpendicular to filaments (Kirk et al., 2013; Fernández-López et al., 2014) have been interpreted as arising from infall onto the filaments (i.e. converging accretion flows).

It has also been observed in recent years that the interstellar magnetic field lies normal to filaments in many cases, as shown by dust polarization maps, which measure the plane-of-sky

component of the magnetic field (Goodman et al., 1992; Chapman et al., 2011; Planck Collaboration et al., 2016). Moreover, both the magnetic field and local velocity gradient seem to be aligned with local ‘striations’ to the filaments, those lower density contrast structures that are themselves normal to filaments (think spine and intersecting vertebrae, Palmeirim et al., 2013). Together, it appears that gas may be converging onto filaments, *along* magnetic fields.

A third interesting property of filaments is that fluid motions seem to change direction *inside* of them, so that the gas flows *along* filaments, internally (Kirk et al., 2013; Fernández-López et al., 2014). Given that the uncertainty of dust polarization measurements increases with density (Goodman et al., 1992), the field might actually change direction to become parallel inside of filaments as well. Indeed, if the internal field *did not* become more or less parallel to the filament, external field lines would be bent away from normal due to drag between internal fluid motions and the field (as shown in panel 4A, Fig. 5.1).

The gas motions and accompanying magnetic field geometry associated with filaments have primarily been attributed to magneto-gravitational instability. In this conceptualization, an overdense region within a molecular cloud first becomes Jeans unstable (panel 1A, Fig. 5.1). Collapse is triggered and proceeds *along* magnetic field lines, as the gas is not yet magnetically supercritical (panel 2A). Once enough mass accumulates for the region to become magnetically supercritical, gas can begin to fall in perpendicular to the field, as well. For magnetically supercritical filaments, this means collapse would then proceed *along* the filament (panel 3A; Pon et al., 2011; Pon et al., 2012; Toalá et al., 2012). At this point, the field would become distorted as it is dragged down into the collapsing gas (panel 4A). That the magnetic field strength increases with density in collapsed gas (i.e.  $B \propto n$ ,  $n > 1000 \text{ cm}^{-3}$ ; Troland & Heiles, 1986; Crutcher, 1999; Crutcher et al., 2010; Tritsis et al., 2015) has commonly been cited as evidence for this scenario.

An alternative explanation that does not require beginning with a Jeans unstable mass is the reorientation of oblique magnetized shocks. This model begins with the collision of marginally supersonic gas along magnetic field lines (i.e. the path of least resistance). As was shown in the

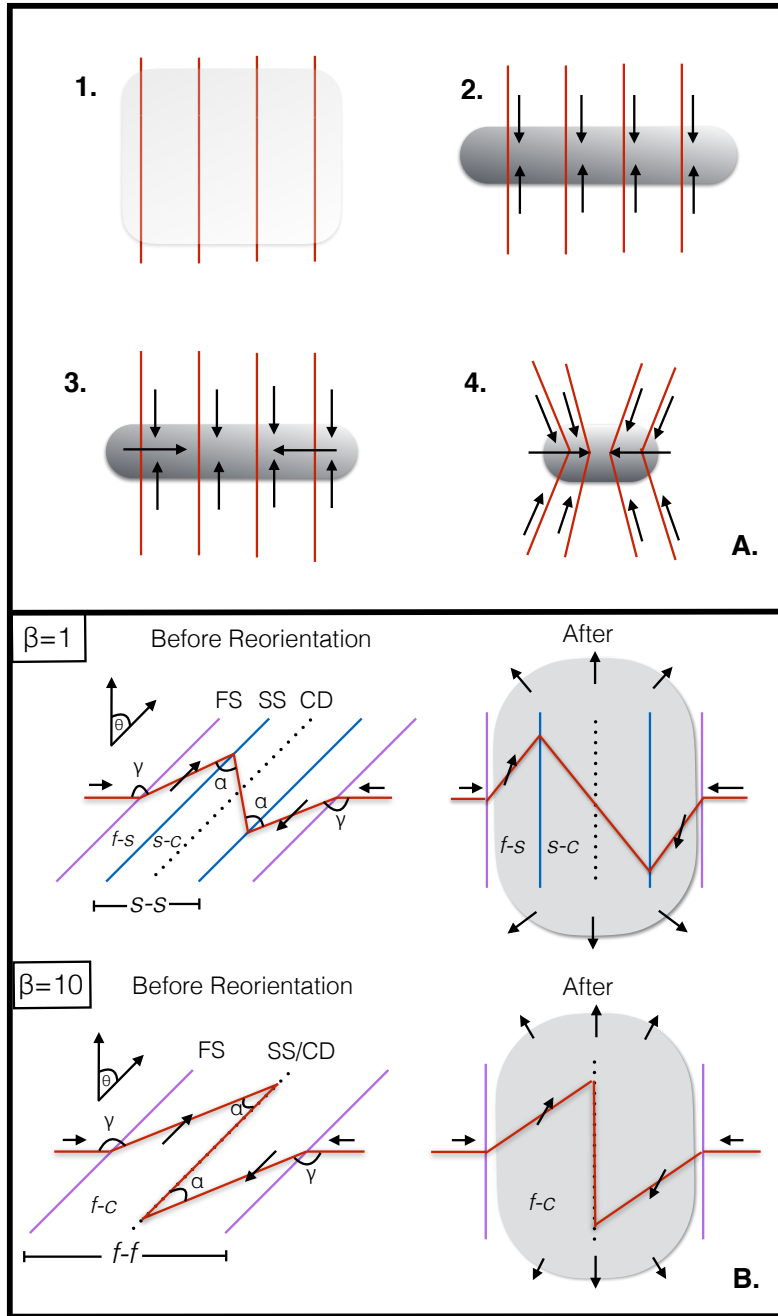


**Figure 5.1:** Mechanisms for generating filaments normal to magnetic field lines. *Top Panel.* Magneto-gravitational collapse. Jeans unstable gas will initially collapse along field lines (1-2). Once enough mass accumulates in the resultant filament, mass can flow along the filament and drag magnetic field lines inward (3-4). *Bottom Panel.* Reorientation of magnetized oblique shocks. Uppercase letters denote wave modes, and lowercase letters give regions (see text). Flow direction is given by the black arrows, and a representative magnetic field line is shown in red. The left and right panels give the initial and reoriented structures, respectively. The top and bottom rows give the moderate ( $\beta = 1$ ) and weak field ( $\beta = 10$ ) cases of this paper. The grey shaded region represents the growing filament.

preceding chapter, in the most general case, where the flows meet at a non-normal interface, the central shock layer appears to readjust so that it becomes normal to the upstream field (and oncoming flows). This effect is also consistent with observed filament gas motions and field morphology (i.e. perpendicular external fluid motions and field lines, as well as parallel internal fluid motions). Moreover, distortion of field lines by passage through colliding flows shocks (cf. Chen & Ostriker, 2014) also produces a power law relationship of the magnetic field strength with density (Heitsch et al., 2007; Hennebelle et al., 2008; Banerjee et al., 2009), consistent with the observations described above.

To orient the reader, a schematic of the reorientation process is illustrated in the bottom panel of Figure 5.1. For the moderately magnetized cases of this chapter (those runs that have a  $\beta = 1$ , where  $\beta$  is the ratio of the thermal to magnetic pressure), supersonic inflows that meet at an oblique angle ( $\theta$ ) generate both an MHD fast shock ( $FS$ ) and slow shock ( $SS$ ) on either side of a contact discontinuity ( $CD$ ; Fig. 5.1B, top/left). Between the  $FS$  and  $SS$  (region  $f - s$ ), gas that moves parallel to the shock front (note the flow direction is given by the black arrows) drags magnetic field lines *away* from the shock normal, whereas in region  $s - s$ , field lines bend *toward* the normal as they connect across the  $CD$ . Over time, the entire post-shock region reorients (right panel), where the grey-shaded region represents the growing filament. As will be shown, this process depends heavily on the lateral ejection of material away from the growing filament into the ambient medium (represented by the outward directed arrows, right hand column), which occurs due to pressure gradients between the post-shock gas and the ambient medium. The result is similar when the magnetic field is weakened ( $\beta = 10$ , Fig. 5.1B, bottom), notwithstanding the slight changes to the shock structure. That is, reorientation produces a post-shock flow and field that has parallel components to the filament, internally (in regions  $f - s$  and  $f - c$ , in the  $\beta = 1$  and  $\beta = 10$  cases, respectively), and perpendicular components, externally. This MHD shock process is the topic of the present chapter.

A suite of 2D magnetized, colliding flows simulations are presented in this chapter that test

the effects of varying the magnetic field strength and the inclination angle of the collision interface on reorientation. Reorientation is found to be possible in all but the strongest magnetic field cases, resulting in post-shock filaments<sup>1</sup> that approach a normal orientation with respect to the upstream velocity and magnetic field. In addition, it will be shown that fluid motions generated by this model are highly parallel to the filament within the shock bounded gas, and the resultant structures naturally assume an s-shaped geometry, reminiscent of the integral-shaped filament (Bally et al., 1987; Johnstone & Bally, 1999).

This chapter is organized as follows. Section 5.2 presents a description of the numerical model, Section 5.3 discusses 1D shock solutions relevant to the present work, and Section 5.4 presents the key results. This chapter concludes with a discussion in Section 5.5, and a resolution study of the results in the appendix.

## 5.2 Methods

### 5.2.1 Numerical Model and Simulation Parameters

The suite of simulations consist of two sets of runs. The first was a pair of shock models that reviewed the wave solutions across *infinite* hydrodynamic (hydro) and magnetohydrodynamic oblique shocks, using an exact Riemann solver and HLLD solver, respectively. The shocks were generated by marginally supersonic flows ( $M = 1.5$ , where  $M$  is the mach number) that collided at an oblique interface, similar to the set up in Chapter 4. These flows were injected along the  $x$  boundaries of a 2D grid so that they completely filled the domain (Fig. 5.2, top panel). Boundary conditions in  $y$  were set to periodic. The obliquity of the collision interface was given by the inclination angle,  $\theta$ , and was fixed at  $\theta = 30^\circ$ . While these runs were performed on a 2D mesh, the fluid variables varied only along the  $x$ -dimension. Thus, these runs provide the wave solutions across 1D oblique shocks.

---

<sup>1</sup>In 2D, the result is actually the generation of perpendicular *sheets*. Only in 3D could true filaments form. The basic MHD shock physics described here in 2D, however, can be extrapolated to 3D. Fogerty et al. (2016) showed that fully 3D simulations also exhibited reorientation.

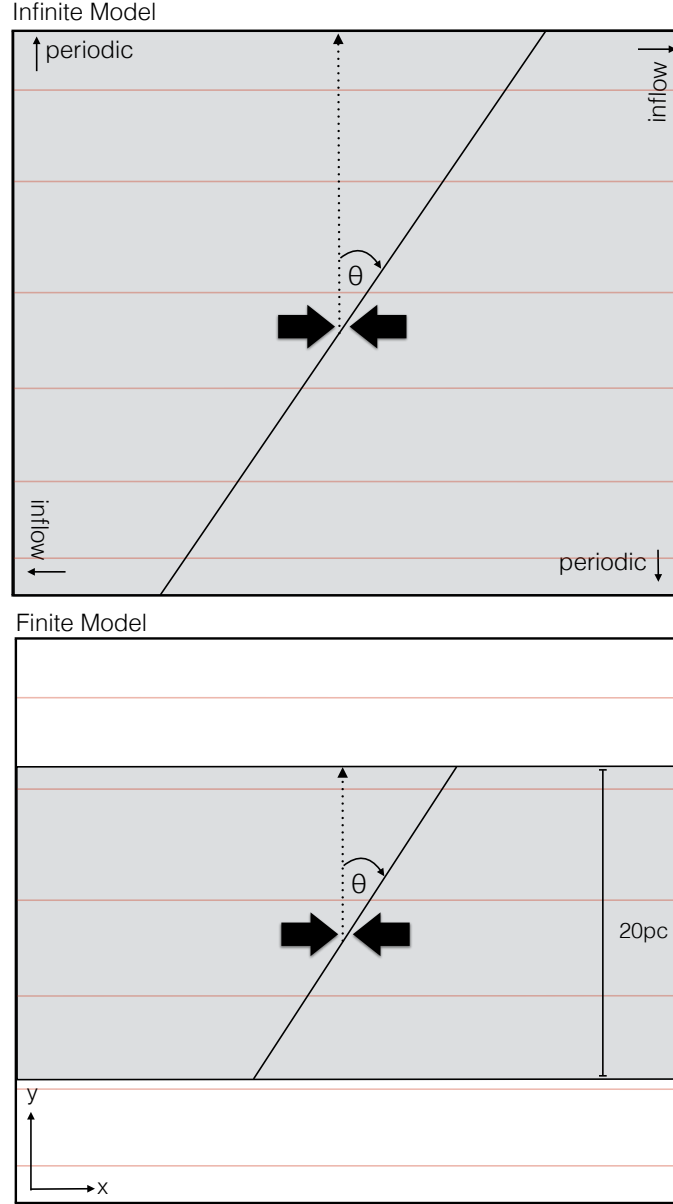


**Figure 5.2:** Model diagrams. *Top panel.* Setup for the infinite cases. Incoming flows meet at an effectively infinite oblique shock, defined by the angle  $\theta$ . Boundary conditions of the different box sides are labeled. Magnetic field lines are represented by the red lines, and the flow is uniform everywhere along the collision interface, in the direction given by the thick black arrows. *Bottom panel.* Setup for the finite cases. The colliding flows are now embedded in a stationary ambient medium of the same density and pressure. The flows are 20 pc in diameter and collide at an oblique collision interface, given by  $\theta$ . The uniform magnetic field is again given by the red lines, and runs everywhere parallel to the flows.

Geometry	Hydro/MHD	$\beta$	$\theta$ ( $^\circ$ )	Domain Length (pc)	Resolution	AMR levels
Infinite <sup>†</sup>	Hydro	...	30	1	$256^2$	0
Infinite <sup>†</sup>	MHD	1	30	1	$256^2$	0
Finite	MHD	.1	30	160	$256^2$	2
Finite	MHD	1	30	160	$256^2$	2
Finite	MHD	10	30	160	$256^2$	2
Finite	MHD	.1	60	160	$256^2$	2
Finite	MHD	1	60	320	$512^2$	2
Finite	MHD	10	60	320	$512^2$	2

**Table 5.1:** Suite of simulations.<sup>†</sup>Did not include cooling.

The second set of runs was a parameter study of 2D *finite* magnetized colliding flows. In these runs, the flows were embedded in a stationary ambient medium of the same density and pressure (Fig. 5.2, bottom panel). The flows were again marginally supersonic ( $M = 1.5$ ), and collided at an oblique interface, given by the inclination angle  $\theta$ . The inclination angle of the finite runs varied between  $\theta = 30^\circ$  and  $60^\circ$ . The complete suite of simulations is given in Table 5.1.

Self-gravity was not included in the present suite of simulations. Consequently, the simulations neglected gravitational collapse along filaments. The runs instead tracked the formation and early evolution of filaments, while illustrating the basic mechanism of reorientation. Cooling was included in all of the finite colliding flows runs, following a modified Inoue & Inutsuka (2008) cooling curve that allowed the gas to cool to  $T = 10$  K. The infinite cases did not include cooling, but instead used an adiabatic equation of state with  $\gamma = 5/3$ .

The parameters of each of the runs were chosen to match ideal ISM conditions (as discussed in the preceding chapter). Thus, the runs were initialized at a uniform number density of  $n = 1$   $\text{cm}^{-3}$  and temperature of  $T = 4931$  K. At these densities and temperatures, the gas was initially in thermal equilibrium (for those runs that included cooling). The speed of each inflow was  $v = 11$   $\text{km s}^{-1}$ .

For those runs that included a magnetic field (cf. Table 5.1), the field was uniform throughout the simulation domain and ran parallel to the flows. The strength of the field was set by  $\beta$ . In the 1D MHD case,  $\beta = 1$ . For the finite colliding flows runs,  $\beta$  ranged between  $\beta = 10 - .1$ . This is equivalent to a field strength of  $B = 1.6 - 16 \mu G$ , in line with current measurements of the global mean field of the ISM ( $B \approx 1 - 10 \mu G$ , Beck, 2001; Heiles & Troland, 2005).

The infinite colliding flows runs had periodic boundary conditions in  $y$  and inflow boundary conditions in  $x$ . The length of the square 2D domain was 1  $pc$  on a side. The mesh was a fixed-grid at a resolution of  $256^2$  and had a cell size of  $\Delta x = .0039 pc$ . For the finite colliding flows runs, the size of the square domain was chosen to be large enough so that no gas or magnetic field lines left the box over the course of the simulation (cf. Table 5.1). However, the effective resolution was held constant at a finest cell size of  $\Delta x_{min} = .15625 pc$ . Boundary conditions were set to inflow where the flows were injected, and extrapolating everywhere else. The radius of the finite colliding flows was  $r = 10 pc$ . The final simulation time for the finite runs was  $t_{sim} = 12 Myr$ . The infinite cases were shorter at  $t_{sim} = 1 Myr$ , the time it took for the shocks to reach the edge of the simulation domain.

### 5.3 Infinite Adiabatic Oblique Shocks

Before presenting the reorientation simulations, let us briefly review the hydro and MHD shock solutions generated by infinite, adiabatic colliding flows. The results of this section provide a framework for evaluating the shocks presented in later sections. Given this section is just a review of 1D oblique shocks, the reader can feel free to jump ahead to the main results in Section 5.4.

#### 5.3.1 Hydro Case

The hydro Riemann problem relevant to the present paper consists of a constant density and pressure fluid that is separated by a discontinuous jump in velocity. In particular, the velocity field converges

on the central Riemann interface at an oblique incidence. Note, the inclination angle of the interface for both the infinite hydro and MHD run (discussed below) was chosen to be  $\theta = 30^\circ$ , to match the finite  $\theta = 30^\circ$  runs of Section 5.4.

As can be seen in Figure 5.3, this Riemann problem generates two oblique shocks that are separated by a contact discontinuity. In addition to the characteristic density increase across each shock front, the top panel of Figure 5.3 shows that velocity vectors bend away from the shock normal across each shock. This occurs because only perpendicular components of upstream velocity vectors ( $v_\perp$ ) change across shocks. This leads to  $v_\perp \rightarrow 0$  in the downstream gas. Note, if  $v_\perp \neq 0$  in the post-shock gas, additional waves would be generated behind the shocks, which would violate the three-wave solution family of hydrodynamic Riemann problems. Thus, post-shock gas flows *exactly* parallel to each shock front. In other words, *oblique shocks generate shear*. The various fluid variables across the wave modes are given in the bottom panel of Figure 5.3.

### 5.3.2 MHD Case

The addition of a uniform magnetic field that is parallel to the flows modifies the shock structure just described. For this case, *two* oblique shocks are generated on either side of the contact discontinuity (Fig. 5.4). Given Alfvén modes cannot be generated in 1D, the forward-most shock can be identified with the MHD fast shock ( $FS$ ), which is trailed by the slow shock ( $SS$ ). As before, incoming velocity vectors are deflected away from the shock normal across the outer,  $FS$  (Fig. 5.4). However, now these redirected velocity vectors encounter the magnetic field. The collision between the flow and the field causes the field to also bend away from the shock normal across the  $FS$ , as the field and fluid are perfectly coupled in ideal MHD. The result is an amplification of the field across the  $FS$ , visible by both the color of the field lines, which increase in strength from white to red (Fig. 5.4, top panel), as well as the amplification of the parallel field component ( $B_{//}$ ) across the  $FS$  (bottom panel). Given the field is tied across the contact discontinuity ( $CD$ ), it eventually must turn back toward the shock normal. This gives rise to the inner,  $SS$ , where the field again switches direction.

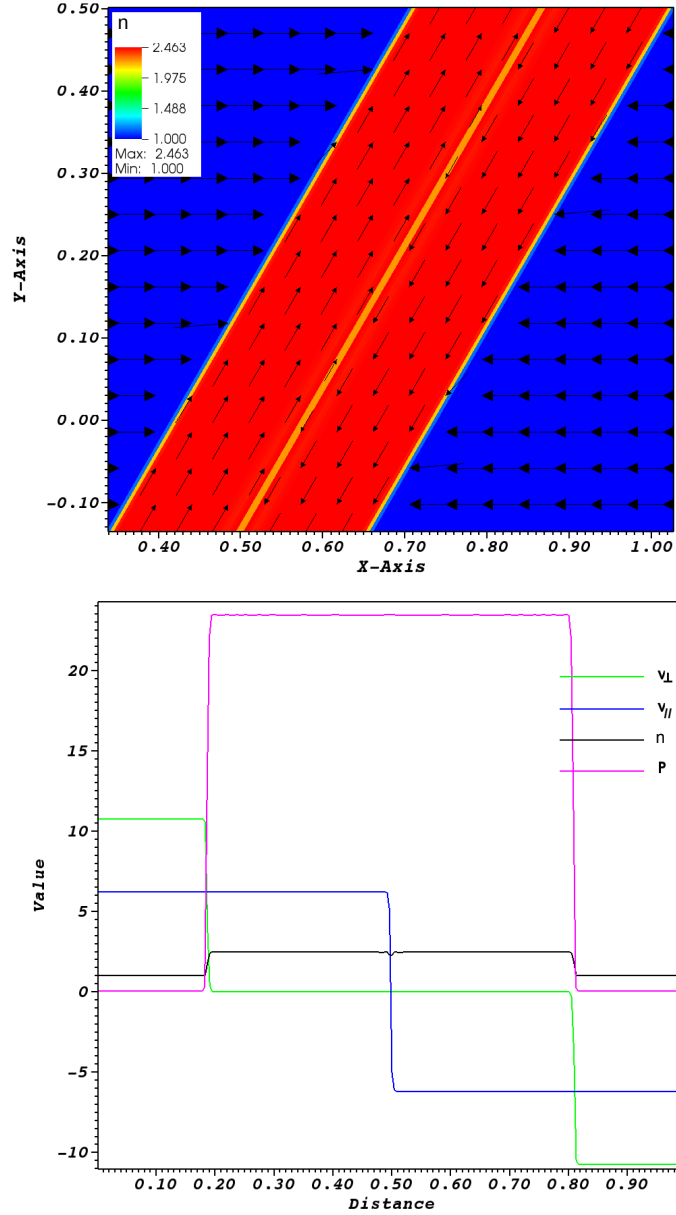


**Figure 5.3:** The fluid variables across hydrodynamic, oblique shocks. *Top panel* shows number density of the infinite hydrodynamic Riemann problem described in text. Velocity vectors are overlaid and scaled by magnitude. *Bottom panel* gives the various fluid variables across the waves. Perpendicular and parallel components of velocity ( $v_{\perp}$  and  $v_{\parallel}$ , respectively) are in units of  $km\ s^{-1}$ , number density in  $cm^{-3}$ , and pressure ( $P$ ) in  $K\ cm^{-3}$ . Note, pressure has been scaled to fit on the  $y$ -axis, where  $P = (P - 4931) \times 10^{-3}$ .

However, in contrast to the  $FS$ , gas that passes the  $SS$  is stagnated. This is visible by zero velocity gas motions in the region  $s - s$  (defined in Fig. 5.1, bottom panel). Lastly, note that reorientation fundamentally cannot occur in 1D, given the symmetry in the initial conditions.

## 5.4 Finite Oblique Shocks, with Cooling

To address the issue of reorientation, let us now turn to simulations of finite, magnetized colliding flows. This section differs from the last in that the flows are now embedded in a stationary ambient medium. This section begins with the effects of varying  $\beta$  and  $\theta$  on the morphology of reoriented flows. Then, the temporal evolution of each case is presented, again focusing on morphological changes over the course of the simulations.

### 5.4.1 The Effects of Varying $\beta$ and $\theta$ on Reorientation

In the finite colliding flows scenario, post-shock motions no longer strictly adhere to the shear flow predicted by the infinite shock solutions of Section 5.3. Pressure gradients now exist between post-shock gas and the external ambient medium, which forces material laterally outwards, away from the collision region. Given reorientation does not occur in the infinite case, this lateral motion is a key component of reorientation. This is illustrated by the fact that reorientation does not occur when material is *prevented* from leaving the collision region, as in the strong field ( $\beta = .1$ ) cases. Plots of number density show that when  $\beta = .1$ , for inclination angles of either  $\theta = 30^\circ$  or  $60^\circ$ , magnetic field lines are strong enough to resist ejection of material from the collision region (Fig. 5.5, top panel). Any material that does manage to escape the collision region travels parallel to the colliding flows, along the field lines, and is deposited in the ‘trailing arms’ of the filament – a prominent feature of finite, oblique, magnetized colliding flows (see red circles in Fig. 5.5, top-left panel). Indeed, the field is so strong in these cases that a post-shock shear flow is also inhibited, as the field effectively resists motion perpendicular to it. Instead, post-shock material is delivered

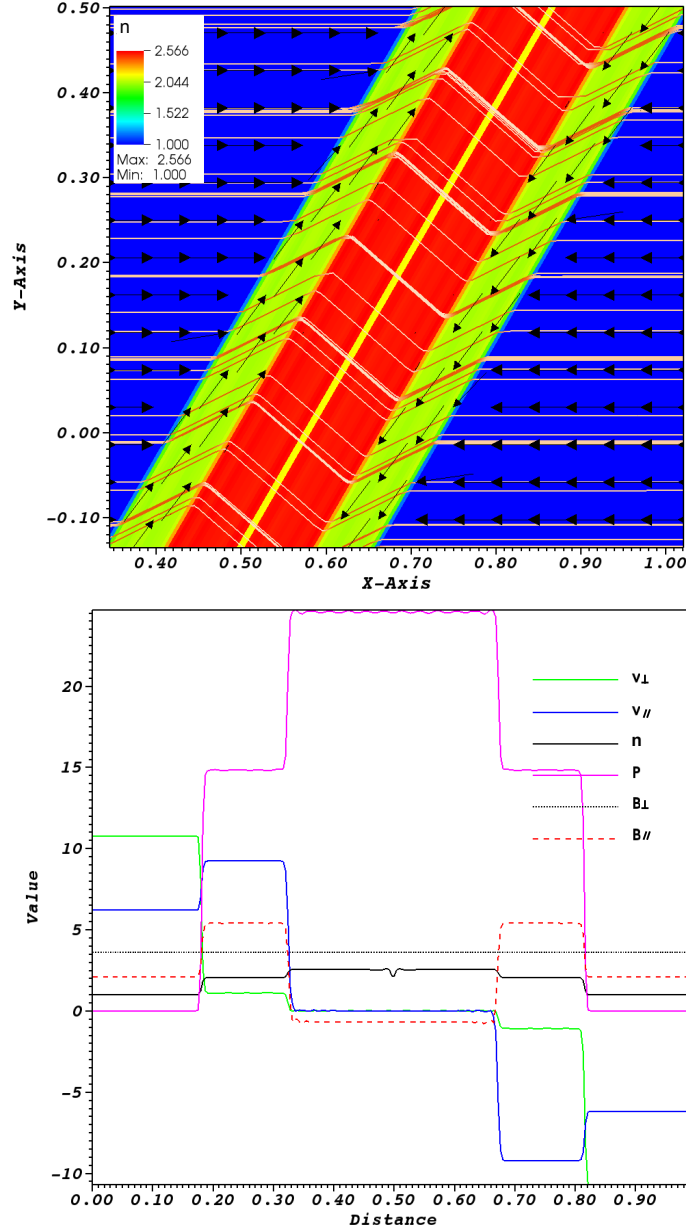


**Figure 5.4:** The fluid variables across MHD, oblique shocks. *Top panel* shows number density of the infinite MHD Riemann problem described in text. Field lines increase in strength from white to red, and velocity vectors are scaled by magnitude. *Bottom panel* gives the fluid variables across the waves. Units are the same as in Figure 5.3, with the addition of the perpendicular and parallel magnetic field components ( $B_{\perp}$  and  $B_{\parallel}$ , respectively), given in  $\mu G$ .

directly onto the growing filament, where it continues to collect, cool, and compress over the course of the simulation. This results in a smooth and flat filament, as turbulent sub-structure (induced from the thermal instability, e.g.) is also effectively inhibited.

The behavior begins to change as the magnetic field is weakened. When  $\beta$  is increased to 1, the  $\theta = 30^\circ$  case exhibits a large-scale reorientation. This is illustrated in Figure 5.5 (middle row, left panel), where we see an initially inclined filament has reoriented to become more or less normal to the oncoming flows by  $t = 12 \text{ Myr}$ . As in the infinite version of this case, an outer shock layer forms that diverts incoming flows either diagonally ‘up’ or ‘down’, depending on the upstream interface orientation (cf. Section 5.3.2). However, across the second, inner shock (region  $s - s$ ), gas is falling onto the long axis of the filament, along magnetic field lines. This is in contrast to the infinite case, where fluid motions were absent in this region, and thus, these motions are arising from cooling. The result is the formation of a post-shock flow that has parallel components to the filament in both the  $f - s$  and  $s - c$  regions.

Near the top and bottom of the filament (i.e. near the flow/ambient boundary), and across the  $CD$ , the velocity vectors become aligned so that they are pointing along  $y$ , out into the ambient medium. That is, the flow switches from being a shear flow across the  $FS$ , to being directed outwards into the ambient medium in the entire  $f - f$  region (near the flow/ambient boundary). This is due to pressure gradients between the collision region and the ambient medium. The ejection of material from the over-pressurized collision region into the ambient medium drives arcs in the magnetic field, whose tension impedes further lateral flow and traps the ejected gas (see the appendix in Chapter 4 for an analytical description of this process). This trapped gas travels along the magnetic field line arcs, as shown by the corresponding velocity vectors in Figure 5.5, where it collects in the trailing arms. This three-step process, namely, 1) post-shock ejection from the collision region into the ambient medium, 2) the bending of the magnetic field lines into arcs, and 3) the redirection of incoming flows along the arcs to collect in the trailing arms of the filament, produces an ‘s-shaped’ filamentary structure.

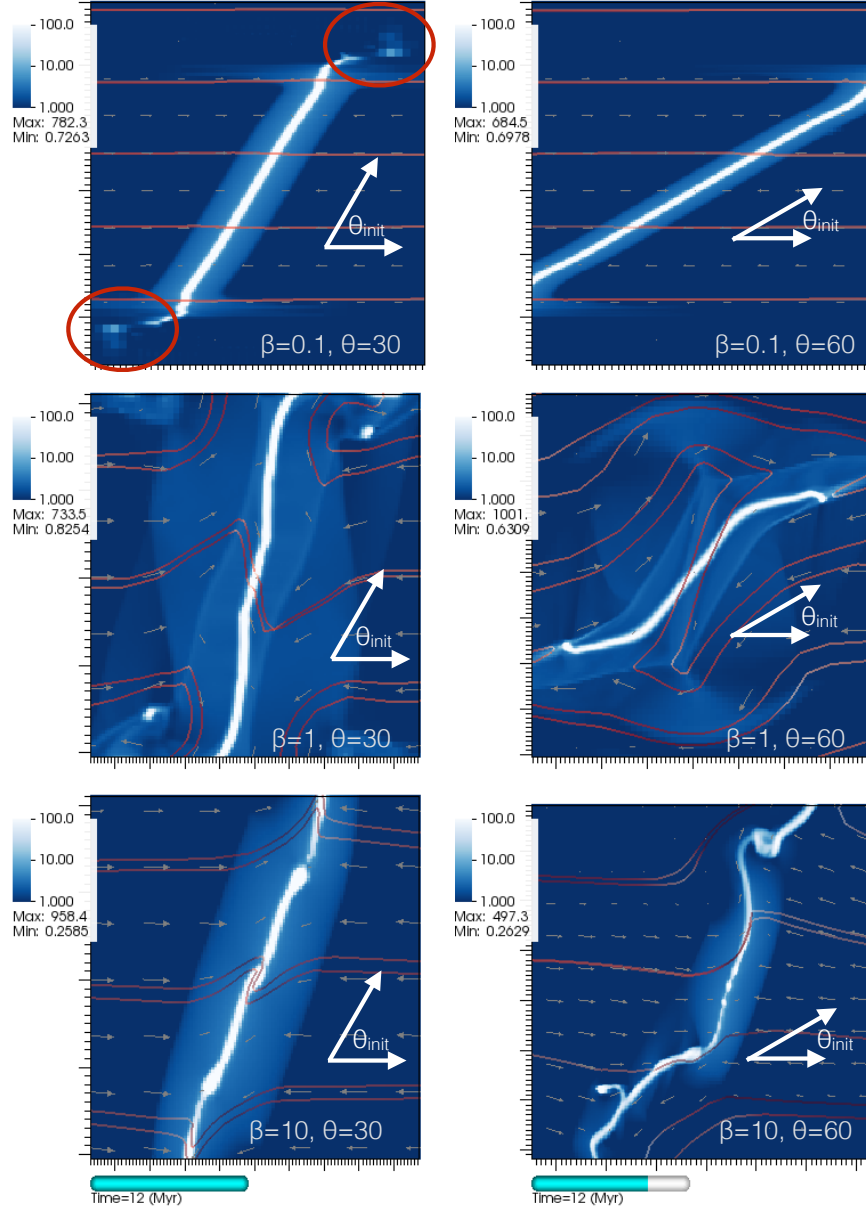


**Figure 5.5:** Density plots of the six finite colliding flows runs, with overlaid velocity vectors and magnetic field lines. Each plot shows the flows at the final simulation time of 12 *Myr*. The legend gives number density in units of  $cm^{-3}$ . Vectors are scaled by magnitude, and field lines increase in strength from white to dark red. The initial inclination angle of the collision interface is given by  $\theta_{init}$ . The trailing arms of the filament (discussed in text) are illustrated by the red circles in the upper-left panel. The location of these trailing arms extend beyond the plot boundaries for the weaker field cases.

As the inclination angle is steepened to  $60^\circ$  for the  $\beta = 1$  case, the same trends develop. Namely, material is deflected away from the shock normal across the  $FS$ , ejected from the collision region into the ambient medium, and an s-shaped filament forms with a similar degree of reorientation by  $t = 12 \text{ Myr}$ . While the higher obliquity shocks of this run produces weaker post-shock compression and thus a wider  $f - s$  region, changing the inclination angle does not appear to drastically alter the degree of reorientation for the moderate field,  $\beta = 1$  cases.

As the field is weakened further in the  $\beta = 10$  runs, the  $30^\circ$  case reorients to a similar degree, but reorientation is enhanced in the  $60^\circ$  case (Fig. 5.5, bottom row). Slightly different filamentary structures are also visible, as there are no longer slow shocks present in the filaments. This means that by  $\beta = 10$ , the shock solutions have effectively approached the 1D hydro solutions (away from the flow/ambient boundary), as they must, in the limit of weak magnetic field. Furthermore, there are no longer  $s - s$  regions (marked by a stagnate velocity field), where material can expand away from the collision region due to pressure gradients alone. Instead, incoming gas is quickly shunted away from the collision region as it passes through the single oblique shock on either side of the  $CD$ . As this material leaves the collision region, it drags magnetic field lines away with it. As the plots show, the weaker field is dragged to further distances, and thus the trailing arms extend farther away into the ambient medium from the main filament body (beyond the plot boundaries).

### 5.4.2 Temporal Evolution of the Flows

Let us now turn to the temporal evolution of the flows. This section will again be focusing on density plots with overlaid velocity vectors and magnetic field lines, beginning with the stronger field ( $\beta = 1$ ) cases.

Figure 5.6 shows the evolution of the  $\beta = 1$ ,  $\theta = 30^\circ$  case. As can be seen in the  $t = .55 \text{ Myr}$  panel, the bulk properties of the flow are similar to the infinite MHD case (Section 5.3.2), at early times. That is, a shear flow is established across the outer,  $FS$ , and negligible fluid motions occur inside of region  $s - s$ . Over time, post-shock cooling triggers inflow along the field lines onto the

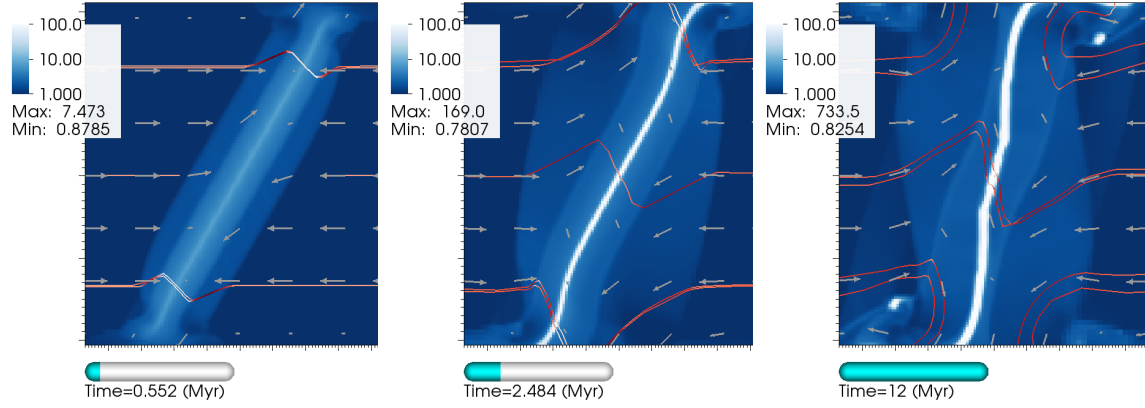


**Figure 5.6:** Temporal evolution of the  $\beta = 1$ ,  $\theta = 30^\circ$  case. All units are the same as in Figure 5.5.

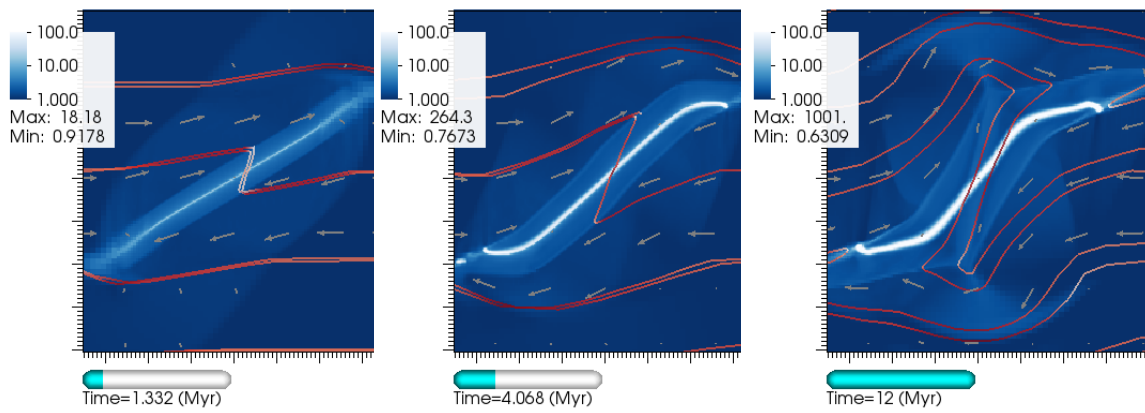


**Figure 5.7:** Temporal evolution of the  $\beta = 1$ ,  $\theta = 60^\circ$  case. All units are the same as in Figure 5.5.

$CD$  of the forming filament ( $t = 2.5 \text{ Myr}$ ). Additionally, this time panel shows that the fast shocks stall (near the top flow/ambient boundary for the right  $FS$ , and near the bottom for the left  $FS$ ). This is due to a decrease in thermal pressure support behind the shocks as material escapes into the lower pressure ambient medium. The result of these stalled shock fronts is the reorientation of the outer shock layers, as those regions that are not stalled continue to propagate away from the collision region. This leads to the outer shock layers becoming normal to the oncoming flows.

As can be seen in the figure (and even better in the animations online<sup>2</sup>), reorientation of the inner shock layer (i.e. region  $s - s$ ) also begins with the lateral ejection of material from the collision region. That is, reorientation occurs from the *outside-in* – beginning near the flow/ambient boundary, and moving toward the colliding flows axis by  $t = 12 \text{ Myr}$ . This occurs as material is delivered along the ‘z-shaped’ magnetic field lines near the colliding-flows axis nearly vertically onto the long axis of the filament. When the inclination angle is steepened to  $\theta = 60^\circ$ , for the same value of  $\beta = 1$ , the evolution is qualitatively similar (Fig. 5.7).

As the field is weakened to  $\beta = 10$ , the largest difference that occurs in the evolution is the appearance of a vacated inner region along the filament’s long axis (FLA) as material preferentially collects around the top and bottom of the filament (i.e. near the flow/ambient boundary), as well as just exterior to the FLA (see Figures 5.8 and 5.9, middle panels). This arises from the extreme amplification of the field along the  $CD$  as field lines are stretched by the shear flow (recall, the color of the field lines increases from white to dark red with increasing field strength). By the last time panel, in both the  $\theta = 30^\circ$  and  $60^\circ$  cases, gas has successfully collapsed onto the FLA, and the internal high density regions of the filament have begun to reorient, again from the outside-in. Within the region  $f - f$ , the flow and the field are highly parallel to the filament, and the entire structure (filament+trailing arms) has assumed an s-shaped geometry.

While this overall evolution is the same between the two  $\beta = 10$  cases, the external flow field

---

<sup>2</sup>See the following youtube channel: <https://www.youtube.com/channel/UCEmUg0BdCyPC3QnKdNDJq1w>

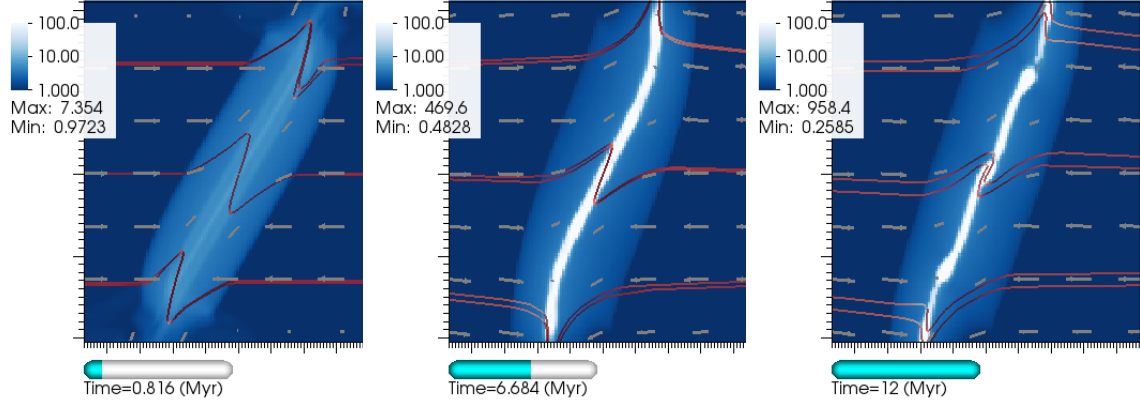


**Figure 5.8:** Temporal evolution of the  $\beta = 10$ ,  $\theta = 30^\circ$  case. All units are the same as in Figure 5.5.

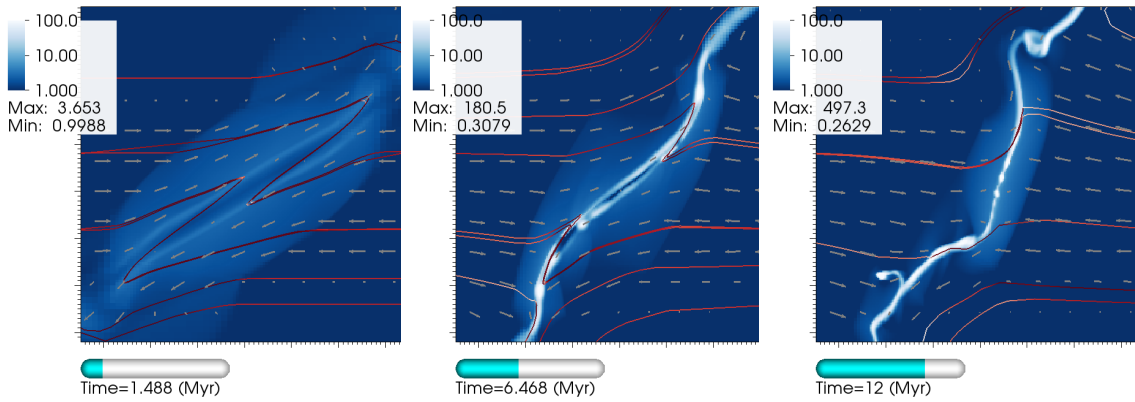


**Figure 5.9:** Temporal evolution of the  $\beta = 10$ ,  $\theta = 60^\circ$  case. All units are the same as in Figure 5.5.

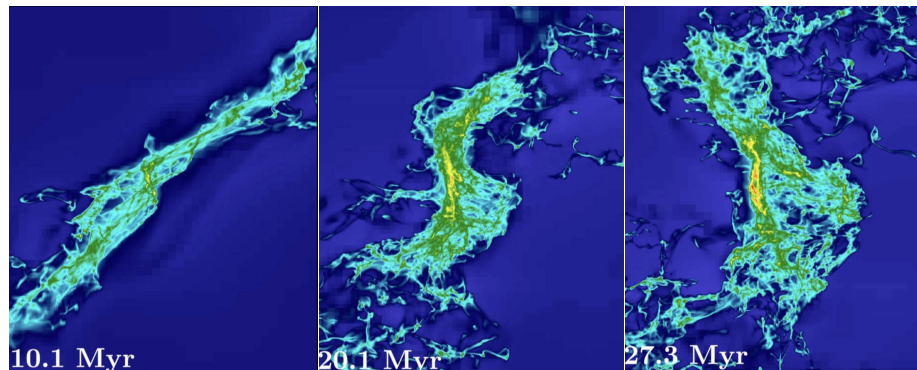


**Figure 5.10:** Evolution of the 3D  $\beta = 10$ ,  $\theta = 60^\circ$  case, with self-gravity. Image taken from Fogerty et al. (2016). The colors represent column density, and increase from blue to red. See Fogerty et al. (2016) for details.

in the  $\theta = 60^\circ$  case at  $t = 12 \text{ Myr}$  is unlike any of the other runs. Velocity vectors show that material entering from the left is directed downwards as it approaches the filament, and that material entering from the right is directed upwards. Note, this is the *opposite* flow pattern that the oblique shocks establish alone (see earlier time panels), indicating that the flow is traveling along bowed magnetic field lines. Such an asymmetric flow is necessary to generate a torque on the filament. This could explain why the  $\beta = 10$ ,  $\theta = 60^\circ$  case reorients more than the  $\beta = 1$ ,  $\theta = 60^\circ$  case (see also Fig. 5.11).

## 5.5 Discussion

The focus of this chapter has been on addressing a previously unexplored mechanism capable of producing filaments normal to magnetic fields: namely the reorientation of finite MHD, oblique shocks formed between colliding flows. This process was identified previously in fully 3D simulations of magnetized colliding flows that included turbulence, self-gravity, cooling, and oblique shocks at

the collision interface (Fogerty et al., 2016). As discussed in Chapter 4, that work revealed a large-scale reorientation of molecular gas, which had occurred for a highly oblique run (Fig. 5.10). Reorientation of the collision interface of 3D, magnetized, oblique colliding flows was also recently reported by Körtgen & Banerjee (2015). Running the simulations in 2D, without gravity, supports that the mechanism of reorientation is robust. Moreover, that hydro simulations of oblique colliding flows do not exhibit reorientation (both in 2D, as well as 3D, Haig et al., 2012; Haig & Heitsch, in prep), indicates that magnetic fields play a crucial role in the process.

As shown, reorientation begins with the lateral ejection of material away from the post-shock collision region between colliding flows. Without magnetic fields, ejecta would continue to push out into the ambient medium until its ram pressure came into balance with the thermal pressure of the environment. With magnetic fields, this material is funneled back down along bowed magnetic field lines, toward the colliding flows surface. This produces ‘trailing arms’ of the filament. Additionally, escaped gas from the collision region into the ambient medium translates into a loss of post-shock pressure support, resulting in stalled outer shocks. This led to the reorientation of the outer shocks, which *is* also seen in hydro. The difference lies in the reorientation of the densest regions of the filament (i.e. along the  $CD$  of the collision region), which does *not* occur without the magnetic field. Instead, the shear flow setup across hydro oblique shocks generates instabilities (i.e. KH modes) along the interface. These instabilities in turn produce a ‘stair-casing’ structure, but not a coherent filament that reorients (Haig et al., 2012). Hennebelle (2013) showed that in order to build a coherent filament in a shear flow, a magnetic field must be present.

The role of the magnetic field in reorienting the internal layers of the filament is the delivery of material along ‘z-shaped’ magnetic field lines within the collision zone, near the colliding flows axis (red box, Fig. 5.11, left panel). Note, these field lines have not been ‘blown-out’ into arcs from the lateral post-shock ejection (as seen in the yellow box of Fig. 5.11, left panel), and thus deliver material nearly vertically onto the growing filament. Thus, reorientation begins with the lateral escape of gas from the collision region, and moves toward the center of the collision region

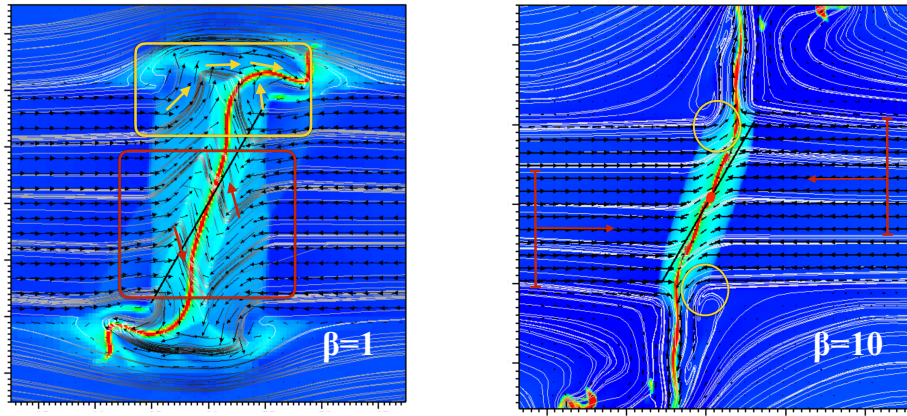


**Figure 5.11:** Potential reorientation mechanisms for finite, oblique, MHD colliding flows. *Left panel* shows the dominant mechanism of reorientation for the  $\beta = 1$  cases. Bowed field lines near the flow/ambient boundaries (e.g. yellow box) deliver material away from the collision region onto the trailing arms, whereas ‘z-shaped’ field lines nearer the colliding flows axis (red box) deliver material directly onto the filament. This differential delivery results in an outside-in reorientation of the filament. *Right panel* shows that in the weaker field cases, material escapes from the collision region asymmetrically across the  $CD$ . In regions marked by yellow circles, the post-shock shear flow is *enhanced* as material flows out of the collision region along the flow/ambient pressure gradient. In contrast, for oppositely directed material across the shock layer, this pressure gradient now *counteracts* the shear flow. The result is a mismatch of incoming  $x$ -momentum onto the filament (red, barred arrows) and a torque in the direction of reorientation.

over time. As the magnetic field is weakened, torque on the collision region may play an additional role in the reorientation process. As we have seen, the  $\beta = 10$ ,  $\theta = 60^\circ$  case reoriented to a greater extent than the stronger field  $\beta = 1$ ,  $\theta = 60^\circ$  case, and this coincided with a large-scale asymmetric flow onto the filament. The mismatch in incoming  $x$ -momenta onto the filament can be seen in the right-hand panel of Figure 5.11, which illustrates the effect for the smaller inclination angle case,  $\beta = 10$ ,  $\theta = 30^\circ$ . As the figure shows, there is an asymmetric loss of material from the collision region across the  $CD$  in the weak field cases (yellow circles), which could lead to a net torque being generated by the bounded flow that remains (red arrows).

Lastly, it was demonstrated that reorientation produces structures that are reminiscent of those found in nearby star-forming regions. Namely, it was shown that under realistic ISM magnetic field strengths, reorientation generates filaments perpendicular to their background magnetic fields, as well as exhibit velocity motions that switch from being perpendicular externally to parallel internally. These features are consistent with observations of prestellar filaments (Kirk et al., 2013; Palmeirim et al., 2013; Fernández-López et al., 2014; Planck Collaboration et al., 2016). Additionally, we have shown that filaments formed via finite, magnetized oblique shocks naturally assume an s-shaped geometry.

## 5.6 Appendix: Resolution Study

A short resolution study of the  $\beta = 10$ ,  $\theta = 60^\circ$  case was conducted, which shows that increasing the resolution to a minimum cell size of 0.02 pc (3 additional AMR levels), *does not change the reorientation behavior of the MHD oblique shock layer*. As Figure 5.12 shows, however, a couple of differences are present at higher resolution. First, the internal structure of the filament appears to not be fully resolved in the present paper: a low-density, internal layer of the filament is present at higher resolution (Fig. 5.12, middle and right panels). Note, this structure is present early-on, at lower resolution (c.f. leftmost panels of Figures 5.8 & 5.9). This suggests that numerical diffusion diminishes magnetic pressure in this region in the lower resolution runs, thereby allowing material to cool and condense onto the axis. Indeed, as the resolution increases, the total magnetic energy in the simulations continues to increase as well (for  $t > 2.4 \text{ Myr}$ , Fig. 13), as post-shock compressions result in magnetic field amplification.

Second, the small-scale structure that develops in the post-shock flow has not converged at the resolution of the present paper. These results are consistent with Koyama & Inutsuka (2004), who show that thermal instability-induced fragmentation converges (in 1D) only when 1) the Field Length,  $\lambda_F = (\kappa T / \rho^2 \Lambda)^{1/2}$ , where  $\kappa$  is the coefficient of thermal conductivity and  $\Lambda$  is the cooling

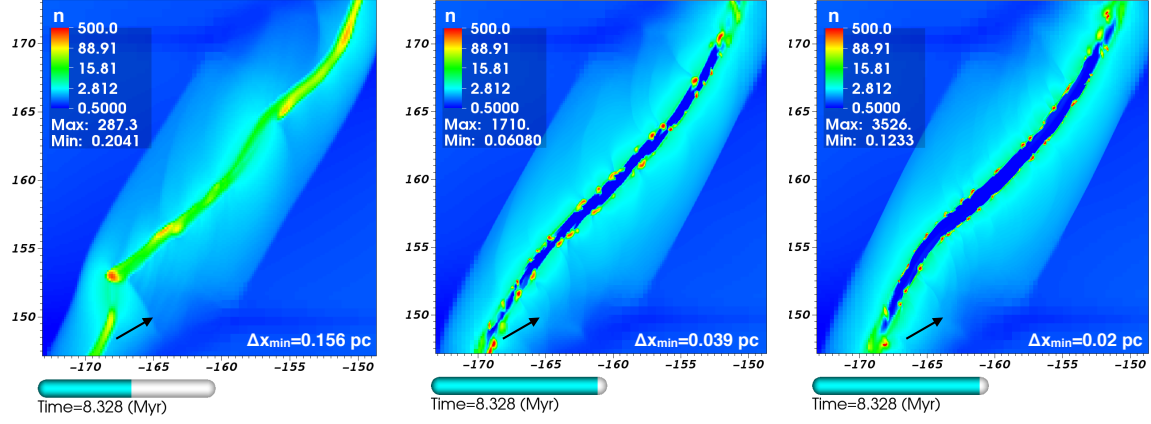


**Figure 5.12:** Resolution study of the  $\beta = 10$ ,  $\theta = 60^\circ$  case. The three panels show a zoom-in of the collision region of this finite case at 8.3 *Myr* for three test resolutions:  $\Delta X_{min} = 0.156$ , 0.039, and 0.02 *pc*. The leftmost panel is the resolution of the current paper. The color legend corresponds to number density ( $cm^{-3}$ ), and the black arrow shows the initial orientation of the shock layer.

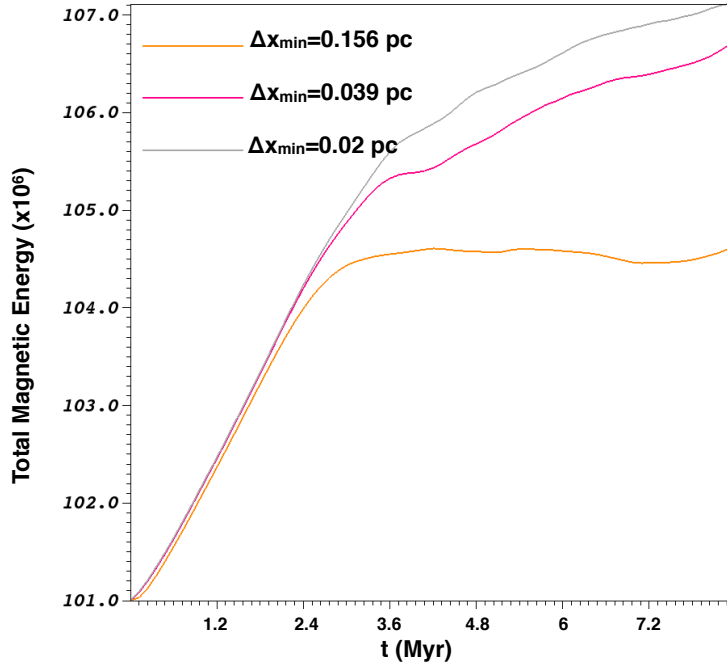


**Figure 5.13:** Total scaled magnetic energy over time for three different resolutions. Note that at higher resolutions, the amplification of the field by post-shock compression continues beyond  $t > 2.4$  *Myr*, where it tapers off at the resolution of the present paper.

rate of thermally unstable gas (Field, 1965), is resolved by at least 3 zones, and 2) thermal conduction is included in the simulations. Along the collision interface, and away from the flow boundaries, the present suite of finite simulations are effectively 1D (at early times). However, since thermal conduction is ignored in the present work, artificial growth of small-scale modes of the TI is expected, seeded by numerical noise on the grid scale. This explains the formation of increasingly smaller-scale ‘clumplets’ in the post-shock flow with increasing resolution.

Taken together, a direct comparison of the simulation results to filaments in the ISM is not possible. However, the intention of this work was to shed light on a potential MHD shock mechanism associated with oblique colliding flows, rather than investigate the detailed characteristics of filaments formed by this mechanism. Moreover, since the present suite of runs are 2D, the detailed structure of the filaments are artificially idealized from the outset (clearly evident when comparing the rightmost panel in Fig. 5.12 with its 3D counterpart: Fig. 5.10). The results of this resolution study support that the reorientation mechanism is a large-scale phenomenon, and that it is sufficiently resolved in the present paper.

## Chapter 6

# Summary and Future Directions

### 6.1 Summary

Star formation is a ‘multiscale, multiphysics’ phenomenon (Chapter 1). This dissertation has explored a range of processes associated with star formation, from molecular cloud formation and evolution, to protostellar collapse. In particular, this thesis has focused on characterizing the governing magnetohydrodynamical, gravitational, and shock dynamical processes within three phases of the gas: molecular clouds, filaments, and protostellar cores.

To carry out this research, the state-of-the-art, Eulerian, adaptive mesh refinement code, AstroBEAR, was used (Chapter 2). In addition to solving the conservative equations of hydrodynamics on a Cartesian grid, AstroBEAR contains a wide range of multiphysics capabilities. The simulations here presented included magnetic fields, self-gravity, heating and cooling processes following a parameterized cooling curve appropriate for the the ISM, and sink particles. Feedback was not included in the present work, and so this research largely emphasizes early evolutionary periods of star forming regions.

The main findings from this dissertation are summarized below. Additionally, a series of modifications have been made to AstroBEAR which facilitate future studies aimed at ‘closing the

loop’ of the doctoral research via the addition of feedback. Thus, a discussion of future directions will be presented at the end of this chapter, thereby concluding this thesis.

### 6.1.1 Molecular Cloud Formation and Dynamics in High-Shear, Magnetized Environments

To explore how molecular clouds form and evolve in high-shear, magnetized environments, a series of magnetized, oblique ‘colliding flows’ simulations were conducted (Chapter 4). Instead of forcing turbulence, the colliding flows model naturally generates turbulent molecular clouds through the excitation of various fluid instabilities in the post-shock region between the flows. The density, temperature, magnetic field strength, and speed of the flows were chosen to match standard ISM values. Over the course of  $27 \text{ Myr}$  in the simulations, a dense network of filamentary molecular clouds form, akin to those seen in observations (Fig. 6.1). Within the filaments of these molecular clouds lie protocluster clumps (Fig. 6.2). Each generated cloud complex was  $\sim 40 \text{ pc}$  across on its long axis,  $\sim 10 \text{ pc}$  across its short axis, and resolved to  $0.05 \text{ pc}$ .

Star formation within the generated molecular clouds was greatly impeded by magnetic fields, relative to hydrodynamic models. This was attributed to field line compression occurring within localized regions of collapsing gas, which would supply an additional source of support (increased magnetic pressure) against gravity. Indeed, 2D histograms of the gas showed that the magnetic pressure within the generated molecular clouds increased with gas density, consistent with this interpretation.

As the shear within molecular clouds increased, so did the magnetic energy (relative to the gravitational and kinetic energy), and this was correlated with further decreases in the star formation activity. These results indicate that shear suppresses star formation within molecular clouds not only due to increased transverse kinetic motions, but also due to enhanced magnetic field amplification relative to models without shear. In order for star formation to eventually proceed in each of the

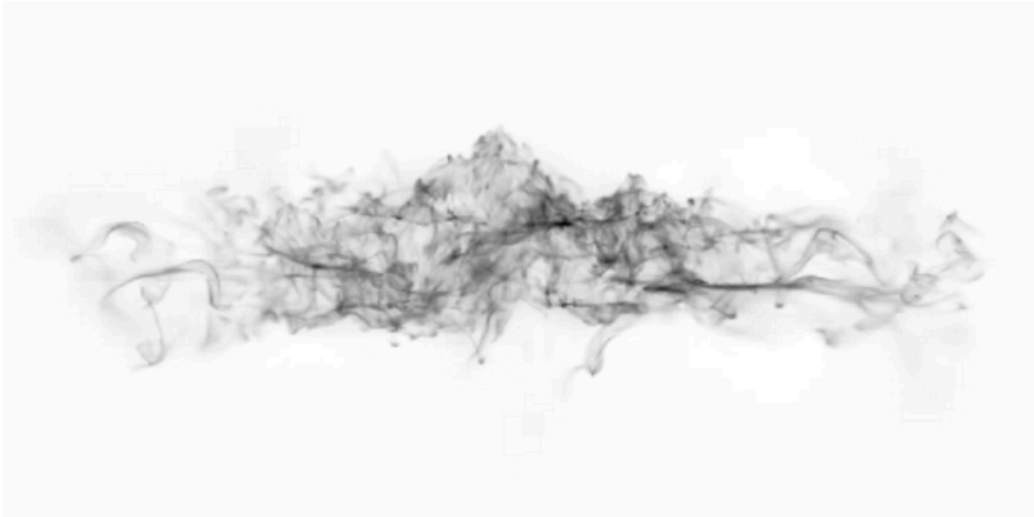


**Figure 6.1:** Column density map of a molecular cloud formed via magnetized, sheared colliding flows. A variety of fluid instabilities produce rich, filamentary substructure.

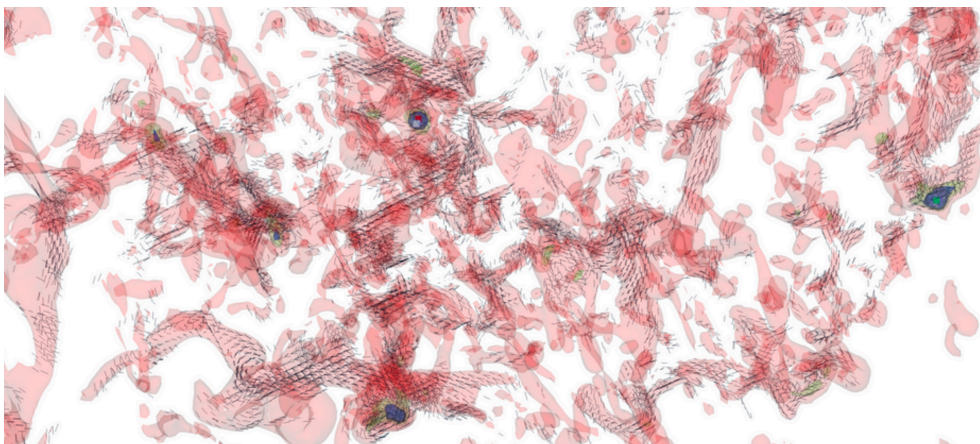


**Figure 6.2:** Density isocontours of molecular cloud complex show clumps embedded within filaments. Magnetic field vectors are overlaid.

simulations, this localized excess magnetic energy had to dissipate. This was shown to occur in the simulations, where magnetic energy was found to decline over time, preferentially on the size scale of protoclusters.

### 6.1.2 MHD Shock Dynamical Evolution of Prestellar Filaments

Filaments in the ISM are commonly observed normal to magnetic fields. Understanding the origin of this configuration (and whether or not it is important for star formation) is of current interest to the star formation community. While different explanations for this structure have been proposed (e.g. gravito-magneto contraction, uncertainty in dust polarization maps), a novel mechanism was presented in Chapter 5 that produces a similar configuration. Beginning with magnetized, oblique shocks that form at the intersection of two finite, supersonic streams of gas, post-shock pressure gradients were shown to drive the realignment of filaments that form between the flows, such that they approach a normal orientation with respect to the upstream velocity and magnetic field (Fig. 6.3). Given the ubiquity of flows in the ISM, this shock process may be of relevance to the formation of this early star formation structure.

### 6.1.3 Non-classical Collapse Dynamics of Bonnor-Ebert Spheres

Protostellar cores are commonly modeled as marginally stable Bonnor-Ebert spheres. In Chapter 3, a series of experiments were presented that explore the gravito-hydrodynamic interaction between embedded BE spheres and their ambient environments. These experiments were different than previous studies in that the *system* (embedded BE sphere+uniform, static background) was allowed to evolve dynamically rather than through forced perturbations. As the sphere gravitationally accelerated the ambient gas, ram pressure perturbations at the surface of the sphere from the infalling envelope drove compression waves into the sphere's interior. The amplitude of these waves can be expressed as a function of the weight of the environment, and can be strong enough to trigger collapse of the sphere itself. Interestingly, when collapse is initiated via compression waves, this set

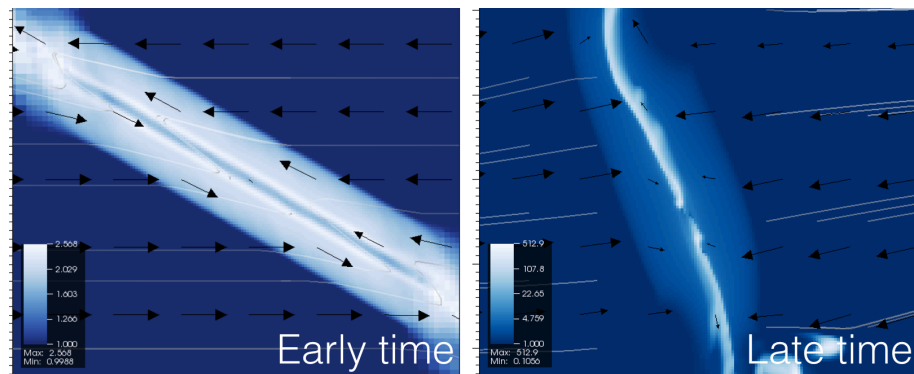


**Figure 6.3:** This density plot with overlaid velocity vectors and magnetic field lines shows the reorientation of a shock confined filament.

of simulations showed that the well-established ‘outside-in’ collapse profiles of BE spheres eventually emerged (Fig. 6.4). This suggests that over the lifetime of a protostellar core, measured density profiles may become degenerate between cores of differing initial conditions.

## 6.2 Future Directions

### 6.2.1 Cloud-to-core Star Formation and ‘Closing the Feedback Loop’

One of the limitations of star formation simulations up until now has been their single-scale, or ‘semi’ single-scale nature. For instance, instead of modeling the formation and evolution of individual protostellar cores beginning from the parent molecular cloud, simulations often prescribe initial and boundary conditions that mimic the larger natal environment. Clearly, boundary conditions must be imposed on any simulation after a certain scale, it is just a matter of where to draw those boundaries.

One of the future directions of this work is to push the boundaries of star formation simulations to even larger dynamic range. One way to accomplish this is using ‘zoom-in’ techniques, whereby highly localized regions within simulations are tagged for refinement and followed to greater

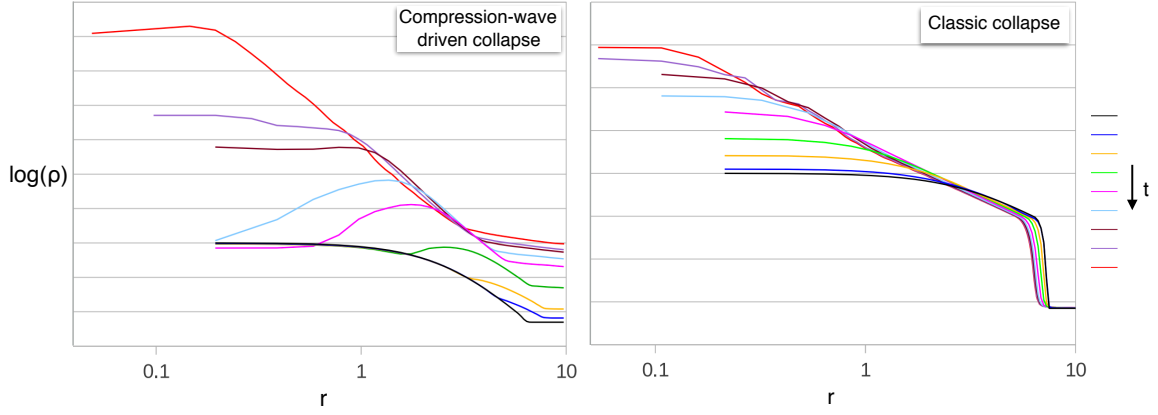


**Figure 6.4:** Radial density profiles of collapsing Bonnor-Ebert spheres, for the case of compression-wave induced collapse (left), and forced perturbation (right).

depths than their surroundings. To date, zoom-in techniques in star formation have mainly focused on the ‘clump-to-core’ scale. For instance, Offner et al. (2012) tracks the formation and collapse of protostellar cores within a turbulent box of length  $l = 2.9 \text{ pc}$  using AMR zoom-in methods. These simulations include self-gravity, radiative transfer, and feedback. Similarly, Bonnell et al. (2003); Hansen et al. (2012); Krumholz et al. (2016) begin with turbulent initial conditions of order  $1 - 2 \text{ pc}$  across, include some subset of radiative transfer, magnetic fields, and self-gravity, and increase the resolution of forming cores to follow the subsequent formation of protostars. It is worth noting that similar zoom-in techniques are becoming popular in cosmological and galaxy simulations, as well (c.f. recent work by Colín et al., 2016; Duarte-Cabral and Dobbs, 2017).

The zoom-in technique will be used in future work to investigate the effects of feedback on *self-consistently* generated cluster environments. These environments will be provided by the colliding flows dataset in Chapter 4, and thus, this work will represent some of the first *cloud-to-core* star formation simulations to date. The proposed cloud-to-core simulations will proceed as follows. First, a gravitationally bound and unstable clump will be selected from one of the simulated molecular

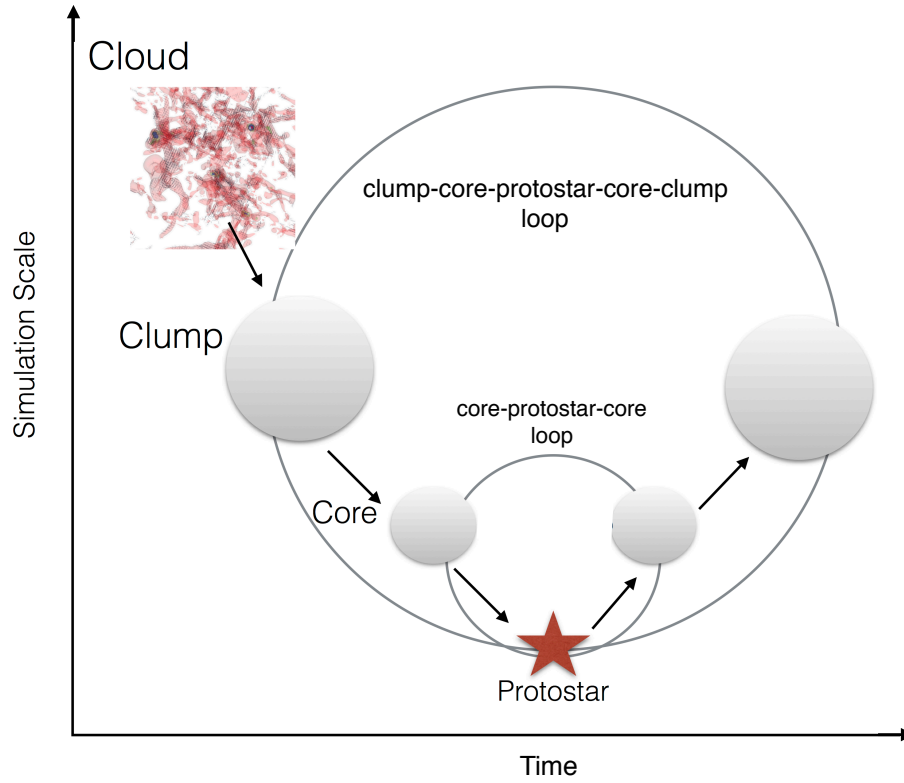


**Figure 6.5:** Cloud-to-core star formation simulations will begin at the cloud scale, and zoom-in to the formation of a single protostar/protostellar cluster. Feedback loops show the interaction between various scales of the simulations.

clouds. This clump will be on the order of  $1 - 10 \text{ pc}$  across, the typical size scale of a protocluster. Once isolated, the resolution of this clump can be selectively increased using AMR and its subsequent evolution followed in detail. This phase of the simulation represents the ‘cloud-to-clump’ leg of the *loop* shown in Figure 6.5.

Meanwhile, regions that are not spatially correlated with this clump can be de-refined to conserve computational cost. As the clump evolves and forms protostellar cores, the zoom-in process will be repeated, this time selectively increasing the resolution of a single protostellar *core* that is

bound, gravitationally unstable, and  $.1\text{ pc} - 10,000\text{ AU}$  across (‘clump-to-core’ leg, Fig. 6.5). In this way, protostellar core formation and evolution can be modeled self-consistently, *beginning from the molecular cloud scale*. Next, to ‘close the loop’ means to follow the collapse of this protostellar core as it forms a protostar that begins to feed back on its environment. This protostar will be modeled using a sink particle, which will inject radiation and outflows into its environment. As described in Sections 2.6.1- 2.6.2, AstroBEAR has recently been updated to include both of these sink particle feedback algorithms. This stage of the simulation represents the ‘core-protostar-core loop’ in Fig. 6.5. In a similar way, the larger ‘cloud-core-protostar-core-cloud loop’ in Fig. 6.5 could be explored by increasing the resolution of *multiple* collapsing cores within the parent clump.

One of the aims of this cloud-to-core-to-cloud project will be to better constrain the physics of feedback and the mechanisms by which feedback regulates the initial mass function of forming clusters. Indeed, developing a deeper understanding of feedback physics is a crucial next step in star formation research, given the rich datasets that will soon be provided by the James Webb Space Telescope (JWST) and the Large Millimeter Telescope (LMT) on clustered star formation. In addition to the theoretical aspects of feedback, future work will also focus on bridging the gap between theory and observation. To this end, synthetic observations will be generated of this data to compare numerical results to young, nearby cluster environments such as NGC 1333 and Serpens South.

Synthetic observations might include  $1.1\text{ mm}$  emission maps, which can easily be generated using the publicly available software package CASA (McMullin et al., 2007) following Offner et al. (2011). These maps will be directly comparable to an upcoming survey aimed at characterizing protostellar cores using the TolTEC camera and the LMT. In addition, synthetic emission maps of  $FEII$  ( $1.644\text{ }\mu\text{m}$ ) and  $H_2$  ( $2.128\text{ }\mu\text{m}$ ). These lines trace shocks, are accessible to JWST, and can be used to constrain cooling rates, mass loss rates, and momenta fluxes associated with protostellar outflows (Raines et al., 2000; Maret et al., 2009).

### 6.2.2 Turbulent Fragmentation across Cosmic Time

Stars have the remarkable property that their mass distribution at birth appears to be the same, irrespective of location within the galaxy (Kroupa, 2002). Even more remarkable still, this initial mass function appears to hold in neighboring galaxies as well (Zinnecker & Yorke, 2007). The apparent universality of the IMF suggests that there are fundamental, underlying physical mechanisms that govern star formation in the local universe.

While the IMF translates into a diverse stellar landscape today, there is a glaring peculiarity: we have yet to observe a star born from the pristine, primordial gas of the Big Bang. Where is this first generation of stars? If the same physics governs star formation in the early universe, then we might expect the IMF to also be temporally universal. However, the conspicuous absence of the first generation of stars (the so-called Population III stars, or POP III stars, for short) suggests otherwise. Instead of being ‘bottom-heavy’ (i.e. peaked in the low-mass end of the spectrum), the primordial IMF appears to be ‘top-heavy’ (i.e. sharply peaked about massive stars). If POP III stars were much more massive than the current generations of stars, this could explain their observed scarcity: they have already exploded as supernovae, or collapsed directly into black-holes.

The hypothesized transition in the IMF from bottom- to top-heavy has most widely been attributed to metallicity. Indeed, numerical simulations support that decreases in metallicity are linked to massive star formation. These projects often investigate the effect of metallicity on accretion rates of stars formed by spherical protostellar cores that have been perturbed into collapse (Omukai et al., 2010; Clark et al., 2008), or the formation of protostellar cores using cosmological initial conditions and simplistic chemical networks and equations of states (Chiaki et al., 2016; Stacy et al., 2016). However, if the distribution of stellar masses primarily results from hierarchical, turbulent fragmentation (as is currently accepted in modern star formation theory), *how does this turbulent fragmentation depend on metallicity?*

Thus, future work is being planned that will explore the nature of turbulent fragmentation

---

in primordial environments. This work will build on the previously conducted thesis research in turbulent molecular cloud dynamics. Planned directions include numerically investigating forced vs. decaying turbulence as a function of metallicity, in order to constrain decay rates, mixing, instabilities, and morphological structure formation related to star formation in the early universe. Numerical simulations will include self-gravity, radiation transport, magnetic fields, relevant chemical networks, and experimentally derived opacities. This project has strong synergies to ongoing research into the ‘First Stars’ cosmology project being conducted at Los Alamos National Laboratory, as well as basic research being conducted into supernova engines and light curves, MHD/hydrodynamical turbulence, radiation transport, and plasma physics.

# Bibliography

Alves, J. F., Lada, C. J., & Lada, E. A. 2001, *nature*, 409, 159

Anathpindika, S. & Di Francesco, J. 2013, *MNRAS*, 430, 154

André, P., Men'shchikov, A., Bontemps, S., Könyves, V., Motte, F., Schneider, N., Didelon, P., Minier, V., Saraceno, P., Ward-Thompson, D., di Francesco, J., White, G., Molinari, S., Testi, L., Abergel, A., Griffin, M., Henning, T., Royer, P., Merín, B., Vavrek, R., Attard, M., Arzoumanian, D., Wilson, C. D., Ade, P., Aussel, H., Baluteau, J.-P., Benedettini, M., Bernard, J.-P., Blommaert, J. A. D. L., Cambrésy, L., Cox, P., di Giorgio, A., Hargrave, P., Hennemann, M., Huang, M., Kirk, J., Krause, O., Launhardt, R., Leeks, S., Le Penne, J., Li, J. Z., Martin, P. G., Maury, A., Olofsson, G., Omont, A., Peretto, N., Pezzuto, S., Prusti, T., Roussel, H., Russeil, D., Sauvage, M., Sibthorpe, B., Sicilia-Aguilar, A., Spinoglio, L., Waelkens, C., Woodcraft, A., & Zavagno, A. 2010, *A&A*, 518, L102

Arzoumanian, D., André, P., Didelon, P., Könyves, V., Schneider, N., Men'shchikov, A., Soubie, T., Zavagno, A., Bontemps, S., di Francesco, J., Griffin, M., Hennemann, M., Hill, T., Kirk, J., Martin, P., Minier, V., Molinari, S., Motte, F., Peretto, N., Pezzuto, S., Spinoglio, L., Ward-Thompson, D., White, G., & Wilson, C. D. 2011, *A&A*, 529, L6

Audit, E. & Hennebelle, P. 2005, *A&A*, 433, 1

- Bacmann, A., André, P., Puget, J.-L., Abergel, A., Bontemps, S., & Ward-Thompson, D. 2000, *A&A*, 361, 555
- Ballesteros-Paredes, J. 2000, in *ESA Special Publication*, Vol. 445, *Star Formation from the Small to the Large Scale*, ed. F. Favata, A. Kaas, & A. Wilson, 323
- Ballesteros-Paredes, J. & Hartmann, L. 2007, *RMxAA*, 43, 123
- Ballesteros-Paredes, J., Hartmann, L., & Vázquez-Semadeni, E. 1999, *ApJ*, 527, 285
- Bally, J., Langer, W. D., Stark, A. A., & Wilson, R. W. 1987, *ApJl*, 312, L45
- Banerjee, R. & Pudritz, R. E. 2006, *ApJ*, 641, 949
- Banerjee, R., Pudritz, R. E., & Holmes, L. 2004, *MNRAS*, 355, 248
- Banerjee, R., Vázquez-Semadeni, E., Hennebelle, P., & Klessen, R. S. 2009, *MNRAS*, 398, 1082
- Beck, R. 2001, *SSRv*, 99, 243
- Beck, S. C., Kelly, D. M., & Lacy, J. H. 1998, *AJ*, 115, 2504
- Beichman, C. A., Myers, P. C., Emerson, J. P., Harris, S., Mathieu, R., Benson, P. J., & Jennings, R. E. 1986, *ApJ*, 307, 337
- Bodenheimer, P. & Sweigart, A. 1968, *ApJ*, 152, 515
- Bok, B. J. 1948, *Harvard Observatory Monographs*, 7, 53
- Bonnell, I. A., Bate, M. R., & Vine, S. G. 2003, *MNRAS*, 343, 413
- Bonnor, W. 1956, *MNRAS*, 116, 351
- Bourke, T. L., Myers, P. C., Robinson, G., & Hyland, A. R. 2001, *ApJ*, 554, 916
- Brunt, C. M. 2003, *ApJ*, 583, 280

- Carpenter, J. M. 2000, *AJ*, 120, 3139
- Carroll-Nellenback, J., Frank, A., & Heitsch, F. 2014, *ApJ*, 790, 37
- Carroll-Nellenback, J. J., Shroyer, B., Frank, A., & Ding, C. 2013, *Journal of Computational Physics*, 236, 461
- Chapman, N. L., Goldsmith, P. F., Pineda, J. L., Clemens, D. P., Li, D., & Krčo, M. 2011, *ApJ*, 741, 21
- Chen, C.-Y. & Ostriker, E. C. 2014, *ApJ*, 785, 69
- Chiaki, G., Yoshida, N., & Hirano, S. 2016, *MNRAS*, 463, 2781
- Clark, P. C., Glover, S. C. O., & Klessen, R. S. 2008, *ApJ*, 672, 757
- Colella, P. & Woodward, P. R. 1984, *J. Comput. Phys.*, 54, 174
- Colín, P., Avila-Reese, V., Roca-Fàbrega, S., & Valenzuela, O. 2016, *ApJ*, 829, 98
- Crutcher, R. M. 1999, *ApJ*, 520, 706
- Crutcher, R. M., Wandelt, B., Heiles, C., Falgarone, E., & Troland, T. H. 2010, *ApJ*, 725, 466
- Cunningham, A., Frank, A., & Hartmann, L. 2005, *ApJ*, 631, 1010
- Cunningham, A. J., Frank, A., Varnière, P., Mitran, S., & Jones, T. W. 2009, *ApJS*, 182, 519
- Dame, T. M., Hartmann, D., & Thaddeus, P. 2001, *ApJ*, 547, 792
- Dawson, J. R., McClure-Griffiths, N. M., Dickey, J. M., & Fukui, Y. 2011, *ApJ*, 741, 85
- Dawson, J. R., McClure-Griffiths, W. T., Dickey, J. M., Hughes, A., & Kawamura, A. 2013, *ApJ*, 763, 56
- De Colle, F., Raga, A. C., & Esquivel, A. 2008, *ApJ*, 689, 302

- Ebert, R. 1955, *Z. Astrophys*, 37, 217
- Einfeldt, B., Munz, C., Roe, P. L., & Sjogreen, B. 1991, *J. Comput.Phys.*, 92, 273
- Eisenhauer, F., Quirrenbach, A., Zinnecker, H., & Genzel, R. 1998, *ApJ*, 498, 278
- Elmegreen, B. G. 2000, *ApJ*, 530, 277
- Falgarone, E., Phillips, T. G., & Walker, C. K. 1991, *ApJ*, 378, 186
- Falgarone, E., Puget, J.-L., & Perault, M. 1992, *A&A*, 257, 715
- Federrath, C., Banerjee, R., Clark, P. C., & Klessen, R. S. 2010a, *ApJ*, 713, 269
- Federrath, C. & Klessen, R. S. 2012, *ApJ*, 761, 156
- Federrath, C., Roman-Duval, J., Klessen, R. S., Schmidt, W., & Mac Low, M.-M. 2010b, *AAP*, 512, A81
- Federrath, C., Schrön, M., Banerjee, R., & Klessen, R. S. 2014, *ApJ*, 790, 128
- Federrath, C., Sur, S., Schleicher, D. R. G., Banerjee, R., & Klessen, R. S. 2011, *ApJ*, 731, 62
- Fernández-López, M., Arce, H. G., Looney, L., Mundy, L. G., Storm, S., Teuben, P. J., Lee, K., Segura-Cox, D., Isella, A., Tobin, J. J., Rosolowsky, E., Plunkett, A., Kwon, W., Kauffmann, J., Ostriker, E., Tassis, K., Shirley, Y. L., & Pound, M. 2014, *ApJL*, 790, L19
- Field, G. B. 1965, *ApJ*, 142, 531
- Fogerty, E., Carroll-Nellenback, J., Frank, A., Heitsch, F., & Pon, A. 2017, in press, *MNRAS*
- Fogerty, E., Frank, A., Heitsch, F., Carroll-Nellenback, J., Haig, C., & Adams, M. 2016, *MNRAS*, 460, 2110
- Foster, P. 1994, in *Proceedings of the 4th Haystack Observatory Conference*, Vol. 65, 105

- Foster, P. N. & Chevalier, R. A. 1993, *ApJ*, 416, 303
- Fukui, Y. & Yonekura, Y. 1998, in *IAU Symposium*, Vol. 179, *New Horizons from Multi-Wavelength Sky Surveys*, ed. B. J. McLean, D. A. Golombek, J. J. E. Hayes, & H. E. Payne, 165
- Goodman, A. A., Barranco, J. A., Wilner, D. J., & Heyer, M. H. 1998, *ApJ*, 504, 223
- Goodman, A. A., Jones, T. J., Lada, E. A., & Myers, P. C. 1992, *ApJ*, 399, 108
- Haig, C. M., Heitsch, F., Carroll, J., & Frank, A. 2012, in *American Astronomical Society Meeting Abstracts*, Vol. 219, *American Astronomical Society Meeting Abstracts #219*, 349.02
- Hansen, C. E., Klein, R. I., McKee, C. F., & Fisher, R. T. 2012, *ApJ*, 747, 22
- Hansen, E. C., Frank, A., & Hartigan, P. 2015, *ApJ*, 800, 41
- Hartmann, L. 2001, *AJ*, 121, 1030
- Hartmann, L., Ballesteros-Paredes, J., & Bergin, E. A. 2001a, *ApJ*, 562, 852
- Hartmann, L., Ballesteros-Paredes, J., & E., B. 2001b, *ApJ*, 562, 852
- Hartmann, L. 2003, *ApJ*, 585, 398
- Hayashi, C. 1966, *ARAA*, 4, 171
- Heiles, C., Goodman, A. A., McKee, C. F., & Zweibel, E. G. 1993, in *Protostars and Planets III*, ed. E. H. Levy & J. I. Lunine, 279–326
- Heiles, C. & Troland, T. H. 2005, *ApJ*, 624, 773
- Heitsch, F., Burkert, A., Hartmann, L., Slyz, A. D., & Devriendt, J. G. 2005, *ApJ*, 633, L113
- Heitsch, F., Hartmann, L. W., Slyz, A. D., Devriendt, J. E. G., & Burkert, A. 2008, *ApJ*, 674, 316
- Heitsch, F., Slyz, A. D., Devriendt, J., Hartmann, L. W., & Burkert, A. 2007, *ApJ*, 665, 445

- Heitsch, F., Slyz, A. D., Devriendt, J. E. G., Hartmann, L. W., & Burkert, A. 2006, *ApJ*, 648, 1052
- Heitsch, F., Stone, J. M., & Hartmann, L. W. 2009, *ApJ*, 695, 248
- Hennebelle, A. P., Whitworth, A. P., Gladwin, P. P., & Andre, P. 2003, *MNRAS*, 340, 870
- Hennebelle, P. 2013, *A&A*, 556, A153
- Hennebelle, P., Banerjee, R., Vázquez-Semadeni, E., Klessen, R. S., & Audit, E. 2008, *A&A*, 486, L43
- Hunter, C. 1977, *ApJ*, 218, 834
- Hunter, J. H. 1979, *ApJ*, 233, 946
- Hunter, J. H., Sandford II, M. T., Whitaker, R. W., & Klein, R. I. 1986, *ApJ*, 305, 309
- Inoue, T. & Inutsuka, S.-i. 2008, *ApJ*, 687, 303
- Inutsuka, S., Inoue, T., Iwasaki, K., & Hosokawa, T. 2015, *A&A*, forthcoming
- Jeans, J. H. 1929, *Astronomy and Cosmology* (Cambridge), 345
- Jessop, N. E. & Ward-Thompson, D. 2001, *MNRAS*, 323, 1025
- Johnstone, D. & Bally, J. 1999, *ApJl*, 510, L49
- Kaminski, E., Frank, A., Carroll, J., & Myers, P. 2013, in *Protostars and Planets VI Posters*
- Kaminski, E., Frank, A., Carroll, J., & Myers, P. 2014, *ApJ*, 790, 70
- Kirk, H., Myers, P. C., Bourke, T. L., Gutermuth, R. A., Hedden, A., & Wilson, G. W. 2013, *ApJ*, 766, 115
- Klessen, R. S., Heitsch, F., & Mac Low, M.-M. 2000, *ApJ*, 535, 887
- Körtgen, B. & Banerjee, R. 2015, *MNRAS*, 451, 3340

- Koyama, H. & Inutsuka, S.-i. 2004, *ApJL*, 602, L25
- Kroupa, P. 2002, *Science*, 295, 82
- Krumholz, M. R., Klein, R. I., McKee, C. F., & Bolstad, J. 2007, *ApJ*, 667, 626
- Krumholz, M. R., Myers, A. T., Klein, R. I., & McKee, C. F. 2016, *MNRAS*, 460, 3272
- Lada, C. J., Lombardi, M., & Alves, J. F. 2010, *ApJ*, 724, 687
- Lada, E. A. & Lada, C. J. 1995, *AJ*, 109, 1682
- Larson, R. 1969, *MNRAS*, 145, 271
- Larson, R. B. 1979, *MNRAS*, 186, 479
- Larson, R. B. 1981, *MNRAS*, 194, 809
- Larson, R. B. 2003, *Reports on Progress in Physics*, 66, 1651
- Lazarian, A., Santos-Lima, R., & de Gouveia Dal Pino, E. 2010, in *Astronomical Society of the Pacific Conference Series*, Vol. 429, *Numerical Modeling of Space Plasma Flows, Astronom-2009*, ed. N. V. Pogorelov, E. Audit, & G. P. Zank, 113
- Lee, C. W., Myers, P. C., & Tafalla, M. 1999, *ApJ*, 526, 788
- Lee, K. I., Fernández-López, M., Storm, S., Looney, L. W., Mundy, L. G., Segura-Cox, D., Teuben, P., Rosolowsky, E., Arce, H. G., Ostriker, E. C., Shirley, Y. L., Kwon, W., Kauffmann, J., Tobin, J. J., Plunkett, A. L., Pound, M. W., Salter, D. M., Volgenau, N. H., Chen, C.-Y., Tassis, K., Isella, A., Crutcher, R. M., Gammie, C. F., & Testi, L. 2014, *ApJ*, 797, 76
- Liu, F. K. 1996, *MNRAS*, 281, 1197
- Looney, L. W., Wang, S., Hamidouche, M., Safier, P. N., & Klein, R. 2006, *ApJ*, 642, 330

- Mac Low, M.-M. & Klessen, R. S. 2004, *Reviews of Modern Physics*, 76, 125
- Maret, S., Bergin, E. A., Neufeld, D. A., Green, J. D., Watson, D. M., Harwit, M. O., Kristensen, L. E., Melnick, G. J., Sonnentrucker, P., Tolls, V., Werner, M. W., Willacy, K., & Yuan, Y. 2009, *ApJ*, 698, 1244
- Marquina, A. 1994, *SIAM J. Sci. Comput.*, 15, 892
- McMullin, J. P., Waters, B., Schiebel, D., Young, W., & Golap, K. 2007, in *Astronomical Society of the Pacific Conference Series*, Vol. 376, *Astronomical Data Analysis Software and Systems XVI*, ed. R. A. Shaw, F. Hill, & D. J. Bell, 127
- Miyoshi, T. & Kusano, K. 2005, *J. Comput. Phys.*, 208, 315
- Mouschovias, T. C. 1979, *ApJ*, 228, 475
- Mouschovias, T. C. 1991, in *NATO Advanced Science Institutes (ASI) Series C*, Vol. 342, *NATO Advanced Science Institutes (ASI) Series C*, ed. C. J. Lada & N. D. Kylafis, 61
- Myers, P. C. 1983, *ApJ*, 270, 105
- Myers, P. C. & Benson, P. J. 1983, *ApJ*, 266, 309
- Myers, P. C. & Gammie, C. F. 1999, *ApJL*, 522, L141
- Myers, P. C. 2008, *ApJ*, 687, 340
- Nakano, T. & Nakamura, T. 1978, *PASJ*, 30, 671
- Offner, S. S. R., Klein, R. I., & McKee, C. F. 2008, *ApJ*, 686, 1174
- Offner, S. S. R., Lee, E. J., Goodman, A. A., & Arce, H. 2011, *ApJ*, 743, 91
- Offner, S. S. R., Robitaille, T. P., Hansen, C. E., McKee, C. F., & Klein, R. I. 2012, *ApJ*, 753, 98

- Omukai, K., Hosokawa, T., & Yoshida, N. 2010, *ApJ*, 722, 1793
- Palla, F. & Stahler, S. W. 2000, *ApJ*, 540, 255
- Palmeirim, P., Andre, P., Ward-Thompson, D., Arzoumanian, D., Konyves, V., Didelon, P., Schneider, N., Benedettini, M., Bontemps, S., Di Francesco, J., Elia, D., Griffin, M., Hennemann, M., Hill, T., Martin, P. G., & Men'shchikov. 2013, *A&A*, 550, A38
- Passot, T., Vazquez-Semadeni, E., & Pouquet, A. 1995, *ApJ*, 455, 536
- Penston, M. 1969a, *MNRAS*, 144, 425
- Penston, M. V. 1969b, *MNRAS*, 145, 457
- Planck Collaboration, Ade, P. A. R., Aghanim, N., Alves, M. I. R., Arnaud, M., Arzoumanian, D., Aumont, J., Baccigalupi, C., Banday, A. J., Barreiro, R. B., Bartolo, N., Battaner, E., Benabed, K., Benoit-Lévy, A., Bernard, J.-P., Berné, O., Bersanelli, M., Bielewicz, P., Bonaldi, A., Bonavera, L., Bond, J. R., Borrill, J., Bouchet, F. R., Boulanger, F., Bracco, A., Burigana, C., Calabrese, E., Cardoso, J.-F., Catalano, A., Chamballu, A., Chiang, H. C., Christensen, P. R., Clements, D. L., Colombi, S., Colombo, L. P. L., Combet, C., Couchot, F., Crill, B. P., Curto, A., Cuttaia, F., Danese, L., Davies, R. D., Davis, R. J., de Bernardis, P., de Rosa, A., de Zotti, G., Delabrouille, J., Dickinson, C., Diego, J. M., Donzelli, S., Doré, O., Douspis, M., Ducout, A., Dupac, X., Elsner, F., Enßlin, T. A., Eriksen, H. K., Falgarone, E., Ferrière, K., Finelli, F., Forni, O., Frailis, M., Fraisse, A. A., Franceschi, E., Frejsel, A., Galeotta, S., Galli, S., Ganga, K., Ghosh, T., Giard, M., Giraud-Héraud, Y., Gjerløw, E., González-Nuevo, J., Górski, K. M., Gregorio, A., Gruppuso, A., Guillet, V., Hansen, F. K., Hanson, D., Harrison, D. L., Hernández-Monteagudo, C., Herranz, D., Hildebrandt, S. R., Hivon, E., Hobson, M., Holmes, W. A., Hufenberger, K. M., Hurier, G., Jaffe, A. H., Jaffe, T. R., Jones, W. C., Juvela, M., Keskitalo, R., Kisner, T. S., Knoche, J., Kunz, M., Kurki-Suonio, H., Lagache, G., Lamarre, J.-M., Lasenby, A., Lawrence, C. R., Leonardi, R., Levrier, F., Liguori, M., Lilje, P. B., Linden-Vørnle, M., López-Caniego, M.,

- Lubin, P. M., Macías-Pérez, J. F., Maffei, B., Mandolesi, N., Mangilli, A., Maris, M., Martin, P. G., Martínez-González, E., Masi, S., Matarrese, S., Mazzotta, P., Melchiorri, A., Mendes, L., Mennella, A., Migliaccio, M., Mitra, S., Miville-Deschênes, M.-A., Moneti, A., Montier, L., Morgante, G., Mortlock, D., Munshi, D., Murphy, J. A., Naselsky, P., Nati, F., Natoli, P., Nørgaard-Nielsen, H. U., Noviello, F., Novikov, D., Novikov, I., Oppermann, N., Pagano, L., Pajot, F., Paladini, R., Paoletti, D., Pasian, F., Perrotta, F., Pettorino, V., Piacentini, F., Piat, M., Pierpaoli, E., Pietrobon, D., Plaszczynski, S., Pointecouteau, E., Polenta, G., Pratt, G. W., Puget, J.-L., Rachen, J. P., Rebolo, R., Reinecke, M., Remazeilles, M., Renault, C., Renzi, A., Ricciardi, S., Ristorcelli, I., Rocha, G., Rosset, C., Rossetti, M., Roudier, G., Rubiño-Martín, J. A., Rusholme, B., Sandri, M., Savelainen, M., Savini, G., Scott, D., Soler, J. D., Stolyarov, V., Sutton, D., Suur-Uski, A.-S., Sygnet, J.-F., Tauber, J. A., Terenzi, L., Toffolatti, L., Tomasi, M., Tristram, M., Tucci, M., Valenziano, L., Valiviita, J., Van Tent, B., Vielva, P., Villa, F., Wade, L. A., Wandelt, B. D., Yvon, D., Zacchei, A., & Zonca, A. 2016, *A&A*, 586, A136
- Poludnenko, A. Y., Frank, A., & Blackman, E. G. 2002, *ApJ*, 576, 832
- Polychroni, D. 2012, in 10th Hellenic Astronomical Conference, ed. I. Papadakis & A. Anastasiadis, 24–24
- Pon, A., Johnstone, D., & Heitsch, F. 2011, *ApJ*, 740, 88
- Pon, A., Toalá, J. A., Johnstone, D., Vázquez-Semadeni, E., Heitsch, F., & Gómez, G. C. 2012, *ApJ*, 756, 145
- Raga, A. C. 1992, *MNRAS*, 258, 301
- Raines, S. N., Watson, D. M., Pipher, J. L., Forrest, W. J., Greenhouse, M. A., Satyapal, S., Woodward, C. E., Smith, H. A., Fischer, J., Goetz, J. A., & Frank, A. 2000, *ApJL*, 528, L115
- Shu, F. H. 1977, *ApJ*, 214, 488

- Shu, F. H. & Adams, F. 1987, in *Circumstellar matter; Proceedings of the IAU Symposium, Heidelberg*, 7–22
- Shu, F. H., Adams, F. C., & Lizano, S. 1987a, *ARA&A*, 25, 23
- Shu, F. H., Lizano, S., & Adams, F. 1987b, in *Star forming regions; Proceedings of the Symposium, Tokyo, Japan*, 417–433
- Simon, M. 1997, *ApJL*, 482, L81
- Spitzer, L. 1968, *Nebulae and Interstellar Matter* (The University of Chicago Press), 44
- Stacy, A., Bromm, V., & Lee, A. T. 2016, *MNRAS*, 462, 1307
- Tafalla, M., Mardones, D., Myers, P. C., Caselli, P., Bachiller, R., & Benson, P. J. 1998, *ApJ*, 504, 900
- Teixeira, P., Lada, C., & Alves, J. 2005, *ApJ*, 629, 276
- Toalá, J. A., Vázquez-Semadeni, E., & Gómez, G. C. 2012, *ApJ*, 744, 190
- Tritsis, A., Panopoulou, G. V., Mouschovias, T. C., Tassis, K., & Pavlidou, V. 2015, *MNRAS*, 451, 4384
- Troland, T. H. & Heiles, C. 1986, *ApJ*, 301, 339
- Truelove, J., Klein, R. L., McKee, C. F., Holliman, J. H., Howell, L. H., & Greenough, J. A. 1997, *ApJl*, 489
- van Dishoeck, E. F. & Black, J. H. 1988, *ApJ*, 334, 771
- van Dishoeck, E. F. & Blake, G. A. 1998, *ARAA*, 36, 317
- Van Leer, B. 1979, *J. Comput.Phys.*, 32, 101

- Vázquez-Semadeni, E., Banerjee, R., Gómez, G. C., Hennebelle, P., Duffin, D., & Klessen, R. S. 2011, MNRAS, 414, 2511
- Vázquez-Semadeni, E., Dongsu, R., Passot, T., Gonzalez, R. F., & Gazol, A. 2006, ApJ, 643, 245
- Vazquez-Semadeni, E., Passot, T., & Pouquet, A. 1995, ApJ, 441, 702
- Ward-Thompson, D. 2002, Science, 295, 76
- Ward-Thompson, D., André, P., & Kirk, J. M. 2002, MNRAS, 329, 257
- Whitworth, A. & Summers, D. 1985, MNRAS, 214, 1
- Zinnecker, H. & Yorke, H. W. 2007, ARAA, 45, 481

# Index

- Ballesteros-Paredes (2000), 6, 152  
 Beck (2001), 76, 152  
 Bok (1948), 2, 152  
 Bonnor (1956), 27, 39, 152  
 Brunt (2003), 9, 11, 74, 152  
 Carpenter (2000), 73, 152  
 Crutcher (1999), 4, 74, 153  
 Ebert (1955), 27, 39, 153  
 Elmegreen (2000), 154  
 Field (1965), 140, 154  
 Foster (1994), 39, 40, 154  
 Hartmann (2001), 112, 155  
 Hayashi (1966), 4, 155  
 Hennebelle (2013), 136, 156  
 Hunter (1977), 39, 40, 49, 156  
 Hunter (1979), 73, 156  
 Jeans (1929), 39, 156  
 Kroupa (2002), 149, 157  
 Larson (1969), 40, 157  
 Larson (1979), 4, 157  
 Liu (1996), 30, 157  
 Marquina (1994), 18, 158  
 Mouschovias (1979), 3, 6, 158  
 Mouschovias (1991), 158  
 Myers (1983), 3, 158  
 Penston (1969a), 40, 159  
 Penston (1969b), 4, 159  
 Poludnenko et al. (2002), 160  
 Polychroni (2012), 11, 117, 160  
 Raga (1992), 90, 160  
 Shu (1977), 40, 160  
 Simon (1997), 3, 161  
 Spitzer (1968), 29, 161  
 Van Leer (1979), 18, 161  
 Ward-Thompson (2002), 5, 162  
 Alves et al. (2001), 2, 39, 151  
 Anathpindika & Di Francesco (2013), 40–42, 151  
 André et al. (2010), 11, 117, 151  
 Arzoumanian et al. (2011), 11, 117, 151  
 Audit & Hennebelle (2005), 73, 151  
 Bacmann et al. (2000), 2, 151  
 Ballesteros-Paredes & Hartmann (2007), 152

- Ballesteros-Paredes et al. (1999), 8, 73, 74, 152
- Bally et al. (1987), 121, 152
- Banerjee & Pudritz (2006), 5, 152
- Banerjee et al. (2004), 5, 39, 40, 42, 47, 49, 152
- Banerjee et al. (2009), 74, 83, 90, 93, 105, 112, 120, 152
- Beck et al. (1998), 73, 152
- Beichman et al. (1986), 72, 152
- Bodenheimer & Sweigart (1968), 4, 152
- Bonnell et al. (2003), 146, 152
- Bourke et al. (2001), 4, 152
- Carroll-Nellenback et al. (2013), 10, 14, 19, 153
- Carroll-Nellenback et al. (2014), 77, 78, 82, 85, 90, 107, 108, 111, 153
- Chapman et al. (2011), 118, 153
- Chen & Ostriker (2014), 74, 83, 93, 111, 112, 153
- Chiaki et al. (2016), 149, 153
- Clark et al. (2008), 149, 153
- Colella & Woodward (1984), 18, 153
- Colín et al. (2016), 153
- Crutcher et al. (2010), 74, 153
- Cunningham et al. (2005), 153
- Cunningham et al. (2009), 10, 14, 19, 153
- Dame et al. (2001), 72, 153
- Dawson et al. (2011), 74, 153
- Dawson et al. (2013), 74, 153
- De Colle et al. (2008), 90, 153
- Einfeldt et al. (1991), 19, 154
- Eisenhauer et al. (1998), 73, 154
- Falgarone et al. (1991), 3, 8, 154
- Falgarone et al. (1992), 3, 154
- Federrath & Klessen (2012), 79, 154
- Federrath et al. (2010a), 32, 154
- Federrath et al. (2010b), 79, 154
- Federrath et al. (2011), 112, 154
- Federrath et al. (2014), 35, 38, 154
- Fernández-López et al. (2014), 11, 117, 118, 138, 154
- Fogerty et al. (2016), 121, 135, 136, 154
- Fogerty et al. (2017), 154
- Foster & Chevalier (1993), 40, 41, 47, 49, 154
- Fukui & Yonekura (1998), 73, 155
- Goodman et al. (1992), 118, 155
- Goodman et al. (1998), 3, 155
- Haig et al. (2012), 136, 155
- Hansen et al. (2012), 146, 155
- Hansen et al. (2015), 90, 155
- Hartmann et al. (2001a), 73, 74, 155
- Hartmann et al. (2001b), 6, 74, 155
- Hartmann, L. (2003), 155
- Heiles & Troland (2005), 4, 76, 155
- Heiles et al. (1993), 4, 155

- 
- Heitsch et al. (2005), 155
- Heitsch et al. (2006), 73, 78, 155
- Heitsch et al. (2007), 74, 93, 105, 112, 120, 155
- Heitsch et al. (2008), 73, 155
- Heitsch et al. (2009), 74, 93, 111, 112, 156
- Hennebelle et al. (2003), 41, 42, 156
- Hennebelle et al. (2008), 74, 93, 105, 111, 120, 156
- Hunter et al. (1986), 73, 156
- Inoue & Inutsuka (2008), 31, 76, 123, 156
- Inutsuka et al. (2015), 74, 156
- Jessop & Ward-Thompson (2001), 2, 156
- Johnstone & Bally (1999), 121, 156
- Kaminski et al. (2013), 156
- Kaminski et al. (2014), 156
- Kirk et al. (2013), 11, 117, 118, 138, 156
- Klessen et al. (2000), 156
- Koyama & Inutsuka (2004), 138, 156
- Krumholz et al. (2007), 157
- Krumholz et al. (2016), 146, 157
- Körtgen & Banerjee (2015), 74, 75, 111–113, 136, 156
- Lada & Lada (1995), 73, 157
- Lada et al. (2010), 157
- Larson, R. B. (2003), 2, 5, 6, 157
- Larson, R. B. (1981), 3, 6, 73, 157
- Lazarian et al. (2010), 112, 157
- Lee et al. (1999), 2, 157
- Lee et al. (2014), 11, 117, 157
- Looney et al. (2006), 74, 157
- Mac Low & Klessen (2004), 157
- Maret et al. (2009), 148, 158
- McMullin et al. (2007), 148, 158
- Miyoshi & Kusano (2005), 19, 158
- Myers & Benson (1983), 2, 3, 158
- Myers & Gammie (1999), 3, 158
- Myers, P. C. (2008), 42, 158
- Nakano & Nakamura (1978), 81, 158
- Offner et al. (2008), 5, 158
- Offner et al. (2011), 148, 158
- Offner et al. (2012), 146, 158
- Omukai et al. (2010), 149, 158
- Palla & Stahler (2000), 73, 159
- Palmeirim et al. (2013), 138, 159
- Passot et al. (1995), 9, 159
- Planck Collaboration et al. (2016), 118, 138, 159
- Pon et al. (2011), 160
- Pon et al. (2012), 160
- Raines et al. (2000), 148, 160
- Shu & Adams (1987), 40, 160
- Shu et al. (1987a), 6, 161
- Shu et al. (1987b), 40, 161

- 
- Stacy et al. (2016), 149, 161
- Tafalla et al. (1998), 2, 161
- Teixeira et al. (2005), 68, 161
- Toalá et al. (2012), 161
- Tritsis et al. (2015), 74, 161
- Troland & Heiles (1986), 74, 161
- Truelove et al. (1997), 33, 45, 161
- Vazquez-Semadeni et al. (1995), 8, 9, 162
- Vázquez-Semadeni et al. (2006), 73, 162
- Vázquez-Semadeni et al. (2011), 74, 81–83, 90,  
111, 112, 161
- Ward-Thompson et al. (2002), 2, 162
- Whitworth & Summers (1985), 41, 42, 162
- Zinnecker & Yorke (2007), 149, 162
- van Dishoeck & Black (1988), 93, 161
- van Dishoeck & Blake (1998), 93, 161